

**MICROSTRUCTURES AND PROPERTIES  
OF COCRMO ALLOY BY METAL INJECTION  
MOULDING PROCESS**

The logo of the University of Malaysia Pahang (UMP) is a shield-shaped emblem. It features a central white vertical band. The left side of the shield is light blue, and the right side is light purple. At the top, a yellow diamond is set within a light blue oval. The letters 'UMP' are written in white across the bottom of the shield.

**NUR AIDAH NABIHAH BINTI DANDANG**

**MASTER OF SCIENCE**

**UNIVERSITI MALAYSIA PAHANG**

## UNIVERSITI MALAYSIA PAHANG

### DECLARATION OF THESIS AND COPYRIGHT

Author's Full Name : NUR AIDAH BINTI DANDANG NABIHAH

Date of Birth : 11<sup>TH</sup> AUGUST 1993

Title : MICROSTRUCTURES AND PROPERTIES OF COCRMO  
ALLOY BY METAL INJECTION MOULDING PROCESS

Academic Session : 2018/2019

I declare that this thesis is classified as:

- CONFIDENTIAL (Contains confidential information under the Official Secret Act 1997)\*
- RESTRICTED (Contains restricted information as specified by the organization where research was done)\*
- OPEN ACCESS I agree that my thesis to be published as online open access (Full Text)

I acknowledge that Universiti Malaysia Pahang reserves the following rights:

1. The Thesis is the Property of Universiti Malaysia Pahang
2. The Library of Universiti Malaysia Pahang has the right to make copies of the thesis for the purpose of research only.
3. The Library has the right to make copies of the thesis for academic exchange.

Certified by:

\_\_\_\_\_  
(Student's Signature)

\_\_\_\_\_  
(Supervisor's Signature)

NUR AIDAH NABIHAH BINTI  
DANDANG  
New IC Number: 930811115604  
Date:

ASSOC. PROF. DR WAN  
SHARUZI WAN HARUN  
Date:

## SUPERVISOR'S DECLARATION

We hereby declare that we have checked this thesis and in our opinion, this thesis is adequate in terms of scope and quality for the award of the degree of Master of Science.

---

(Supervisor's Signature)

Full Name : DR WAN SHARUZI WAN HARUN

Position : ASSOCIATE PROFESSOR

Date :

---

(Co-supervisor's Signature)

Full Name : DR NUR ZALIKHA KHALIL

Position : SENIOR LECTURER

Date :

### STUDENT'S DECLARATION

I hereby declare that the work in this thesis is based on my original work except for quotations and citations which have been duly acknowledged. I also declare that it has not been previously or concurrently submitted for any other degree at Universiti Malaysia Pahang or any other institutions.

---

(Student's Signature)

Full Name : NUR AIDAH NABIHAH BINTI DANDANG

ID Number : MMM16021

Date :



UMP

MICROSTRUCTURES AND PROPERTIES OF COCRM0 ALLOY BY METAL  
INJECTION MOULDING PROCESS



NUR AIDAH NABIHAH BINTI DANDANG

Thesis submitted in fulfillment of the requirements  
for the award of the degree of  
Master of Science

UMP

Faculty of Mechanical and Manufacturing Engineering

UNIVERSITI MALAYSIA PAHANG

MAY 2019

## ACKNOWLEDGEMENTS

Syukur Alhamdulillah, the first word that resembles everything for His precious given. With His blessing, after all, my research work had finally come to an end within the given timeframe. I would like to extend my heartfelt gratitude to all that have been contributed in this project especially to my supervisor, PM Dr Wan Sharuzi Wan Harun, and my co-supervisor, Dr Nur Zalikha Khalil for their encouragement, guidance and advice during one and half semesters to completely finish this research work.

I also would like to express my particular thanks to Universiti Malaysia Pahang (UMP) for giving me the opportunity and support to carry out my research successfully. My sincere appreciation also goes to Mr Zukarnain, technician staff of Mechanical Engineering Faculty for his help and cooperation. I greatly acknowledge all Green Research for Advanced Materials Laboratory (GRAMSlab)'s teams for their helping hand and lessons during my research activities. A significant contribution and hard working from them to cooperate with me while conducting and completing this thesis was great indeed.

Continued prayers and support from my husband, Mohamad Iamie Bin Rosli, I'm really thankful, thank you for being a great companion and truly understand each of my hard day. I also would like to express sincere appreciation to my beloved family especially my beloved parents Dandang Bin Jusoh and Zaini Binti Embong for an irreplaceable sacrifice and continuous support from the beginning until now. Their love and concern are everything to me until finally, I managed to complete my research and thesis.

Lastly, I would like to convey my gratitude to all people who directly or indirectly give me a hand in the process of completing this thesis. It was one of the greatest experience learning and the fundamental knowledge during this particular period.



UMP

## ABSTRAK

Logam campuran CoCr kebiasaannya digunakan untuk tujuan pembedahan kerana mempunyai sifat daya tahan daripada kakisan, kekuatan logam yang tinggi dan juga bersifat biokompabiliti. Proses pembentukan logam (*MIM*) adalah satu daripada proses metalurgi serbuk yang digunakan untuk menghasilkan suatu komponen yang rumit dan menepati kehendak bentuk. Kini, proses tersebut juga telah dijadikan sebagai salah satu alternatif bagi menghasilkan implan untuk tujuan pembedahan dan pergigian sesuai dengan kehendak pasaran perubatan yang tinggi. Proses pembentukan logam ini terhasil melalui teknik pencampuran logam dan komponen perikat, kemudian proses pengacuan injeksi antara logam dan komponen perikat, seterusnya peleraian pengikat (*debinding*) dan pensinteran (*sintering*). Fasa *Sintering* dan *debinding* adalah fasa yang terpenting di dalam proses pembentukan logam memandangkan kedua-dua fasa ini mampu mempengaruhi sifat-sifat produk akhir setelah proses sintering. Hal ini kerana, kegagalan memilih parameter yang sesuai sewaktu proses ini boleh menyebabkan kerosakan produk akhir lebih daripada 25%. Mudah rapuh, ruang rongga yang banyak semasa proses *debinding* akan menyebabkan produk akhir selepas proses *sintering* menjadi senang retak dan tidak berkualiti. Oleh itu, kajian ini bertujuan untuk menentukan parameter yang sesuai bagi fasa *solvent debinding*, kemudian mengkaji kesan parameter fasa *sintering* terhadap struktur mikro produk akhir dan juga kesan parameter sintering terhadap sifat fizikal, mekanikal dan sifat kakisan produk. Komponen pertama yang dihasilkan selepas proses pengacuan injeksi akan *didebound* melalui proses *solvent debinding* dalam larutan n-heptane pada suhu 50, 60 dan 70°C selama 4 jam. Komponen kedua yang dihasilkan selepas proses *solvent debinding*, akan melalui proses sintering pada suhu 1250, 1300 dan 1350°C selama 1 dan 3 jam dalam atmosfera argon. Setelah itu, komponen akhir yang terhasil selepas fasa sintering akan dikaji melalui kaedah ketumpatan, ujian ketegangan dan kekerasan mikro. Sifat kakisan ditentukan daripada kaedah elektrokimia. Manakala, kajian metallografi untuk permukaan patah dan pembentukan liang struktur mikro komponen dianalisis melalui mikroskop optic (OM) dan mikroskop pengimpasan electron (SEM). Hasil eksperimen telah menunjukkan, *solvent debinding* pada suhu 60°C selama 4 jam ditentukan sebagai parameter yang sesuai untuk proses ini memandangkan peratus kehilangan perikat mencukupi iaitu 76.9%. Manakala, komponen yang disinter pada 1350°C-3jam menunjukkan ketumpatan tertinggi (92.5%), kekerasan mikro (308.1 HV), kekuatan tegangan (728.5 MPa) dan kadar kakisan yang bagus, 2.16E-06 mm / tahun dibandingkan dengan sintered pada 1250°C-jam, 1300°C-jam, 1350°C-1jam, 1250°C-3jam dan 1350°C-3jam. Apabila suhu meningkat, dan masa dipanjangkan untuk proses sintering, kekuatan tegangan dan kekerasan meningkat secara beransur-ansur. Manakala, struktur mikro komponen sintered menunjukkan bahawa ikatan morfologi antara partikel serbuk menjadi lebih padat apabila masa yang diperuntukkan sesuai iaitu 3jam dan suhu sintering yang tinggi pada 1350°C. Tambahan pula, pengecilan ruang rongga di dalam struktur mikro komponen juga telah membantu menguatkan sifat mekanikal logam komponen CoCrMo. Kesimpulannya, suhu dan masa sewaktu proses sintering adalah parameter yang kritikal untuk kepadatan ruang rongga dan meningkatkan sifat-sifat mekanikal dan sifat-sifat kakisan kompak sinteran.

## ABSTRACT

The CoCr-based alloy is used for surgical inserts due to their superior corrosion resistance, high strength and good in biocompatibility. Metal injection moulding (MIM) is one of the powder metallurgy process used for the fabrication of complex and near net shape assembly of high-performance materials. Currently, this method has also been used as an optional way to fabricate implants in surgery and dentistry befitting for economical mass production. MIM process involves mixing, injection moulding, debinding and sintering. Sintering and debinding is the main stage in the injection moulding process that could affect the properties of the sintered part. In some instances, no optimised parameters were apply to both process may cause defective for final products formed up to 25 %. Brittle, porous structure of brown compacts after debinding caused sintered compact after sintering process become easily cracks and not quality compacts were formed. This research interests in the persistence of optimum parameter for solvent debinding process, the effects of sintering parameters on microstructure of sintered compact and effect of sintering parameters on physical, mechanical properties and corrosion behaviours of sintered compacts. The CoCrMo alloy compacts were solvent debound in n-heptane solution at 50, 60 and 70 °C for 4 hours soaking time. The brown compacts produced was continued to a sintering process at temperature 1250, 1300 and 1350 °C for 1 and 3 hours in an argon atmosphere respectively. The tensile and microhardness testing determined the mechanical properties of sintered CoCrMo alloy compacts. The corrosion properties were characterised from electrochemical method experiments. Metallographic studies of fractures surface and pore formation were observed by optical microscopy (OM) and scanning electron microscope (SEM). The results of the investigation indicate that solvent debinding at 60 °C for 4 hours was found to be optimum parameters for solvent debinding due to adequate mass loss of paraffin wax which reported at 76.9 %. While compacts sintered at 1350 °C-3h showed the highest density (92.5 %), hardness (308.1 Hv) and tensile strength (728.5 MPa) and desirable corrosion rate of 2.16E-06 mm/year compared to the sintered conditions at 1250 °C-1h, 1300 °C-1h, 1350 °C-1h, 1250 °C-3h and 1350 °C-3h. As the temperature increased, and holding time was prolonged to 3 hours, the tensile strength and the hardness increased gradually. While, from the morphology of sintered compacts, it shows that the morphological bonding between powder particles become denser with longer sintering time, 3 h highest sintering temperature of 1350 °C. Moreover, the decrease in porosity amount was shown to improve the mechanical properties of CoCrMo alloy sintered compacts. It can be concluded that the sintering temperature and time is a critical parameter for reducing the amount of porosity and improving mechanical properties of sintered compacts.



## TABLE OF CONTENT

<b>DECLARATION</b>	
<b>TITLE PAGE</b>	
<b>ACKNOWLEDGEMENTS</b>	<b>ii</b>
<b>ABSTRAK</b>	<b>iii</b>
<b>ABSTRACT</b>	<b>iv</b>
<b>TABLE OF CONTENT</b>	<b>v</b>
<b>LIST OF TABLES</b>	<b>ix</b>
<b>LIST OF FIGURES</b>	<b>x</b>
<b>LIST OF SYMBOLS</b>	<b>xiii</b>
<b>LIST OF ABBREVIATIONS</b>	<b>xiv</b>
<b>CHAPTER 1 INTRODUCTION</b>	<b>1</b>
1.1 Research Background	1
1.2 Problem Statement	2
1.3 Objectives of Study	4
1.4 Scopes of Research	4
1.5 Significance of Study	5
1.6 Thesis Structure	5
<b>CHAPTER 2 LITERATURE REVIEW</b>	<b>7</b>
2.1 Introduction	7
2.2 Metallic Biomaterials for Powder-Based Manufacturing Processes	7
2.2.1 Titanium and Titanium based alloys	10

2.2.2	CoCr-based alloys	11
2.2.3	316L Stainless Steel	12
2.2.4	Other metal and metal alloy biomaterial	13
2.3	The common parameter of metallic powder biomaterial	13
2.4	Properties of CoCr-based alloy	16
2.4.1	CoCr-based alloy for biomedical applications	16
2.4.2	ASTM F75	17
2.5	Parameters of metal injection moulding (MIM)	19
2.6	Metal injection moulding (MIM)	23
2.7	The process	23
2.7.1	Mixing and pelletizing	24
2.7.2	Characteristics of feedstock	25
2.7.3	Debinding process	26
2.7.4	Sintering process	27
2.8	Characterisation of CoCr-based alloy	30
2.8.1	Physical and mechanical properties	30
2.8.2	Chemical properties	32
2.8.3	Microstructural analysis	33
2.9	Summary	34
<b>CHAPTER 3 METHODOLOGY</b>		<b>36</b>
3.1	Introduction	36
3.2	Compact Preparation	38
3.2.1	Characterisation of CoCr-based alloy	38
3.3	Characterisation of CoCr- based alloy powders and feedstock	40
3.3.1	Thermal analysis of the feedstock	40

3.4	The metal injection moulding process	42
3.4.1	Preparation of feedstock	44
3.4.2	Mixing process	45
3.4.3	Injection moulding	45
3.4.4	Debinding Process	47
3.5	Thermal debinding and sintering process	48
3.6	Characterisation of the compacts	50
3.6.1	Physical testing	50
3.6.2	Mechanical testing	53
3.6.3	Microstructural analysis of compacts	54
3.6.4	Corrosion behaviour study	58
3.1	Summary	59
<b>CHAPTER 4 RESULTS AND DISCUSSION</b>		<b>60</b>
4.1	Introduction	60
4.2	Characterisation of metal powder	60
4.2.1	Particle size distribution of CoCr-based alloy powder	60
4.2.2	Selection of optimum powder loading	61
4.3	Feedstock characterisation	63
4.3.1	DSC measurement of binder's component and feedstock	63
4.3.2	TGA analysis of binder's component and feedstock	64
4.4	Injection moulding	65
4.5	Solvent debinding	67
4.6	Thermal debinding and sintering process	71
4.7	Characterisation of sintered compact	72
4.7.1	Microstructure study	72

4.7.2	Physical properties	76
4.7.3	Mechanical properties	80
4.8	Electrochemical properties of sintered compact	88
<b>CHAPTER 5 CONCLUSIONS AND RECOMMENDATIONS</b>		<b>91</b>
5.1	Introduction	91
5.2	Conclusions	91
5.3	Recommendation	92
<b>REFERENCES</b>		<b>94</b>
<b>APPENDIX A PUBLICATIONS</b>		<b>110</b>



## LIST OF TABLES

Table 2.1	Common powder parameters of metallic biomaterials	15
Table 2.2	Typical properties of cast and wrought cobalt-base alloys	17
Table 2.3	Parameters of metal injection moulding for metallic biomaterials	22
Table 2.4	Tensile properties of the CoCr-based alloy	32
Table 3.1	Properties of CoCr-based alloy powder provided by the manufacturer	38
Table 3.2	Chemical composition of CoCr-based alloy powder provided by the manufacturer	39
Table 3.3	Characterisation of binders	40
Table 3.4	Specific labelling for compact's condition for each stage of the MIM process	44
Table 3.5	Powder and binder ratio by mass (%)	44
Table 3.6	Estimated weight and volume for a tensile green compact in this study	44
Table 3.7	MIM Processing Parameters in this study	46
Table 3.8	Prototype labelling for the sintered compact	50
Table 3.9	Setting parameters for Universal tensile testing machine	53
Table 3.10	Chemical used for the etching process	58
Table 4.1	Characteristics of metal powder	61
Table 4.2	Grain size analysis sintered compacts for each sintering condition	75
Table 4.3	Density of CoCrMo alloy sintered compact.	79
Table 4.4	Yield stress, Ultimate tensile strength, and elongation of the compact at different sintering condition	83
Table 4.5	Corrosion behaviour analysis of sintered compacts, respectively	89

## LIST OF FIGURES

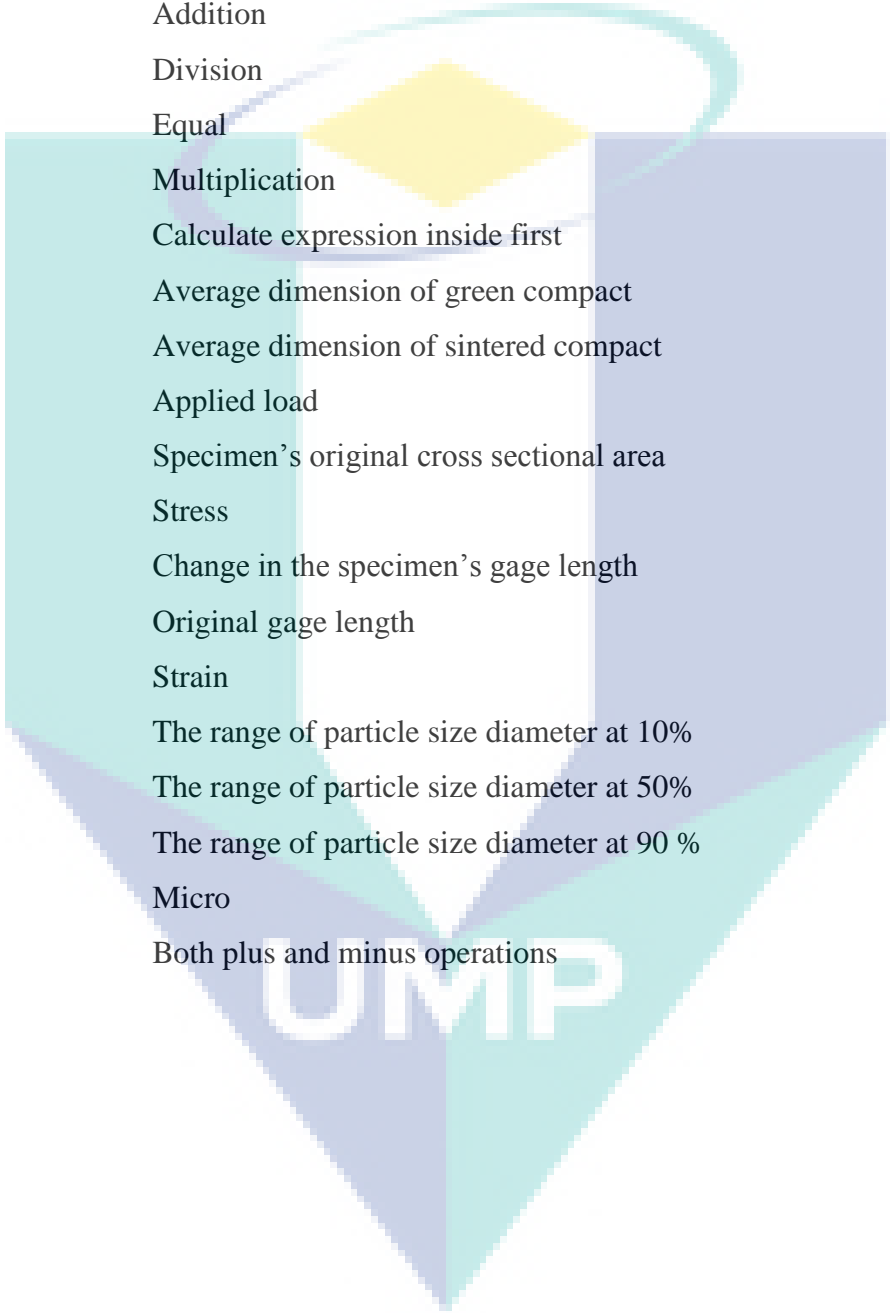
Figure 2.1	Trend of metal and metal alloy biomaterials for powder -based manufacturing processes for the year 2000-2017 (%)	10
Figure 2.2	Microstructure of as-cast (a) and as sintered (b) F75 alloys with 0.35%C Microstructure of forged high-strength Co-Cr-Mo alloy (c)	19
Figure 2.3	Metal Injection Moulding Process	24
Figure 2.4	Debinding process	26
Figure 2.5	Neck formation and microstructure changes when necks growth	28
Figure 2.6	Vickers Hardness Test Schematic diagram	30
Figure 2.7	Metallic behaviour curve	32
Figure 2.8	Typical as-cast microstructure of HS21 alloy, original magnification 100x (13) (a) and microstructure of HS after 24 hours at 870 °C, magnification 500x (b)	34
Figure 3.1	Research flow chart	37
Figure 3.2	Morphology image of the CoCr-based alloy powder	38
Figure 3.3	Laser scattering particle analyzer	39
Figure 3.4	Thermogravimetric Analysis (TGA) machine	41
Figure 3.5	Differential Scanning Electron (DSC) machine	41
Figure 3.6	Disc shape compacts	42
Figure 3.7	Overview of the metal injection moulding process	43
Figure 3.8	Double Planetary mixer machine	45
Figure 3.9	Tensile shape model according to ASTM 638-type V standard (unit in mm)	46
Figure 3.10	NISSEI 20-tonne injection moulding machine components	46
Figure 3.11	Mould used in the current study ( Tensile shape model according to ASTM 638 – type V standard)	47
Figure 3.12	Schematic diagram for solvent debinding by wicking technique	48
Figure 3.13	Graph illustrates Time vs Temperature plot of solvent debinding	48
Figure 3.14	Steps for thermal debinding and sintering process	49
Figure 3.15	Graph pattern of thermal debinding and sintering process	50

Figure 3.16	Schematic diagram of MIM CoCrMo tensile bar	51
Figure 3.17	Method of measuring relative density	52
Figure 3.18	Precisa Gravimetrics Equipment	52
Figure 3.19	INSTRON Universal Testing Machine	53
Figure 3.20	Mounted compact	54
Figure 3.21	Vickers Hardness Machine MATSUZAWA Type MMT X7	54
Figure 3.22	Steps to measure amount of porosity by Image J Software analysis	56
Figure 3.23	Hot mounting of CoCrMo alloy sintered compact	56
Figure 3.24	Metkon grinding and polishing machine	57
Figure 3.25	Polishing solutions after the grinding process	57
Figure 3.26	Solutions and tools used for etching	58
Figure 3.27	Yellowish white solution ready to use for etching	58
Figure 3.28	Painted sintered compact by acrylic painting	59
Figure 3.29	Set up a diagram for electrochemical testing	59
Figure 4.1	Particle Size Distribution Curve	61
Figure 4.2	Optical micrograph of sintered compact ; a) 64 vol.% PL b) 65 vol.% PL c) 66 vol.% PL d) 67 vol.% PL e) 68 vol.% PL	63
Figure 4.3	Percentage of porosity for five different powder loading	63
Figure 4.4	DSC of binder's component (a) and DSC measurements of feedstocks (b)	64
Figure 4.5	TGA of binder's component (a) and TGA measurements of feedstocks (b)	65
Figure 4.6	Green compact of CoCr-based alloy	66
Figure 4.7	Defect (a) Short shot (b) Sink mark (c) Fracture	67
Figure 4.8	Time vs Temperature plot for paraffin wax's mass loss during solvent debinding	69
Figure 4.9	A schematic graph of paraffin wax loss for each phase	69
Figure 4.10	Defects observed on brown compact a) Fractures b) collapse c) cracks at conditions 70°C and 4 hour	70
Figure 4.11	SEM micrographs of green compact before solvent debinding (a) and brown compact after solvent debinding (b)	71
Figure 4.12	CoCrMo compacts (a) Green vs brown compact (after debinding) (b) green vs sintered compact (after sintering)	72

Figure 4.13	Optical micrograph of sintered compact; (a) 1250°C-1h; (b) 1250°C-3h; (c) 1300°C-1h; (d) 1300°C-3h; (e) 1350°C-1h; (f) 1350°C-3h.	73
Figure 4.14	Amount of porosity of CoCr-based alloy sintered compact by Image J Analyser Software	74
Figure 4.15	Optical micrograph of sintered compact; (a) 1250°C-1h; (b) 1250°C-3h; (c) 1300°C-1h; (d) 1300°C-3h; (e) 1350°C-1h; (f) 1350°C-3h	76
Figure 4.16	Dimensional change of sintered compact	77
Figure 4.17	Dimensional change of sintered compact at 1h sintering condition (a) and 3h (b)	78
Figure 4.18	Percentage of shrinkage for CoCrMo alloy sintered compacts.	78
Figure 4.19	Relation between density, amount of porosity and percentage of shrinkage for CoCrMo alloy sintered compacts	80
Figure 4.20	Micro-hardness of CoCrMo alloy sintered compacts	81
Figure 4.21	Relation between hardness and amount of porosity for CoCrMo alloy sintered compacts	82
Figure 4.22	Stress-strain curves at different sintering condition for CoCrMo alloy sintered compacts	83
Figure 4.23	SEM image of sintered CoCrMo at 1350°C-3h.	84
Figure 4.24	SEM image of sintered CoCrMo at 1350°C-3h (a) SEM image and EDS analysis of sintered CoCrMo at 1350°C-3h (b)	84
Figure 4.25	XRD analysis of sintered CoCrMo at 1350°C-3h	85
Figure 4.26	Fracture surface of sintered CoCrMo at (a) 1250°C-1h (b) 1250°C-3h (c) 1300°C-1h (d) 1300°C-3h (e) 1350°C-1h and (b) 1350°C-3h	87
Figure 4.27	Brittle fracture surface of sintered CoCrMo at 1350°C-3h after tensile test	87
Figure 4.28	Potentiodynamic of CoCrMo compacts, sintered at 1250, 1300 and 1350°C for 1 and 3 h; Ringer solution, 37°C	88
Figure 4.29	Corrosion rate vs corrosion current density ( $i_{corr}$ ) analysis of sintered compacts, respectively	90
Figure 4.30	Corrosion rate vs amount of porosity analysis of sintered compacts, respectively	90

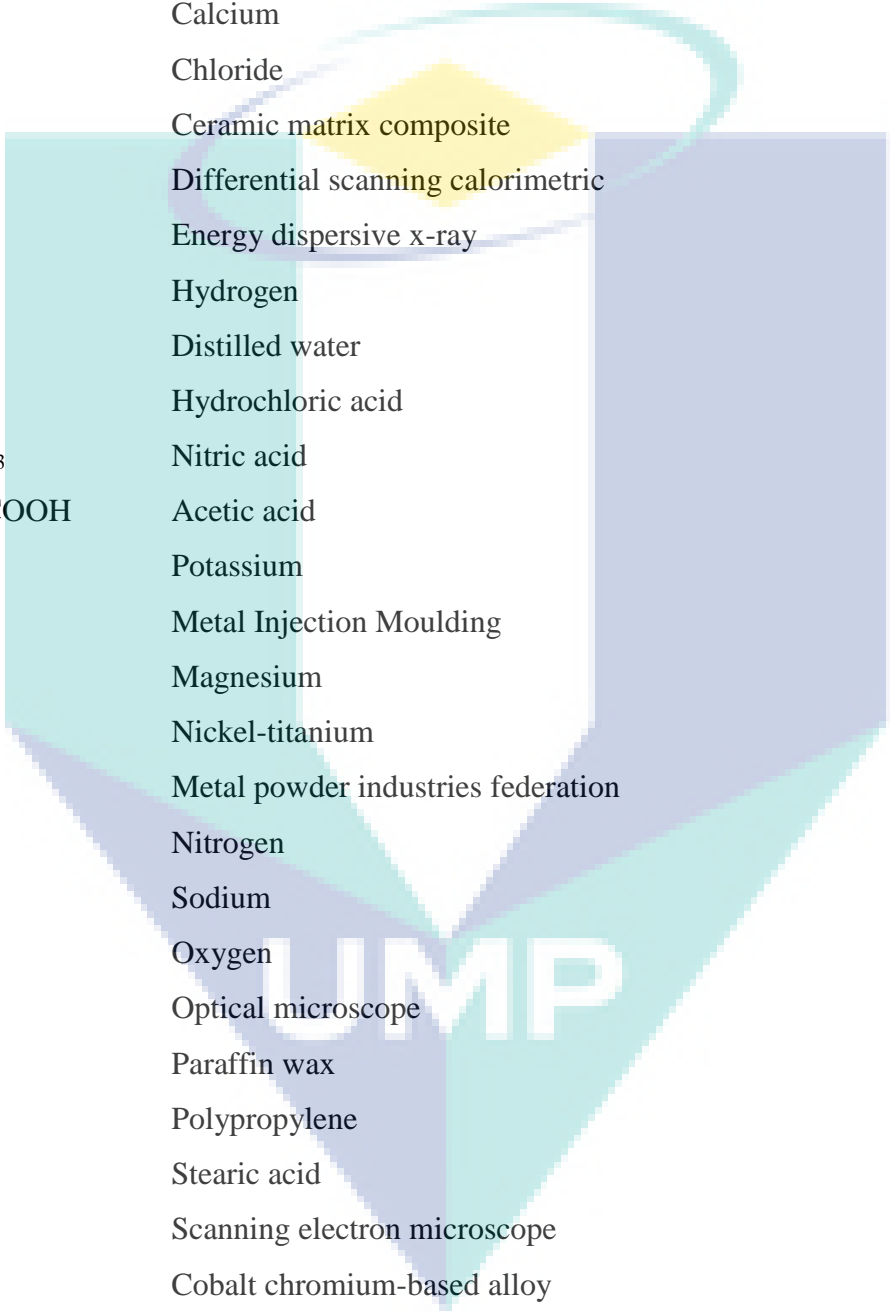


## LIST OF SYMBOLS



$<$	Less than
$>$	More than
$-$	Subtraction
$+$	Addition
$/$	Division
$=$	Equal
$\times$	Multiplication
$()$	Calculate expression inside first
$d_1$	Average dimension of green compact
$d_2$	Average dimension of sintered compact
$P$	Applied load
$A_0$	Specimen's original cross sectional area
$\sigma$	Stress
$\delta$	Change in the specimen's gage length
$L_0$	Original gage length
$\epsilon$	Strain
$D_{10}$	The range of particle size diameter at 10%
$D_{50}$	The range of particle size diameter at 50%
$D_{90}$	The range of particle size diameter at 90 %
$\mu$	Micro
$\pm$	Both plus and minus operations

## LIST OF ABBREVIATIONS



ASTM	American society for testing materials
At. %	Percentage in atomic
C	Carbon
Ca	Calcium
Cl	Chloride
CMC	Ceramic matrix composite
DSC	Differential scanning calorimetric
EDS	Energy dispersive x-ray
H	Hydrogen
H <sub>2</sub> O	Distilled water
HCl	Hydrochloric acid
HNO <sub>3</sub>	Nitric acid
CH <sub>3</sub> COOH	Acetic acid
K	Potassium
MIM	Metal Injection Moulding
Mg	Magnesium
NiTi	Nickel-titanium
MPIF	Metal powder industries federation
N	Nitrogen
Na	Sodium
O	Oxygen
OM	Optical microscope
PW	Paraffin wax
PP	Polypropylene
SA	Stearic acid
SEM	Scanning electron microscope
CoCr	Cobalt chromium-based alloy
CoCrMo	Cobalt chromium molybdenum alloy
TGA	Thermogravimetric analysis
Wt.%	Percentage in weight
Vol.%	Percentage in volume

## CHAPTER 1

### INTRODUCTION

#### 1.1 Research Background

Cobalt-Chromium (CoCr)-based alloys have been developed and employed for many years as medical implants. These alloys are commonly used for surgical implants because of their high strength, superior corrosion resistance, non-magnetic behaviour, and biocompatibility (Girardin et al., 2016; Hedberg et al., 2014; Liu et al.; X. Wang et al., 2013). Applications of CoCr-based alloys include prosthetic replacements of hips, knees, elbows, shoulders, ankles, and fingers, bone plates, screws, staples, and rods; and heart valves (E. Liverani et al., 2016; Robison et al., 2016). Various in vitro and in vivo tests have indicated that the alloys are biocompatible and suitable for use as surgical implants (M. M. Dewidar et al., 2006). CoCr-based alloy implants can be obtained by casting or forging; forging process starts from bar or rod stock achieved by conventional forming of cast billets or by hot isostatic pressing of Co alloy powders.

In recent years, the CoCr-based alloy is been used as a suitable material for the biomedical applications with regard to its biocompatibility and corrosion resistance (Ismail et al., 2012). These alloys are commonly produced by casting. However, small complex parts are hardly produced by this method. Therefore, researchers had found alternative ways which are powder metallurgy method for CoCr-based alloy fabrication. MIM as one of PM process is a considerable suggestion to produced CoCr-based alloy compact) due to sufficient green density, low porosity, and considerable hardness can be achieved in the final parts by this process (Hayat, Wen, Li, et al., 2015; Obasi et al., 2010). MIM starts with the mixing of fine metal powder with a suitable thermoplastic binder to form the feedstock. The binder aids the flowability and formability of fine metal powders during moulding, and they have to be removed in the next stage to enable high-density

components to be produced. The removal of the binder is done either thermally in the furnace or by solvent extraction. Ideally, the removal of the binder would open up pore channels which allow accelerated removal of the higher boiling point components. The components are sintered following the debinding stage. This stage is crucial to the MIM process as appropriate debinding and sintering conditions would ensure pore-free structures that have excellent mechanical properties.

Theoretical studies of sintering treat the powder as a spherical particle and divide sintering into three stages (Dourandish et al., 2008; Shu et al., 2006). The early stage of sintering occurs at low temperatures and is characterised by neck growth at the contact points between the particles. The intermediate stage of sintering is characterised by an interconnected pore system having complex geometry. The final stage begins when the pore phase becomes closed, and the shrinkage rate of the components slow down. The suitable choice for sintering parameters will increase the properties besides reducing the porosity of sintered compacts after microstructure observations.

Therefore, this study is carried out to analyse the influences of the MIM processing parameters of different sintering conditions on the microstructure, physical and mechanical properties and also corrosion behaviour of CoCr-based alloy compacts. The compacts were sintered at three different sintering temperatures from 1250, 1300 and 1350°C at two different sintering time; 1 and 3 hours by using 10°C/min heating rate under an argon atmosphere. It is expected that compact with higher sintering temperature and longer sintering time would exhibit morphological analysis that will support better physical and mechanical properties and corrosion behaviour results.

## **1.2 Problem Statement**

The CoCr-based alloy is a material of apparent interest. Various combinations of properties can be achieved by using this alloys (M. M. Dewidar et al., 2006; Henriques et al., 2015; Koike et al., 2011; Mohd Afian et al., 2014; M. OMAR et al.; Ryan et al., 2006; Takaichi et al., 2013; Torres et al., 2014; Wen et al., 2014). Among others metallic biocompatible materials such as stainless steels and Titanium and its alloy, CoCr-based alloy exhibit suitable characteristics for biomedical applications due to their non-toxicity, high biocompatibility, corrosion resistance and at affordable cost (Gulsoy et al., 2015; Mutlu, 2016; Raza et al., 2016; M. Rafi Raza et al., 2012; Xin et al., 2014). Nevertheless,

some critical issues such as the applications of CoCr-based alloys are still limited in this industry primarily due to its low affordability that extracts from its difficult extraction and machining process. (Hayat, Wen, Li, et al., 2015; Imgrund et al.; H.-S. Wang et al., 2014). Powder metallurgy (PM) which is a near-net-shaping technique offers a promotion to overcome this problem. MIM as one of PM process, can be considered an ideal candidate for CoCr-based alloys processing due to its ability to process intricate shapes at low production cost per part (in massive volume production) (Bolzoni et al., 2014; Bolzoni et al., 2016; Seyed Farid Seyed et al., 2015).

Recently, in the MIM process, a majority of researchers dealt with the phases of debinding and sintering. These phases are the most unpredictable. There must be an acceptable removal of binder thru debinding and uniform shrinkage through sintering. In some instances, defective products formed extent up to 25 % due to no optimised parameters for this processes. This is both economically and ecologically and intolerable (M. Dewidar, 2012; D. Li et al., 2009; Salahinejad et al., 2010). Thru debinding, the compacts are very brittle and rather porous. Progressively, the pores are formed which are increasingly more significant. Once the pores are undesirable large or connected to each other, it can lead to cracks in the final part. The additional risk is that binder is not melted, but decomposed into low molecular weight species (such as water, methane, carbon dioxide or carbon monoxide).

Whereas, for the sintering process, unappropriated sintering parameters; temperature, time, heating rate and atmosphere stated by (R. M. German et al., 1992) caused the formation of closed spherical pore besides further shrinkage of the compacts will become very difficult in the final stage. Additionally, some compacts are inspected to have an air contact with surrounding and cause a high level of impurities to occur within the compacts which are detrimental to the density and properties of final compacts. At higher sintering temperatures, creep happens to lead to distortion but not cracking. As the component mass decreases, these high-temperature problems are less evident. The primary function of the sintering temperature is to protect metal parts from the effects of air contact which leads to pores elimination. While, for the holding time, not much study was discussed on that. However, from (Limberg et al., 2012; Palermo, 2014) when the green compact is formed through low-pressure shaping which is MIM process, the

suitable sintering temperature suggested were (in a range of 1200-1360 °C) and the holding time may also be longer which is (between 90-180 min).

It can be concluded that the most influential factors in the MIM process are the existence of porosity in the sintered compact. Therefore, the amount of porosity exists should be minimised to improve the quality of final compacts. Additionally, this sintering parameters may affect the corrosion resistance properties. Thus, the total surface area for the compact was also minimised which translated to minimum corrosion rate due to less surface for corrosion reaction to occur. Better corrosion-rate of the metal implant is always commonly desired criterion in a biomedical discipline. This work aims to study the effect of sintering temperature and sintering time on the properties of CoCr-based alloy compacted. The physical, mechanical properties, microstructure and corrosion behaviour of sintered compacts were comparatively analysed to understand the mechanisms of sintering.

### **1.3 Objectives of Study**

The objectives of this study are:

- I. To determine the optimum solvent debinding setting parameters for the CoCrMo alloy green compact
- II. To identify the effect of sintering parameters on the microstructure of the CoCrMo alloy sintered compact
- III. To determine the effect of sintering parameters on the physical, mechanical and corrosion properties of CoCrMo alloy sintered compact.

### **1.4 Scopes of Research**

The scope of this research is divided into a few sections in which the first one is to study the powder characteristics via several analyses such as particle size analyser, SEM, and XRD. Powder loading preparation is also essential where powder mixing is carried out with different volume of powder loading by using the hot-pressed method. The powder to volume ratio of CoCr-based alloy with the addition of binders was done approximately in the respective powder mixing ratios (64, 65, 66, 67 and 68 vol. %).

This study focuses on the debinding process with different debinding parameters (50,60 and 70°C for 30 -240 minutes) and sintering processing with different sintering temperatures (1250, 1300 and 1350°C) and different sintering times (one and three hours). The alloy powder of CoCrMo and three types of binder (paraffin wax, polypropylene, and stearic acid) are used in this project while the mixing process carried out using a mixer. Thermal analysis via DSC and TGA is conducted to verify the thermal event during heating which produces useful information for mixing and debinding stage. Several characterisations of sintered compacts would take place mainly regarding physical and includes dimensional analysis, shrinkage measurement, relative density, and a tensile test by using Instron tensile test machine, microhardness test, microstructure analysis by SEM and EDX analysis, and lastly corrosion behaviour test by electrochemical method.

### **1.5 Significance of Study**

The findings in this research work are based on the capability of the processing technique by MIM to produce sintered compact of the CoCr-based alloy. The aim is to focus on the suitable processing parameters of the MIM process especially on debinding and sintering stage to obtain an ideal CoCr-based alloy compact. Then. The properties of the CoCr-based alloy compacts were analysed. There is physical properties study on shrinkage measurement and density, mechanical properties study on hardness and tensile strength and microstructure analysis by Optical Microscope, Selective Electron Microscope, EDS and XRD analysis on porosity, grain size, element analysis and phase identification. From this work, it also presents a practical study using CoCr-based alloy compared to the previous study on CoCr-based alloy formulation. This research work also offers an improved awareness of future work regarding this metal alloy, and simultaneously, it enhances excellent properties in physical and mechanical characteristics and also corrosion behaviour.

### **1.6 Thesis Structure**

This thesis is separated into five main chapters which are the introduction, literature review, methodology, results, and discussion, conclusion and recommendation.

#### **I. Chapter 1**

Chapter one focuses on the overall background of the study by emphasising a study on CoCrMo alloy properties fabricated by MIM. It includes the problem statement, research objectives, research scopes and expected a result from the MIM process by using CoCr-based alloy.

## II. Chapter2

Chapter two reviews the CoCr-based alloy especially on the history, properties and also the usage of CoCr-based alloy for biomedical application. The fabrication process of biomaterial alloy by Metal Injection method is also highlighted based on previous researchers especially the processing stage which is the debinding and sintering process. The primary concern in this work is in the MIM process. All the processes in MIM have reviewed starts with the selection of powder and binder, mixing process, injection moulding, debinding, and sintering process.

## III. Chapter 3

Then, the methodology of the present experiment is elaborated in this chapter.

## IV. Chapter4

All the findings are reported in Chapter 4. The properties result on the effect of each sintering conditions of CoCrMo ally compact under an argon atmosphere were discussed.

## V. Chapter5

Lastly, the conclusion and recommendation for the improvement of future work are given in chapter five.



## CHAPTER 2

### LITERATURE REVIEW

#### 2.1 Introduction

This chapter has concisely discussed the information of metallic biomaterials alloy, especially on CoCr-based alloy powder on fabricating compact by MIM and others powder-based manufacturing processes. The details on CoCr-based alloy as a biomedical material, MIM process, sintering method, characterisation of the alloy based on their physical and mechanical properties, microstructural analysis and corrosion behaviour were discussed on this topic. To complete this chapter, sources like journals, papers, reference books, and the internet are used to get further information that related to this research.

#### 2.2 Metallic Biomaterials for Powder-Based Manufacturing Processes

With the demand for implant devices such as joint replacements in the human body and as a medical tool for surgery, the metal and metal alloy biomaterials used by powder-based manufacturing process remain to grow. Figure 2.1 demonstrated the various percentage of utilisation of metal and metal alloy biomaterials through PM and AM processes, especially in biomedical applications. Those materials comprised of Ti and its alloys, CoCr-based alloys, 316L stainless steel, and other metal and metal alloys that currently becomes the focus in biomedical processes. The observations were taken starting from the year of 2000 to date, which then classified into three main phases that include; Phase 1 (2000-2005), Phase 2 (2006-2011), and Phase 3 (2012-2017). The finding served as evidence for the expansion in demand, particularly for metal and metal alloy biomaterials based-medical equipment through powder-based processing. Within the span of time as indicates in Figure 2.1, the titanium and its alloys followed by CoCr-based alloys materials have been abruptly increased in the production since the year 2000

to 2017. Nevertheless, 316L stainless steel showed a constant trend during the Phase 1, 2 and 3. Additionally, the request of others metal and metal alloys started to appear as the Phase 2 initiate followed by Phase 3 with a promising advancement.

Phase 1 involves the production of metal and metal alloy biomaterials from the year 2000 till 2005. The Ti and its alloy, CoCr-based alloy and 316L stainless steel were among the earliest biomaterials utilised by the powder-based manufacturing processes with 1.7, 0.9 and 2.6 % utilisation. In the first phase, the production of other alloys for medical implants is zero. Surprisingly, in Phase 2, the choice of metal and metal alloy biomaterials employed starts to grow with the addition of another alloys family. The other alloys consist of magnesium and nickel-titanium. The CoCr-based alloys as shown in Phase 2, its demand has been dominated by the growth trend with 11.3 % utilisation which is 10.4 % gain compared to the preceding phase. While the Ti and its alloys contributed to the progress of 9.6 % utilisation which was 7.9 % increment than the phase 1. The 316L stainless steel showed considerably lower demand in Phase 1 which is only 1.7 % utilisation. The demand for the 316L stainless steel has been improved to 4.3 % during phase 2 and remained stagnant when entering Phase 3. Amazingly, others metal and metal alloy biomaterials have shown significant increasing to 5.2 % from zero 0 % in demand before doubling up to become 10.4 % through Phase 3. Additionally, in phase 3, the titanium and its alloy have shown a tremendous increase of 23.4 %, which was double the value of its previous growth trend in Phase 2. On the other hand, the CoCr-based alloy also shows an increment demand up to 5.2 % in Phase 3. Its increment was higher than 316L stainless steel by 12.2 %. However, at Phase 1, 2, and 3, 316L stainless steel has shown a gradual trend which is only 4.3 % utilisation, while other metal and metal alloy biomaterials had increased about 5.2 % utilisation which is much higher than in Phase 2.

Metallurgists and materials scientists are seeking more innovative ways to improve the quality and longevity of surgical implants for the human body concerning materials used and their other benefits. Demanding properties such as material's toughness, fatigue resistance, and biocompatibility, give an ample promising for an implant in the human body. Therefore, metal and metal alloy biomaterials study in this review, such as Ti and its alloy and along with CoCr-based alloys had become a choices for medical implants includes in total joint-replacement systems and devices for fracture fixation (Bartolomeu et al., 2017; M. Z. Ibrahim et al., 2017; Kikuchi et al., 2017).

The understanding of biocompatibility has become a been the focus on for long-term implantable devices, which biologically sedentary and chemically inert so that they give no dangerous effect on the human tissues (Shang et al., 2017). Nevertheless, with a new development in biotechnology, a certain level of biological actions in the medical area, such as tissue engineering, drug and gene delivery systems, where direct contacts between biomaterials and tissue components are essential to be implemented in these days especially in the biomedical field.

One of the recent definitions of biocompatibility is the ability of a material to perform its desired function which concerning on medical therapy and without eliciting any undesirable local or systemic effects in the recipient or beneficiary. However, generating the most appropriate beneficial cellular or tissue response in that given situation, and optimising the clinically relevant performance of that therapy must be sufficiently concerned to avoid any risk that may harm human body (Bullard et al., 2008; Shang et al., 2017). In metal and metal alloy biomaterial, biocompatibility involves the acceptance of an artificial implant by the surrounding tissues and by the body. The metallic implants benefits make it not irritate the surrounding structures, not incite an excessive inflammatory response, not stimulate allergic and immunologic reactions, and it also does not cause cancer (Simoneau et al., 2017). Other functional characteristics that are necessary for the metal and metal alloy biomaterial implants include adequate mechanical properties such as strength, stiffness, and fatigue properties; and appropriate density. Since many applications of metal devices are for the structural implant, metal biocompatibility is of considerable concern since metals can corrode in an *in vivo* environment. The corrosion of biomaterial implant gives adverse effects on the surrounding tissues and to the implant itself. It produces chemical substances that harmful to human organs and deteriorates the mechanical properties of the implant. Therefore, the corrosion resistance of a biomaterial implant is a fundamental aspect of its biocompatibility. Even though, in particular cases, metals which can degrade are proposed for temporary implants, but probably biocompatibility requirement will not be ignoring easily (Mariot et al., 2016).

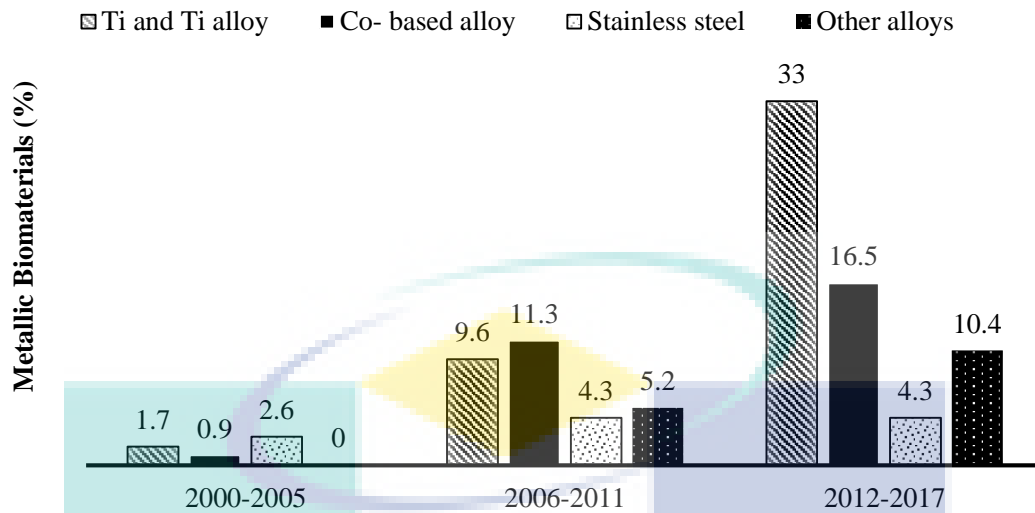


Figure 2.1 Trend of metal and metal alloy biomaterials for powder-based manufacturing processes for the year 2000-2017 (%)

### 2.2.1 Titanium and Titanium based alloys

In Phase 1 as indicates in Figure 2.1, the titanium and its alloys have manifested their presence as processed decorous metallic biomaterials for medical usage. The tremendous demand was due to their outstanding biocompatibility quality and biomechanical properties which make them as of great-value candidate in implantable applications. Hence, as the Phase 2 started representing the next six-year outcomes (2006 until 2011), the increment trend in the utilisation of the materials due to increasing activities were assessed especially with the ones related to the evaluation of mechanical properties and microstructure of titanium parts which mostly involved the additive manufacturing processes using SLM and DMLS (Y. Chen et al., 2017; Madhukar et al., 2017; Thavanayagam et al., 2015). The components made of titanium also has undergone both *in-vivo* and *in-vitro* studies for implantation in the human body, where the biocompatibility has been investigated. As progress to Phase 3, the titanium and its alloys have turned out to be the most established metallic biomaterials used in the powder-based processes. The increment was supported by the growing numbers of new titanium alloys with aluminium and vanadium-free for biomedical implants (J.-L. Wang et al., 2017).

Despite the fact that titanium and its alloys have offered many unique properties such as high specific strengths and high coefficient resistance to corrosion (Y. Chen et al., 2017; Madhukar et al., 2017), the focus is only confined to high-value products such as the aerospace and biomedical sectors. Consequently, the soaring cost of these prestigious

products can only be entirely justified (Thavanayagam et al., 2015; J.-L. Wang et al., 2017). Swiftly, the MIM is one of the processes that offered a solution to reduce the cost (Bolzoni et al., 2017) besides producing affordable titanium-based parts (Salleh et al., 2017). The innovative moulding technique was used to produce complex shaped components from the feedstock of metal powders with thermosetting or thermoplastic binders, which provide the required fluidity for successful injection moulding.

Although the titanium and its alloys have long been the favourite alloys in biomedical applications, the alloys have a potential for toxic effect especially in the permanent implant applications resulting from the released of vanadium and aluminium. Consequently, vanadium and aluminium-free alloys have been proposed as alternative titanium alloys for implant applications (Han et al., 2013; M. Wang et al., 2017).

### **2.2.2 CoCr-based alloys**

The living trend of the CoCr-based alloy is shown in Figure 2.1. The CoCr-based alloy marked its recognition in Phase 1 as one of the critical material options for powder-based processes for biomedical applications. In Phase 1, the CoCr-based alloy is one of the alloys that has been focussing for their properties and applications besides the titanium and its alloy and 316L stainless steel. In Phase 2, the utilisation of the CoCr-based alloy has risen and became the most extensively utilised metallic biomaterials. The primary study of the alloys in Phase 2 involved the investigation of the microstructure properties along with their corrosion resistance coefficient, and also the performance of other types of coating techniques. Subsequently, although the CoCr-based alloys were on the rising in utilisation demand in Phase 3, the alloys had been considered as the second most adopted metallic biomaterials after titanium, and its alloys due to the increased use of titanium and its alloys. From the inclination trend of the statistics shown in Figure 2.1, there were many of the researchers have utilised CoCr-based alloy for specific applications in the medical field, especially in dental and orthopaedic applications.

The CoCr-based alloy is considered as non-magnetic, wear, corrosion and heat-resistant (high strength even at elevated temperature) (Limmahakhun et al., 2017; Srivastava et al., 2017). Also, the alloys are difficult to be processed which make their usage limited. However, continuous efforts in the improvement of specific casting methods have been made (J. Li et al.; Xu et al., 2017). Due to its excellent resistance to degradation in the

oral environment, the first medical use of CoCr-based alloys was in the cast of dental implants (Darvish et al., 2016; Imran et al., 2017). The outcome from both *in vitro* and *in vivo* tests have shown that the alloys were biologically compatible with living tissue thus suitable for the use of surgical implant devices. Today, the use of CoCr-based alloys for implant and surgical applications had grown up to a prevalent practice especially related to orthopaedic prostheses for the knee, shoulder, and hip as well as for fracture fixation devices (Y. Lu et al., 2017; Trimble et al., 2017).

### **2.2.3 316L Stainless Steel**

As shown in Figure 2.1, the popularity of 316L stainless steel (316L SS) commences in the year 2000. In Phase 1, the researchers have shown an appreciation towards 316L stainless steel as affordable metal options that possess excellent properties. To date, the 316L SS has been used widely through several powder-based processes such as metal injection moulding, press, and sintered process. Besides, the material is a perfect candidate for aerospace and joining components such as screws and nuts, it employed in the medical field, particularly for human implant devices and surgical tooling. While in Phase 2 and Phase 3, though as compared to other metallic biomaterials, the used of the 316L SS is somewhat moderate as the interest in other metals such as titanium and cobalt-based alloys have still existed.

The 316L SS is one of the broadly investigated metallic biomaterials in medical applications because of its preferred properties (E Liverani et al., 2017; Mengucci et al., 2017; Y. Zhang et al., 2017). The steels are known for their excellent welding properties, joined by both fusion and resistance processes (Jinlong et al., 2017). Nonetheless, it is essential to make sure that copper and zinc do not become contaminants at the site of welds, as this can create cracks. Moreover, 316L SS alloy also contains low-carbon version and becomes the most preferable when dealing with anxious corrosive environments at a reasonable cost.

Furthermore, the 316L stainless steel also offers superior properties in corrosion and oxidation resistance. Hence, the 316L Stainless Steel alloy was found to be one of the most popularly used materials by metal injection moulding (MIM) process for biomedical applications (Choi et al., 2015; Choi et al., 2014b; Quinard et al., 2011). To date, almost all properties of MIM stainless steel parts improved as the density of the compacts increases. Nevertheless, the presence of porosity in the alloy matrix tends to reduce the



strength, ductility and corrosion resistance of components and thus, many efforts have been implemented to reduce the porosity level of sintered stainless steel (Dobrzański et al., 2017; Ertugrul et al., 2014; Hoeges et al., 2017).

#### **2.2.4 Other metal and metal alloy biomaterial**

Apart from the three aforementioned commonly used metallic biomaterials; titanium and its alloys, CoCr-based alloys, and 316L stainless steel biomaterial, the magnesium and nickel-titanium seemed to be vital in the modern biomedical research achievements. The expansion of these metal and metal alloy biomaterials is still at their early stage. However, there is a considerable possibility that magnesium and nickel-titanium will be developed further to be processed using powder-based techniques especially in orthopaedics applications (C. He et al., 2017; Montani et al., 2017).

The addition of these metal and metal alloys into any base in a metal can increase the properties of the metallic biomaterials by developing metastable which can intelligible with the particle's matrix dispersoids (Saedi, 2017; Saedi et al., 2017). Also, the present of the addition metal and metal alloys can also help to avoid recrystallisation besides stabilising the grain structure of particles. For example, the higher addition of zirconium than the usual amount used into the aluminium alloy can enrich their influence on the alloy properties for future potential when using the technology-related to powder metallurgy processes (Obadele et al., 2017).

### **2.3 The common parameter of metallic powder biomaterial**

Materials used for biomedical purposes exist in different forms, and they must possess specific properties to fulfil their intended role (M. Z. Ibrahim et al., 2017; Okulov et al., 2017). Materials such as metal and metal alloy biomaterials usually used for implantation. Therefore, their components must possess excellent properties which will enable them to deliver intended function inside the human or animal body (Dutta et al., 2017; L. Lu et al., 2014). Shortly, after the introduction of the 18-8 stainless steel in the 1920s, which has far-superior corrosion resistance to anything at that time, it immediately attracted the interest of the clinicians. Since then, the metal implants have experienced significant development and clinical use. Type of metal and metal alloy biomaterials used depends on specific biomedical applications applied nowadays. The 316L stainless steel (316L SS) yet the most used alloy in all implants division ranging from cardiovascular to

otorhinology (Raghavendra et al., 2015; Xiao et al., 2017). However, when the implant requires high wear resistance such as in artificial joints, CoCr-based alloys and Titanium alloy are good choices. Table 2.1 summarised the type of biocompatible metals used with a different set of parameters.

Based on Table 2.1, Ti and its alloys have the broadest range of particle sizes. The typical particle size employed by CoCr-based alloys, 316L stainless steel, nickel, and iron are higher than 20  $\mu\text{m}$ . The particle shape for the majority of the metallic biomaterials is irregular and spherical. While water and gas atomised powders are favourable powder fabrication processes utilised for metal and metal alloy biomaterials study in this review. These parameters are significant factors for the powder-based manufacturing process. Compare to water atomised, gas atomised powder fabrication for the biocompatible metal, and metal alloy powder is more preferable. It is because, this powder fabrication has great influences on the feedstock properties regarding performance, viscosity and other practical aspects. Moreover, as the size of particle increases, the feedstock's viscosity, especially in the metal injection moulding process, decreased, which it may enhance the stability of the powder processing in fabricating the implant parts. The properties of the final medical products further manipulated by several process variables such as density of the powder, sintering time and temperature, and addition of others metal and metal alloys.

The shape of metal and metal alloy biomaterials employed in powder-based processes as stated in Table 2.1 are mostly spherical and irregular based on the SEM analysis done by the researchers. Both particle shapes typically used for Ti and its alloys and 316L stainless steel. While for CoCr-based alloy, the typical particle shape used was spherical. For efficient powder-based processes, the suitable selection of biomaterials principally determined by the powder size and its shape (Dufaud et al., 2014). Frequently, for spherically shaped powder particles, the maximum amount of porosity limited to 50 % compared with the pore shape of the non-spherical powder. Besides, the geometric of the particle shapes also influenced the rheology characteristics, and feedstock flow consequences, as well as the mechanical properties of manufactured parts. The spherical particle shape is a better choice compared to irregular as it led to more significant densification during compaction or consolidation stage in the powder-based processes. Nevertheless, the unique features of irregular particle shape offer a high-feature retention in the compact (Mirzaei et al., 2017). Once compacted, the irregular particle shape offered better interlocking feature between particles which resulted in excellent mechanical



properties. Alertness of particle size dissemination hits precarious fragment in the manufacture of homogeneous missing of powder metal during the powder-based process (Al-Rashidy et al., 2017).

Table 2.1 Common powder parameters of metallic biomaterials

	Particle size ( $\mu\text{m}$ )	Particle shape	Powder fabrication method	References
<b>Ti and its alloy</b>	1 - 300	Irregular spherical	Gas atomised	(Bolzoni et al., 2014; Bolzoni et al., 2013, 2015; L.-j. Chen et al., 2009; Guoxin et al., 2008; Han et al., 2013; Hayat, Wen, Zulkifli, et al., 2015; Ismail et al., 2012; Khanlari et al., 2017; B. Q. Li et al., 2013; Liu et al.; Málek et al., 2013; Nouri et al., 2010; Nyberg et al., 2005; Obasi et al., 2010; Raza et al., 2015; Scott Weil et al., 2006; Song et al., 2012; H. Sun et al., 2014; Torres et al., 2014; X. Wang et al., 2013; Yablokova et al., 2015; Yadroitsev et al., 2014; Yan et al., 2015; L. C. Zhang et al., 2011; Zhao et al., 2015)
<b>CoCr-based alloy</b>	4.44 - 200	spherical	Water atomised, gas atomised	(Bedolla-Gil et al., 2009; Dourandish et al., 2008; Fox et al., 2008; Girardin et al., 2016; Grądzka-Dahlke et al., 2008; G. He et al., 2016; Hedberg et al., 2014; Henriques et al., 2015; Koseski et al., 2005; S.-H. Lee et al., 2005; E. Liverani et al., 2016; Mohd Afian et al., 2014; Murakami et al., 2010; P. Vieira Muterlle et al., 2009; P. V. Muterlle et al., 2009; Rodrigues et al., 2011b; Takaichi et al., 2013; Xin et al., 2014)
<b>316L stainless steel</b>	1.83 - 80	Irregular, spherical	Gas and water atomised	(Aboulkhair et al., 2016; Gulsoy et al., 2015; Ji et al., 2001; Kan et al., 2014; Koseski et al., 2005; Manonukul et al., 2010; Raza et al., 2016; M. Rafi Raza et al., 2012; Z. Sun et al., 2016; D. Wang et al., 2013; Yadroitsev et al., 2011)
<b>Other alloys</b>	2.5 - 200	Irregular	Gas atomised	(Čapek et al., 2014; Choi et al., 2014a; Garcia-Cabazon et al., 2017; Imai et al., 2017; Kayhan et al., 2016; Lang et al., 2016; W. Li et al., 2016; Loh et al., 2015; Y. Lu et al., 2015; Madeira et al., 2017; Mariot et al., 2016; Ng et al., 2011; Páez-Pavón et al., 2016; Tahmasebifar et al., 2016; Thomas-Vielma et al., 2008; Yazdimamaghani et al., 2017; Yoon et al., 2016; Youhua et al., 2010; Zhou et al., 2016)

## **2.4 Properties of CoCr-based alloy**

From the periodic table for transition group VIII, the metallic element of cobalt acts as the central member of the ferromagnetic trio, cobalt, iron, and nickel. Cobalt has a varied series of useful uses, nonetheless practically all of these comprise its practice as an alloying component or as a chemical compound; the pure metal has a limited applications but is significant as a metal for scientific study, is mainly characterized by its ferromagnetic properties with an exclusively high Curie point, its hexagonal crystal form at average temperatures, converting to cubic at higher temperature, and its small stacking-fault energy (West, 1982). The Swedish chemist Brandt insulated the metal in 1735 and introduced the scientific study of the element, while its true element nature was not well-known up until it had been widely studied about 40 years later by Bergman (West, 1982). The physical and mechanical properties of metallic cobalt are mostly liable to distinctions due to the undefined structure after the sluggishness of the cubic-to-hexagonal transformation of the metal alloy.

### **2.4.1 CoCr-based alloy for biomedical applications**

The metallic element cobalt appears as the middle member of the ferromagnetic Cobalt-base alloys were first used in the 1930s as said before. The CoCr-based alloy Vitallium was used as a cast dental alloy and formerly implemented to orthopaedic applications starting in the 1940s. The corrosion resistance of this alloy is more than an order of magnitude better than that of stainless steel, and it has high mechanical property. The four leading alloys used are Co-28Cr-6Mo casting alloy, ASTM F75, Co-20Cr-15W-10Ni wrought alloy, ASTM F90, Co-28Cr-6Mo thermomechanically processed alloy with a composition closely duplicate to ASTM F 75, ASTM F799 and Co-35Ni-20Cr-10Mo wrought alloy, ASTM F 562 (Cramer et al., 2006).

In order to produce a wrought cobalt-chromium alloy, carbon must be reduced compared to the level in cast alloys (0.05% versus approximately 0.25% or higher). Low carbon contents mean that less strengthening is produced by carbides. Alloys produced for structural applications such as hip prostheses can be forged if optimal properties are desired; this process results in maximum strength and toughness for cobalt-chromium alloys but may not produce uniform grain sizes. These alloys are difficult to machine, closed-die forging can minimise machining requirements, but wrought components still

may require more machining than cast components. Consequently, investment casting often is used to produce cobalt-chromium implants at lower cost (Cramer et al., 2006). The preferred method to produce implants of cobalt-base alloy will be a function of the trade-off between cost and properties. Where the properties of casting are sufficient, casting will dominate, when maximum strength is required, hot pressing and forging will rule. Table 3.4 shows some mechanical properties of these alloys (Cramer et al., 2006).

Table 2.2 Typical properties of cast and wrought cobalt-base alloys

ASTM designation	Condition	Young's Modulus (Gpa)	Yield strength (Mpa)	Tensile Strength (Mpa)	Fatigue endurance limit
F75	As cast/Annealed	210	448-517	655-889	207-310
PM HIP (a)	253	841	725-950	1277	
F799	Hot Forged	210	896-1200	139-1586	600-896
F90	Annealed	210	448-648	951-1220	Not available
44% cold worked	210	1606	586	1896	
F562	Hot Forged	232	965-1000	1206	500
Cold worked, aged	232	1500	689-793	1795	

PM: HIP, hot isostatic pressing. (b) Axial tension, R=0,05, 30 Hz.

Source: Cramer et al. (2006)

MIM is one of the expertise method practice to fabricate this metal alloys. The focal aspects that create MIM as a competitive technology versus investment casting and machining are cost. Applications such as femoral components, tibial trays, and cable crimps, represent a challenge regarding their size, material performance, and biocompatibility issues.

#### 2.4.2 ASTM F75

Commonly used commercial/proprietary names to describe this alloy include Vitallium and Haynes 21 (HS21). Cobalt-chromium-molybdenum-carbon alloys are used in aircraft engines and surgical implants. These alloys are known for high strength and excellent wear resistance, but their primary attribute is the corrosion resistance in chloride environments, which is related to their bulk composition (principally the high chromium content) and the surface oxide (nominally Cr<sub>2</sub>O<sub>3</sub>). When F75 is cast into shapes by investment casting, the alloy is melted at 1350 to 1450°C and then poured into ceramic moulds (Ratner et al., 2004). In the case of the F75 produced by MIM, the sintering behaviour of this alloy is of critical importance to obtain a high-performance product.

Some of the variables affecting the sintering response of this alloy are the starting particle size, chemistry, and the sintering atmosphere (Tandon et al., 1999). The high sintering temperature in a MIM process is needed to obtain a high sintered density (more than 95 %) and a homogeneous microstructure. Within the relatively broad ASTM F75 chemistry specification, it is important to note that minor variations in levels of carbon can lead to significantly different sintering response and, hence, can affect density and mechanical properties. From a sintering standpoint, process control is much easier for a material containing little or no carbon, versus one requiring carbon within a tight tolerance. However, it is known that carbon is required to impart strength in F75. Hence, process control is expected to be a challenge concerning the sintering atmosphere (Tandon et al., 1999). A higher carbon content (0.3-0.35 % C) promotes the formation of eutectic liquids which activate sintering; therefore sintering temperature is lower than in the case of a low carbon alloy (Vieira Muterlle, 2010). As-cast F75 alloy typically has an f.c.c matrix (cubic phase), while as sintered F75 is usually hexagonal. The microstructure presents interdendritic and grain- boundary carbides (primarily  $M_{23}C_6$ , where M represents chromium or molybdenum). There can also be interdendritic cobalt and molybdenum-rich sigma intermetallic and cobalt-base gamma phases (Cramer et al., 2006). If none equilibrium cooling occurs during solidification, a cored microstructure can arise. In this situation, the interdendritic regions result in solute (chromium, molybdenum, carbon) enriched and contain carbides, while dendrites become chromium depleted and richer in cobalt. This is an unfavourable electrochemical situation, with the chromium-depleted regions being anodic concerning the rest of the microstructure. Coring also results in small differences in the mechanical properties between the cobalt-rich dendrites and the chromium-rich interdendritic regions. Subsequent solution annealing heat treatments at 1225°C (2235°F) for 1 to 3 hour can help alleviate the problems associated with coring (Cramer et al., 2006). A further feature of cast cobalt implant alloys is the extremely large grain size observed in the original castings. This problem is particularly severe in castings having a large cross-section, because here any chilling effect from the mould wall is quickly lost, and the remaining liquid solidifies slowly, resulting in coarse grain size (Williams et al., 1990). The large grain size is a feature of MIM parts too. Examples of microstructures of as cast, as sintered and wrought materials are shown in Figure 2.2.

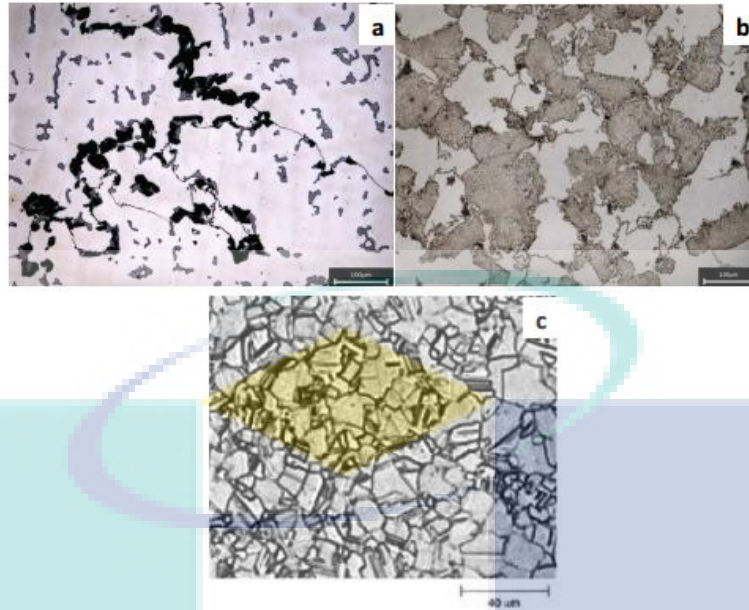


Figure 2.2 Microstructure of as-cast (a) and as sintered (b) F75 alloys with 0.35% C  
Microstructure of forged high- strength Co- Cr- Mo alloy (c)

Source: Klarstrom et al. (2004)

## 2.5 Parameters of metal injection moulding (MIM)

Table 2.3 shows parameters for the metal injection moulding process for each metal and metal alloy biomaterials which are Ti and its alloys, CoCr-based alloy, 316L stainless steel and others alloy. Metal injection moulding offers high potential, fabricating a fine-grained assembly and excellent mechanical properties, in some instances beyond the properties of wrought or cast materials (Thavanayagam et al., 2015). The methods for manufacturing components for biomaterial powders in this process separated into two group; the blended elemental (Lin et al., 2017; Liu et al.), and the pre-alloyed methods. In the blended elemental, for example, titanium sponge fines, which a by-product of the commercial titanium reduction process, will be mixed with the base powder and binder. The first step in the MIM process is by mixing the powder with selected binders. From Table 2.3, the conventional binders used in Ti and its alloy are mostly involves the thermoplastic binders such as Stearic Acid (SA), Paraffin Wax (PW) , Naphthalene, polyethylene (PE), polymethyl methacrylate (PMMA), High Density Polyethylene (HDPE), Low Density Polyethylene (LDPE) and Polyethylene glycol (PEG). The same conditions applied for CoCr-based alloy, where most of the binders used are similar, and as indicates in Table 2.3, polyolefin and organic binders which are Palm Stearin binder also been used. For 316L Stainless Steel alloy and others alloy, most of the binders used



are the same as stated in Ti and its alloys. After the mixing process, the feedstock was prepared for injection moulding to produce green compacts.

Then, the green compact will go for the debinding process. There are two steps in the debinding process, which are solvent debinding and thermal debinding (G. Chen et al., 2013; Md Ani et al., 2014; Zaky, 2004). From Table 2.3, in Ti and its alloys, solutions used to immerse the green compacts were consisting of hexane, chloroform, methylene dichloride and water bath distilled water. For CoCr-based alloy and 316L Stainless Steel alloy, heptane is the most common solution used. While, for others alloy apart from heptane, hexane is employed in the process as a solvent. During solvent debinding, for Ti and its alloy, the soaking time used to remove the binder is from 1- 20 hour with the debinding temperature used is from 40 until 313°C. Differ from CoCr-based alloy, where the soaking time is about 4-10 hour with the common used debinding temperature is between 40 -90°C. While for 316L Stainless Steel and others alloy, 5 and 8 hour soaking time were applied for 45-60°C and 25-60°C temperature for debinding. After solvent debinding, the brown compact was then introduced for the thermal debinding process where this compacts would create a higher risk due to the loss of the binder component. Therefore, cautioners to hold the compact must be applied.

For Ti and its alloys, based on Table 2.3 below, the typical soaking temperatures of the thermal debinding process is between 40 to 313°C, and the compacts were heated up for 1 until 20 hours soaking times. While, the thermal debinding temperature for CoCr-based alloy is frequently in a range of 450 to 600°C, where the compacts are heated to become the brown compacts for 1 until 3 hours soaking time. The range of thermal debinding temperature for 316L Stainless Steel alloy was between 450-1350°C, and average range for soaking time is between 1 to 2 hours. For others, alloy, thermal debinding temperature and soaking time that is commonly used are from 250 – 400°C for 1 until 4 hours. Brown compacts after debinding were then sintered in a variety of different atmospheres and sintering conditions depending on the combination of properties required.

From Table 2.3, frequently sintering atmospheres applied for each alloy which is Ti and its alloy, CoCr-based alloy, 316L Stainless Steel and others alloy were consists of Argon, Vacuum, Hydrogen and Nitrogen. Then, compacts will be sintered in a furnace with specified sintering temperatures and time depending on the metal alloy used. For Ti and its alloy, the typical sintering temperatures used is from 750- 1500°C and were

sintered for 1-48 hour for 2-10°C/min heating rate. While, for CoCr-based alloy, the sintering temperature range is from 1200- 1400°C heated up until 1- 2 hour sintering time for about 0.3 until 10°C/min range of heating rate. Then, 1200 until 1390°C sintering temperatures were applied for 316L Stainless Steel alloy at 1- 2 hour sintering time for 3-20°C/min range of heating rate. Next is for others alloy, the common sintering temperatures and times used are from 500 until 1650°C for 2 hours at the heating rate between 5-10°C /min.

Initially, in the MIM process, powder metal is mixed with a binder to form the homogeneous feedstock. Feedstock homogeneity does promote dimensional consistency of injected parts and helps to prevent such defects as binder separation and powder segregation. Role of binder systems itself is like a transporter which is helpful to form the metal powder into the desired shape. After mixing, the feedstock in pellet form poured into the hopper of the injection moulding machine. The feedstock melted, then injected into the mould cavity and solidified before ejected out from the mould as a green compact which replicates the shape of the mould cavity. The green compact can then be debound at specific temperatures and times. The compacts then were subjected to thermal debinding and sintering process. During this phase, the metal particle bonding occurs by solid state diffusion.

Then, the part was then debound, eliminating all binder, and sintered conventionally to give entirely solid components (Darvish et al., 2016). Whether the compacts were sintered in argon, vacuum or nitrogen atmosphere, they were reliable to achieve a sintered compact of 98 to 99 % of the theoretical density. However, in few studies said that the effect of nitrogen on the microstructure and mechanical properties of a CoCr-based alloy determined the formation of finer carbides. As a consequence, the increase of nitrogen content in the alloy improve some mechanical properties, like the yield strength, tensile, fatigue strengths and the hardness. The sintering process can increase the final density, but a limited remaining porosity was remained an issue due to impurities during reduction process (Čapek et al., 2014; Ebel et al., 2017). In MIM, the variables of the production process such as sintering temperature, sintering time, and sintering atmosphere were continuously diminished, and the addition of alloying elements to the steels to increase corrosion resistance was explored (Hsu et al., 2005).

Table 2.3 Parameters of metal injection moulding for metallic biomaterials

Materials		Ti and its alloy	CoCr-Based alloy	316L SS	Other alloys	References
<b>Binders</b>		EVA, SA, PW, PE, HDPE, PEG, PMMA, LDPE	An organic binder, Polyolefin based, EVA, SA, PW, Zr, HDPE, PP, Palm stearin, PE	An organic binder, PE, PW, SA, CW, EVA, PP, PMMA,	HDPE, PW, SA, EVA	(Ahn et al., 2009; Dourandish et al., 2008; Guoxin et al., 2008; S.-H. Lee et al., 2005; D. Li et al., 2009; Manonukul et al., 2010; Nyberg et al., 2005; M. Rafi Raza et al., 2012; Sidambe et al., 2012; Youhua et al., 2010)
<b>Solvent debinding</b>	Solution	Chloroform, methylene dichloride, water bath of distilled water, hexane	Heptane	Heptane	n-Heptane, hexane, CH <sub>2</sub> CL <sub>2</sub>	(L.-j. Chen et al., 2009; Guoxin et al., 2008; Koseski et al., 2005; Mohd Afian et al., 2014; Obasi et al., 2010; M. Rafi Raza et al., 2012; Shu et al., 2006; Thomas-Vielma et al., 2008; Wahi et al., 2016; Youhua et al., 2010)
	Time (h)	1-20	5-10	5	8	
	Temperature (°C)	40-313	40-90	45-60	25-60	
<b>Thermal debinding</b>	Time (h)	1	1-3	1-2	4-15	(Baojun et al., 2002; L.-j. Chen et al., 2009; Choi et al., 2014a; Dourandish et al., 2008; "Effects of silver on the microstructure of sintered nickel-copper-zinc ferrites," 1993; Ismail et al., 2012; Ji et al., 2001; Koseski et al., 2005; Manonukul et al., 2010; Mohd Afian et al., 2014; Murakami et al., 2010; P. V. Muterlle et al., 2009; Obasi et al., 2010; M. OMAR et al.; Onbattuvelli et al., 2014; M. Rafi Raza et al., 2012; Raza et al., 2015; Shu et al., 2006; Sidambe et al., 2012; Wahi et al., 2016; Youhua et al., 2010)
	Temperature (°C)	350-720	450-600	450-1350	250-600	
<b>Sintering</b>	Atmosphere	Argon, vacuum, hydrogen	Nitrogen and hydrogen, argon, vacuum	Hydrogen, nitrogen, argon, vacuum	Air, vacuum, hydrogen	(L.-j. Chen et al., 2009; Dourandish et al., 2008; "Effects of silver on the microstructure of sintered nickel-copper-zinc ferrites," 1993; Gulsoy et al., 2015;
	Time	1-48	1.5-20	1-2	2	



Temperature	750-1500	1200-1400	1200-1390	500-1650	Hayat, Wen, Zulkifli, et al., 2015; Ismail et al., 2012; Ji et al., 2001; Koseski et al., 2005; D. Li et al., 2009; Manonukul et al., 2010; Mariot et al., 2016; P. V. Muterlle et al., 2009; Nyberg et al., 2005; Özbilen et al., 2016; Raza et al., 2016; Youhua et al., 2010; Zhao et al., 2015)
Heating rate	2-10	0.3-10	3-20	5-10	

## 2.6 Metal injection moulding (MIM)

MIM method is a root of the plastic and injection moulding. In MIM, metal powders are mixed with various thermoplastic binders, then injected into a mould cavity and, after binder are removed by the debinding process, parts are sintered to produce high-density metal parts for the desired shape required. About 28 years ago, for the first time, this machinery was recommended on the industrial level. MIM has been a talented process to develop into an established commercial technique for the fabrication of complex and small and shapes.

## 2.7 The process

Figure 2.3 shows a schematic diagram of the MIM process. The metal powders are mixed with a binder's component which usually comprises polymers and waxes to produce feedstock. This feedstock is then pelletized to form pellet feedstock that can be moulded using an injection moulding machine (Vervoort et al., 1996). MIM process can be separated into 4 main stages, which are mixing and pelletizing, injection moulding, debinding, and sintering.

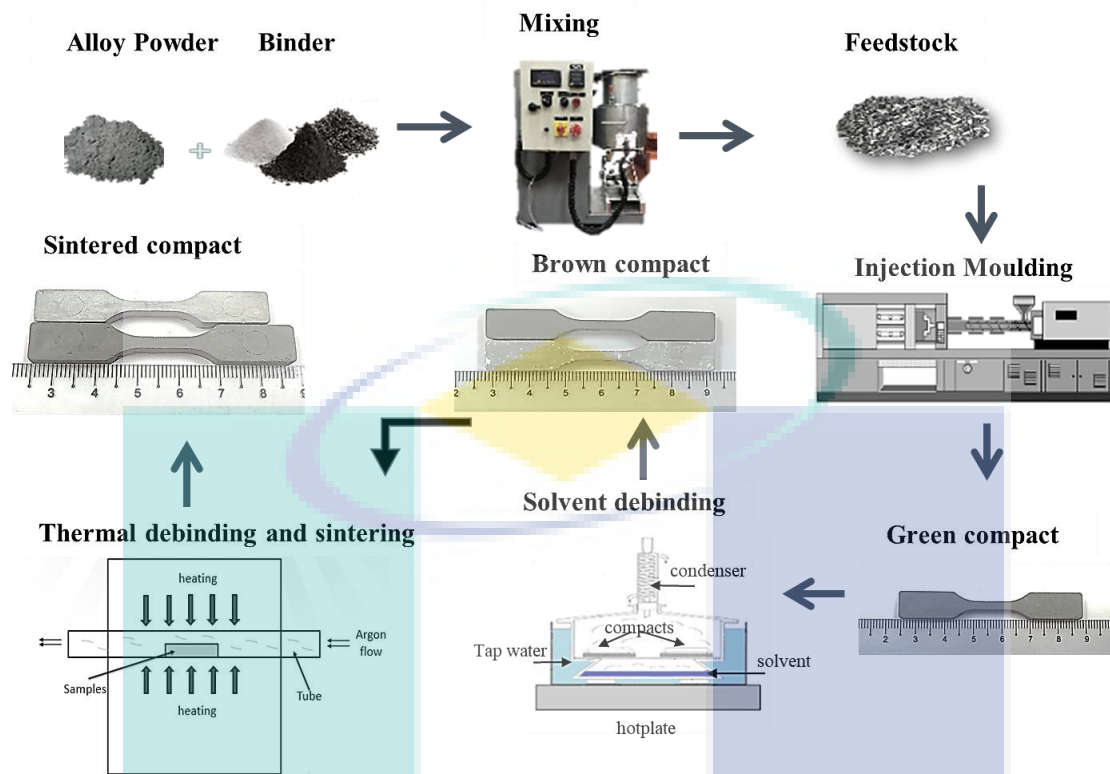


Figure 2.3 Metal Injection Moulding Process

### 2.7.1 Mixing and pelletizing

Mixing of the powder and binder's component is compulsory to form the homogeneous feedstock for injection moulding. The objectives in the mixing process are to melt the powder's particle with the binder, avoid agglomeration, and to reach even distribution (Randall M German, 1990). Mixing is usually carried out in either in mixers, such as twin screw extruders, continuous mixers, sigma- blade mixers, or any suitable mixer that can be used to mix powder and binder. They were mixed at temperatures above the melting points of the binder's components. The homogeneously mixed feedstock is cooled to room temperature and made into pellets forms for transport and storage (Randall M German, 1990). This is required since in most circumstances the mixing process is separated from the moulding machine, and palletization is used to formulate a uniformly sized material for the moulding operation. There are two intentions in pelletizing or granulating MIM feedstock. At first, it aims to make the feedstock easily transported which can be loaded automatically into the moulding machine. Secondly, to combine the used material back into the moulding process. The used material derives from runners, sprues, and inappropriately moulded parts (earlier to debinding) (Randall M German, 1990).

### 2.7.2 Characteristics of feedstock

In MIM, the powders used are much improved than those in conventional Powder metallurgy technique. For metal powders, it has an average size of 5-10  $\mu\text{m}$ , and particle size is generally  $<20 \mu\text{m}$ . This is a decent approach to enhance homogeneous distribution of the particles in the mixed feedstock in such a way that it has the excellent mixture of viscosity and flow under injection moulding conditions for uniformity of die filling.

As the sintering rate is inversely proportional to the fourth power of the particle size, densification and sintering of the part will take place more rapidly (Vervoort et al., 1996). The higher volume of powder loading (about 60% for powder metals) with a tolerable flow will minimise the debinding pattern and also improve the dimensional control so that sintering shrinkage can be measured more easily. Thus, the use of high packing density systems made up of various size spherical particles (S. H. Lee et al., 2008) is needed. This means that powders with either a very wide or a very narrow particle size distribution are favoured. Water and gas atomised and carbonyl powders are the three more frequently used powders. For this process, the particle morphology is the primary key. In specific, for improving rheological properties of the feedstock, smooth and rounded particles, as produced by carbonyl process or the gas atomization, are desired. Occasionally, more irregular powders are required to enhance the shape retention and green strength throughout sintering (Kaysser et al., 1993); in this situation, water atomised powders should be considered. As a result, the geometry and the size are the controlling aspects of whether a material can be injection moulded or not. The achievement of MIM is mostly determined by the suitable choice of binder's component. It should act as a carrier and flow medium for the high volume of fine powder loading throughout mixing and injection moulding. The binder must feature good wettability of the powder for easy mixing, high strength of the moulded material (green part) and should avoid segregation during injection moulding (Vervoort et al., 1996). After moulding, the binder has to be detached without damaging the integrity of the part or cause-effect on the properties of the part. Decomposition of the binder must be progressive. This combination of characteristics can only be gained by some component to form a multi-component binder. In a conventional classification, there are five categories of binders used in MIM, most of which are polymers includes water-based systems, thermosetting

compounds, thermoplastic compounds, gelation systems and inorganics binder (Randall M German, 1990).

### 2.7.3 Debinding process

Debinding is the method where the binder is detached from the part before sintering. Cracking of compact is an outcome of a failure in the step of debinding. From (Gorjan et al., 2014), one of the time-consuming and challenging phase in the metal injection moulding process is eliminating the binder from the green compacts, without causing any cracks or deformation. The debinding process is tough because large amount of poorly volatile binder of green compacts in the solid state, i.e. below the melting point. Removal of the binder without have the particles dislocated is a subtle process that is best completed in a few stages. Primarily the binder keeps the powder particles together. When the binder is heated, it softens and is incapable of enduring shear stress from thermal gradients, gravity or internal vapour pockets. To hold part's shape, inherent particle-particle friction is desirable. The binder should be removed from the pores as a fluid (liquid or vapour) without contaminating or distorting the part (Randall M German, 1990). In Figure 2.4, an ideal debinding process is represented in a compact shaped from monosized spheres.

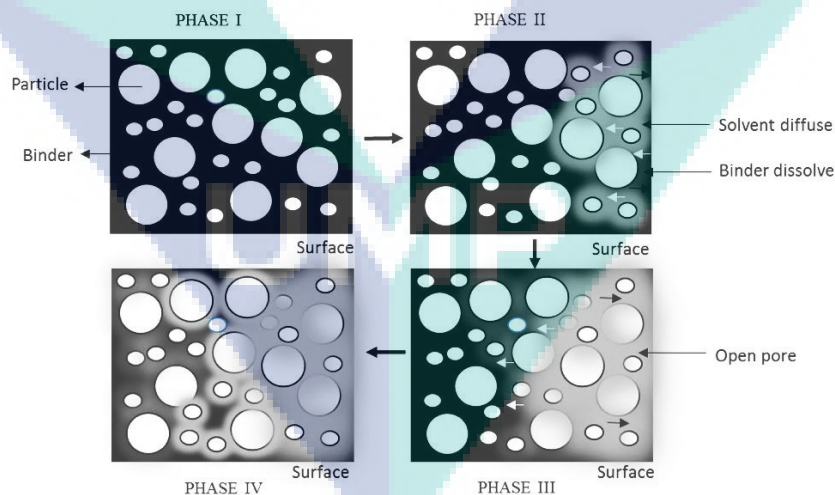


Figure 2.4 Debinding process

Debinding is commonly reached by gradually heating the green compacts, causing the binder to vaporise and decompose. The complications are particularly severe in low-pressure injection moulding, as the binder does not have a backbone polymer that would hold the particles firmly in place during the debinding. Debinding binders in two phases

are critical to retaining the shape of injected parts; the resulting decomposition affects the rigidity and strength of a structure. Hence, the aim in debinding is to remove the binder in the shortest time with the minimum impact on the compact (Md Ani et al., 2014). The extraction or leaching of one binder component forms porosity in green bodies. A huge amount of open porosity, after solvent debinding, permits the degraded minor binder to diffuse to the surface effortlessly. Therefore, the thermal removal of insoluble binder components will be ended in a much shorter period without exposing the integrity of the green compacts. Thus, the combination of solvent debinding and thermal debinding can be time saving (Banerjee et al., 2012; Randall M German et al., 1997). Several authors considered different variables affecting the solvent debinding process but they retain the solvent to feed ratio constant. Later, White and German (Randall M German, 1990) initiate that a high powder loading required a long solvent debinding time to remove the wax from the binder.

There are six debinding methods, includes of solvent and thermal processes, as listed such as Thermal debinding; permeation (high pressure), diffusion (low pressure) and wicking (capillary flow), while solvent debinding; high pressure (supercritical), extraction (immersion) and thermally assisted (solvent and heat). Thermal debinding is the calmest to visualise. The part is slowly heated to decompose the binder. One of the keys to debinding is to practise a multicomponent binder system that decomposes gradually over some phases so that eliminating a primary binder constituent leaves enough quantity of a second constituent to hold the particles in place. The most popular approach is to immerse the component in a solvent that dissolves some binder, thereby leaving some polymer behind to hold the particles in place for subsequent handling and an open pore structure for subsequent debinding by evaporation. The remaining binder is formatting.

#### **2.7.4 Sintering process**

Certain processes that define themselves as “sintering” (such as Direct Metal Laser Sintering) are actually melting materials- which can be a reason to the misperception surrounding the two processes (sintering and melting). The process of liquefying metal is frequently used when joining two metals, similar to sintering. In common terms, sintering has many different uses. One of the key function of sintering is to join metal particles together. Practically, this process usually used on metals by high

melting point, as it doesn't depend on reaching melting temperatures to work. Sintering also can improve the properties of certain materials as it can reduce the porosity of an object's surface. While, melting in contrast, also has many benefits depending on the material being melted. Another use of melting is to fully liquefy a metal alloy to reform it into a new shape or to change some of its physical characteristics. In most manufacturing applications, melting is more commonly used to fuse two objects or to reform a metal than it is to change object properties. So, while sintering and melting have similarities, they are in fact two different processes that have different applications.

In MIM, sintering is the last stages in this process, which can be combined directly during the thermal debinding cycle. Powder particles bond together during sintering when heated to specific high temperatures, leading to densification. On a microstructural scale, this bonding happens as interconnected necks (weld bonds) developed at the points of contact between particles (Randall M German, 1990). Figure 2.5 shows necks formed between sintered nickel spheres. Such neck growth effects all of the significant property changes related to sintering. Figure 2.5 demonstrates the changes in microstructure when the necks grow between the particles (necks enlarge and merge). The point that the used of powders are much finer in MIM than those used in PM means that sintering takes place more eagerly because of the higher surface energy of the particles (Heaney, 2012). Regularly sintering aids the double part of chemical homogenization and densification, when elemental powders or master alloys are used to produce an alloy.

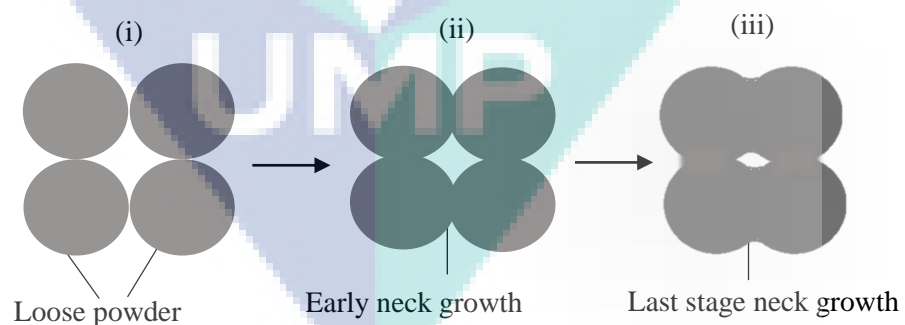


Figure 2.5 Neck formation and microstructure changes when necks growth

As the “brown” part is particularly porous, a very high shrinkage happens during sintering. Therefore the temperature of sintering must be very carefully controlled to maintain the shape and prevent slumping’. Typically, shrinkage during sintering is isotropic and uniform, so the moulded component is large to gain the preferred last



dimensions. The identification of significant process parameters during sintering of brown parts in Metal Injection Moulding (MIM) is essential because improper control of these parameters can result poor parts. Whereas, for the sintering process, unappropriated sintering parameters; temperature, time, heating rate and atmosphere stated by (R. M. German et al., 1992) caused the formation of closed spherical pore besides further shrinkage of the compacts will become very difficult in the final stage. Additionally, some compacts are inspected to have an air contact with surrounding and cause a high level of impurities to occur within the compacts which are detrimental to the density and properties of final compacts. At higher sintering temperatures, creep happens to lead to distortion but not cracking. As the component mass decreases, these high-temperature problems are less evident. The primary function of the sintering temperature is to protect metal parts from the effects of air contact which leads to pores elimination. While, for the holding time, not much study was discussed on that. However, from (Limberg et al., 2012; Palermo, 2014) when the green compact is formed through low-pressure shaping which is MIM process, the suitable sintering temperature suggested were (in a range of 1200-1360 °C) and the holding time may also be longer which is (between 90-180 min).

For the sintering process, it is vital that all binder's component is removed during the initial sintering stages. If binder remains, mostly tar and graphite, are left when the pores are closed, they will be fused in the last compact (Vervoort et al., 1996). The MIM technology offerings a very high dimensional control than PM process after sintering, where shrinkages of the compact up to 12 to 18%. If the powder structure is shaped homogeneously, then sintering is constant and final dimensions can be alleged to near measurements (Randall M German, 1990). After sintering, the part has good strength, with properties near or even superior to those existing from other processing methods. The density is almost to the theoretical one, typically about 90%. Final densification can be supported by both cold and hot deformation, including hot isostatic pressing. Other post- sintering steps include plating, drilling, coining, machining, reaming, passivation, and also heat treatment. Options in heat treatment include precipitation hardening, tempering, carburising and nitriding.

## 2.8 Characterisation of CoCr-based alloy

### 2.8.1 Physical and mechanical properties

#### 2.8.1.1 Hardness properties

Figure 2.6 shows the methods for measuring hardness in this research. Where a square base diamond pyramid is used as the indenter. The included angle between the opposite faces of the pyramid is  $136^\circ$ . As a consequence of the indenter's shape, the dimple on the surface of the specimen will be a square form. The length of the diagonal of the square is measured over a microscope fitted with an ocular micrometre that comprises of movable knife-edges. The loads are between 1 and 1000 g which referring to the microhardness test. The Vickers hardness values (HV) are calculated by the Equation 2.1 below;

$$HV = \frac{2P_{HV} \sin \frac{\alpha}{2}}{d^2} = 1.8544 \left( \frac{P_{HV}}{d^2} \right) \quad 2.1$$

The value of diagonal length ( $d$ ) can be obtained from the mean value of the diagonals as shown in Equation 3.10.

$$d = \frac{d_1 + d_2}{2} \quad 2.2$$

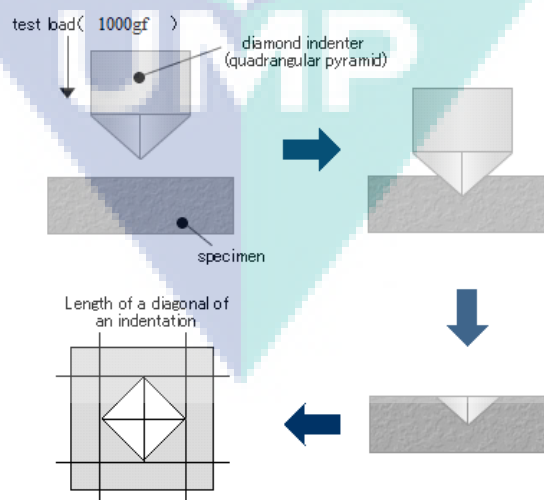


Figure 2.6 Vickers Hardness Test Schematic diagram



The hardness at a room temperature of cobalt has been reported to be between 140 and 250 HV. For well-annealed compacts of high-purity metal, the values are between 140 and 160 HV. The variation of hardness with temperature does not present an inflexion at the transformation temperature. Microhardness measurements on zone-refined single crystals have given results critically dependent on crystal orientation, and the values obtained varying from 81 to 250 HV. The low values are associated with deformation by slip on the basal planes of the hexagonal form, high values with twinning (West, 1982).

### 2.8.1.2 Tensile properties

The tensile test is practice to estimate the strength of metals and alloys. For a short time at a constant rate, plastic or metal compact is pulled to failure in this test. Before the test is conducted, the lengths of the specimen need to be identified by making two small punch mark. The capability of a material to endure breaking from tensile stress is one of the most significant and extensively measured properties of materials used in structural applications.

From the data recorded, the nominal or engineering stress is obtained by dividing the applied load,  $P$  with the specimen's original cross-sectional area,  $A_0$ .

$$\sigma = \frac{P}{A_0} \quad 2.3$$

Then, nominal or engineering strain is obtained by dividing the change in the specimen's gage length,  $\delta$  ( $\delta = L - L_0$ ) by the specimen's original gage length,  $L_0$

$$\varepsilon = \frac{\delta}{L_0} \quad 2.4$$

From the tension test data, it is potential to calculate several values of the stress and corresponding strain in the specimen and hence, the results are plotted. The stress-strain diagram was formed from the resulting curve. The ultimate tensile strength, yield strength, breaking strength and elastic or Young's modulus of material can all acquire from this curve. The graph shown in Figure 2.7 is a representative curve for metallic behaviour. At small strain values (the elastic region), the bond between stress and strain is approximately linear. Within this area, the slope of the stress-strain curve is defined as the elastic modulus. As many metal absence a sharp yield point, i.e. a sudden,

recognisable transition among the elastic region and the plastic region, the yield point is frequently defined as the stress that gives rise to a 0.2 % permanent plastic strain. By this convention, a line is drawn parallel to the elastic region of the material, starting at a strain level of 0.2 % strain (or 0.002 mm/mm.). The point at which this line intersects the curve is called the yield point or the yield stress. The ultimate tensile strength, in contrast, is obtained by measuring the maximum stress extended by the material. The total work of elastic deformation is a measure of resilience, where *Modulus of Resilience*,  $U_r$

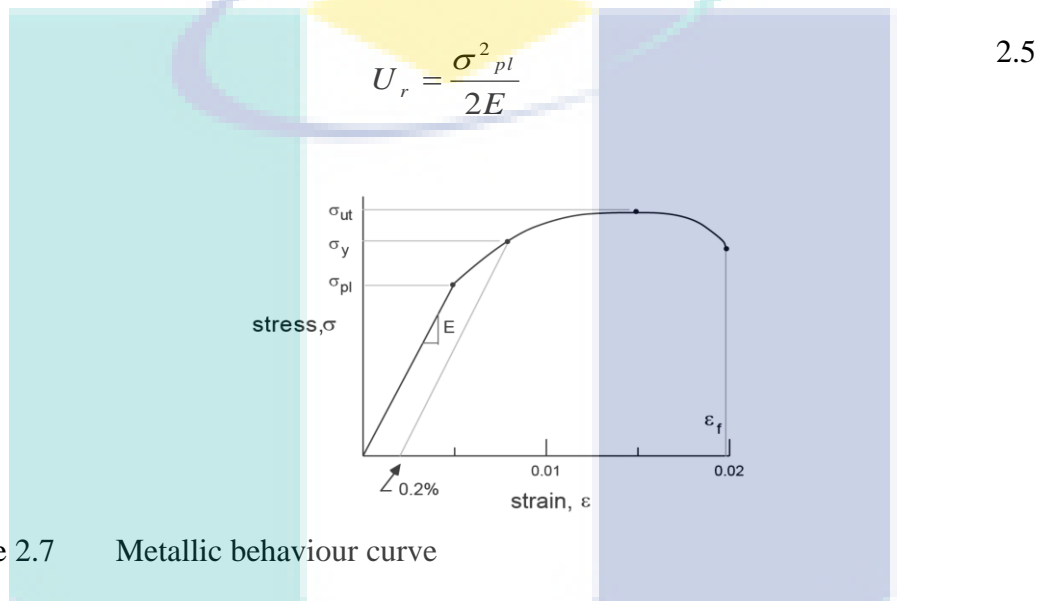


Figure 2.7 Metallic behaviour curve

For CoCr-based alloy with high purity and combined either by powder metallurgy or vacuum melting monitored by annealing and hot working at temperatures about 800-1000°C, the tensile properties obtained are (West, 1982): 0.2% proof stress Tensile strength Elongation 305-345 MNm<sup>-2</sup> 800-875 MNm<sup>-2</sup> 15-30% as seen from Table 2.4. Air-melted materials are much less ductile.

Table 2.4 Tensile properties of the CoCr-based alloy

0.2% proof	Tensile strength	Elongation
305-345 MNm <sup>-2</sup>	800-875 MNm <sup>-2</sup>	15-30 %

Source: West (1982)

### 2.8.2 Chemical properties

In an enormous practice, the CoCr-based alloy is unaffected by various mild corrosive means. Nevertheless, in a finely separated form, it can be much more willingly influenced. The rate of early attack by several media is very reliant on in the form of the

metal and the form of the surface. The corrosion rate of cobalt is established to be of the similar order as that of nickel in various dilute media, but it is much fewer oxidation resistant than nickel above a wide temperature range. Cobalt is energetically corroded by concentrated nitric acid at room temperature but develops passive at lower temperatures. Cobalt is more resistant than a nickel in deaerated dilute hydrochloric acid. Hydrogen is soluble in cobalt to an extent which increases with rising temperature from about 1 weight ppm at 700°C to about 8 weight ppm at the melting point. Oxygen is dissolved to a level of 60 weight ppm at 600°C, rising to 130 ppm at 1200°C but with an inflexion at around 850°C. Nitrogen has been reported as being insoluble in solid cobalt but is soluble to the extent of 40 weight ppm at the melting point (West, 1982).

### **2.8.3 Microstructural analysis**

#### **2.8.3.1 Effect of Carbides in CoCr-based alloys**

The strengthening of CoCr-based alloys is delivered in part by the solid-solution strengthening of the matrix, and in part by precipitation of carbides. The solid-solution strengthening is reliant on the amount of alloying elements not joined as carbides or, in limited cases, as intermetallic compounds, so that the two strengthening mechanisms are to some level interdependent. Solid-solution strengthening is mainly due to the content of chromium, niobium, tungsten and tantalum, while nickel, when existing, marks some influence, but is mainly considered as stabilising the cubic structure and hence escaping instability related with the hexagonal transformation. The second-phase strengthening in cobalt-base is nearly due to carbides or carbonitrides formed by chromium, which is mostly existent to confer corrosion resistance, and other elements added as carbide formers – these may include molybdenum, tungsten, tantalum, niobium, vanadium, titanium and zirconium.

Carbides are mixed carbides in which the metal radical comprises more than one of the elements itemised above, and the forms stated contain MC, M<sub>6</sub>C, M<sub>7</sub>C<sub>3</sub>, M<sub>23</sub>C<sub>6</sub> and occasionally M<sub>2</sub>C<sub>3</sub>. The forms appear in some alloy will influence on the balance of the carbon content, on metallic composition and the thermal history of the alloy. Nitrogen possibly will, in part, substitute for carbon in most of the above carbides (West, 1982). The morphology and location of the carbide precipitate effect the strengthening and, for ideal improvement, precipitation both in grain boundaries and within the grains is

necessary. At the grain boundaries the precipitates avoid gross sliding and migration of the boundaries, and once occur in enough quantities might form a skeletal network which can hold few of the imposed stress. Intergranular precipitation strengthens the matrix by given complications to the movement of dislocations and therefore preventing slip. The distribution of carbides is indomitable in any alloy by the solidification conditions (West, 1982). A representative microstructure of such an alloy is shown in Figure 2.8(a). Additional carbide precipitation, both at grain boundaries and within the grains, occurs on heating to average service temperatures for extended periods. This is shown in Figure 2.8(b) for alloys HS 21 after 24 hours at 870 °C.

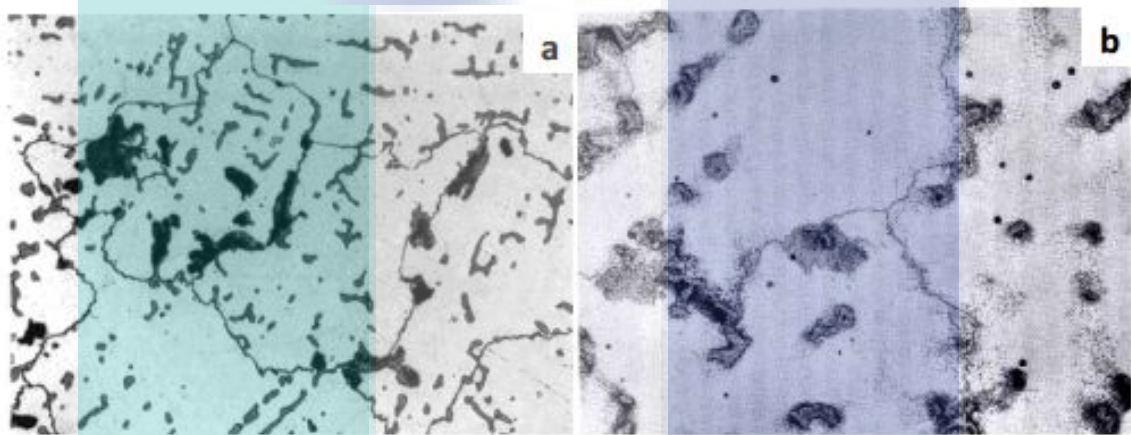


Figure 2.8 Typical as-cast microstructure of HS 21 alloy, original magnification 100x (13) (a) and microstructure of HS after 24 hours at 870 °C, magnification 500x (b)  
Source: West (1982)

Complete solution of the primary carbides is not possible in most CoCr-based alloys as melting would happen before a full solution of the more constant carbides was attained. The microstructure of a typical wrought CoCr-based superalloy in the solution-treated condition displays the occurrence of undissolved primary carbides typically, mainly at the grain boundaries, while after ageing or after a period of high- temperature service additional fine intergranular carbides precipitates are noticeable (West, 1982).

## 2.9 Summary

The usage of CoCrMo alloy is increasing in biomedical application. However, the conventional method like casting and machining are not suitable for small implant size. It also can cause wasteful of material, time-consuming and costly (Hedberg et al., 2014; Henriques et al., 2015; M. OMAR et al.). When compared to other processing methods,

Powder Metallurgy (PM) route which is MIM, offers significant advantages such as the ability to produce near net shape product, more uniform structure and finer grains which will ultimately lead to improvement of mechanical properties of the final product (Ahn et al., 2009; Choi et al., 2015; Marek et al., 2015).

In this chapter, the metallic biomaterials and MIM process are discussed. Due to multiple materials consisting of MIM raw material and the sub-melting point temperature of the moulding process, some extra steps are required to produce the finished compact. Defects that occur during debinding stage are caused by the stresses involved. It's not only gravity and the decreasing amount of binder that makes the compacts vulnerable do defects during debinding. The binder extraction itself causes stress inside the parts. Moreover, the harsh energy-rich atmosphere accommodates for uneven thermal expansion and other problems. In general, the most common defects are cracking and distortion. Therefore, major precaution on the parameter involved should be well build up to support the compacts, and the risk of any defects occurring is reduced.

The sintering process is the last stop in the MIM cycle. Here, compacts get their final strength, and the results are reviled. Since this is the final process, defects introduced during previous processes will show up. Mostly, common sintering defects: cracking, distortion and blisters related to dimensional defects, low density, low properties and large pores. Adjustments to the sintering parameters should fix the problems. If over sintering and too rapid heating, it is much related to grain growth and cause crack formation. Sintering cycle especially; temperature and time play the critical role in this stage. If the cycle of this process goes through high temperatures and too much of the metal enters a liquid phase, the structural integrity of the compact will be lost. This means distortion is very likely. Uneven heating can cause distortion as well. Therefore, finding a suitable sintering cycle will help most strength related defects.

## CHAPTER 3

### METHODOLOGY

#### 3.1 Introduction

This chapter briefly explains the procedures and steps used in this study. This study focuses on the fabrication, experimental research and analysis of compacts by using few steps of the process. The experiment was conducted to determine the effect of sintering temperature and time on the properties CoCr-based alloy fabricated by Metal Injection Moulding (MIM) process. Then, the relationship between the properties and the microstructural analysis were determined. The methodology flow chart of this study is summarised in Figure 3.1. For the current research, three primary objectives are highlighted. The initial process started with the characterisation of powder and binders, feedstock mixing, injection of compacts, solvent and thermal debinding and ended with sintering. The last stage, which is sintering will produce as-sintered compacts where the compacts had undergone sintering process under argon atmosphere in the furnace at selected conditions. Then, the compacts are ready to be tested on the mechanical, physical and chemical study. In the mechanical test, two types of mechanical testing are performed. The test includes a hardness test by Vickers hardness and tensile test, where the compacts are tested until failure to prove their strength. While, for physical testing, three types of testing are conducted. They are dimensional accuracy, shrinkage measurement and density test by Archimedes principles. Then, the microstructures of each compact will be investigated by using an optical microscope (OM) and Selective Electron Microscope (SEM) where the porosity and microstructure behaviour of compacts were studied. The results from a mechanical, physical and chemical test of compacts at each sintering conditions will reflect their morphology of microstructure which proves the relevant and successful results from each property so that the best conditions of compacts will be obtained.



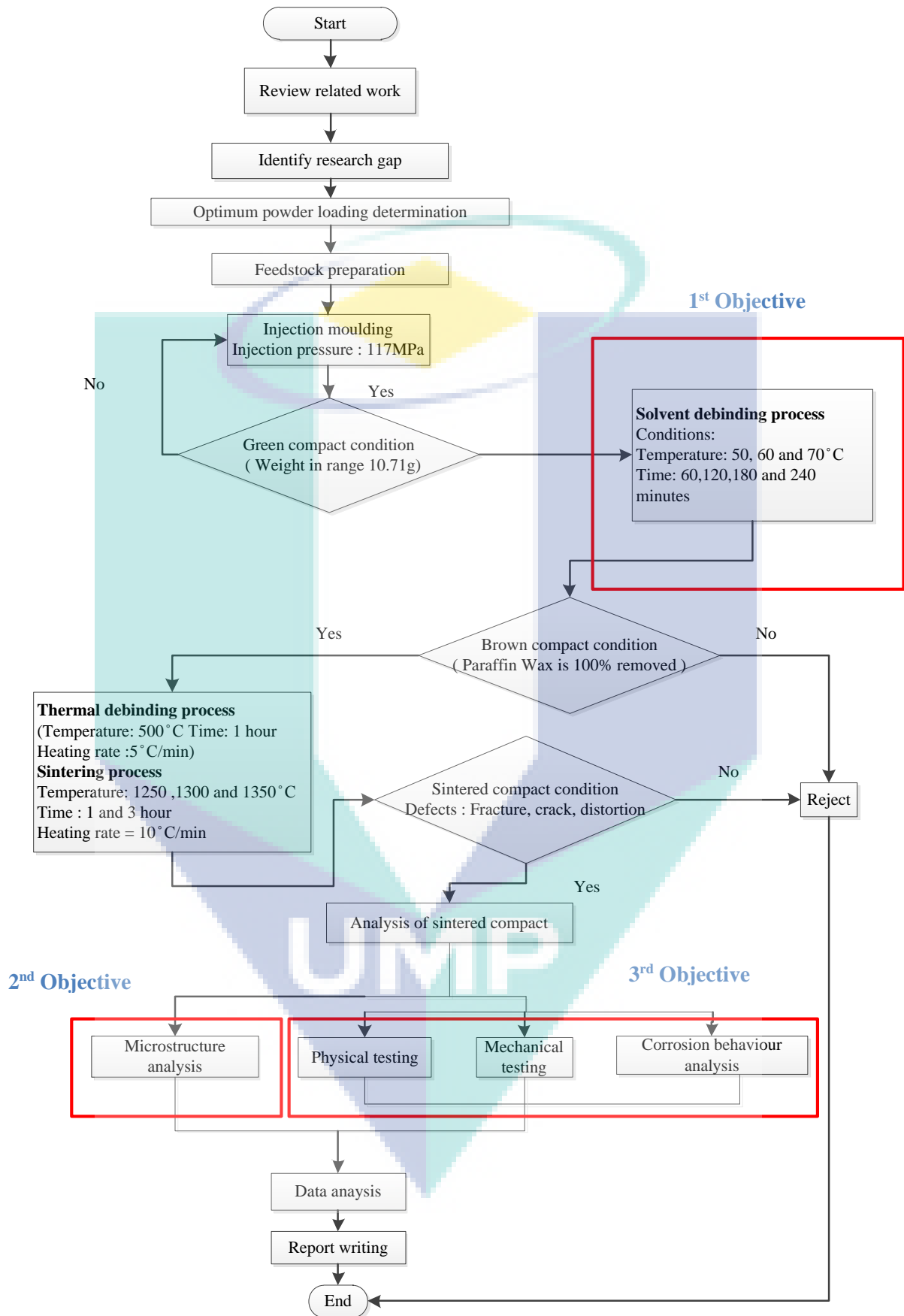


Figure 3.1 Research flow chart

## 3.2 Compact Preparation

### 3.2.1 Characterisation of CoCr-based alloy

The characterisation of alloy powders is an essential part of this study to come out with a good outcome from well understanding of the MIM process at the end of this research. Several difficulties, specifically on the sintered compacts can be overcome with the support by the result from alloyed powder characterisation where their characteristics could be determined and expected. Therefore, the powder must go through powder's characterisation testing concerning on physical and chemical features mainly on the size, shape and packing characteristics before they are being mixed and injected.

#### 3.2.1.1 Metal powder

In this research, the metal powder used was gas-atomised CoCr-based alloy with an average particle size of 22  $\mu\text{m}$ . Powder particles of the CoCr-based alloy are mostly spherical. Figure 3.2 shows that the powder particles of the CoCr-based alloy are generally in a spherical shape. While, from Table 3.1 and Table 3.2 below, the properties of CoCr-based alloy powder and their chemical compositions were detailed.

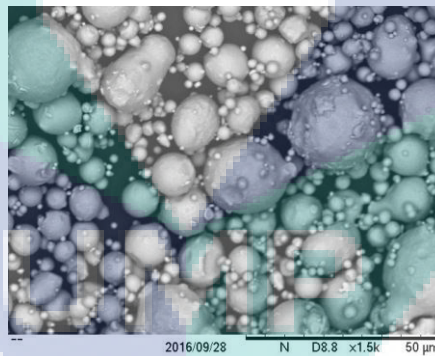


Figure 3.2 Morphology image of the CoCr-based alloy powder

Table 3.1 Properties of CoCr-based alloy powder provided by the manufacturer

<b>Material Properties of the Cobalt-based alloy powder</b>	
Alloy powder	Cobalt-based
Particle shape	Spherical
Particle size $D_{90}$	22 $\mu\text{m}$
Density	8.4 $\text{g}/\text{cm}^3$
Melting point	1454 $^{\circ}\text{C}$



Table 3.2 Chemical composition of CoCr-based alloy powder provided by the manufacturer

The chemical composition of the CoCr-based alloy	
Cr	28.5
Mo	6.00
Ni	0.25
Fe	0.20
C	0.22
Si	0.70
Mn	0.50
W	0.01
P	0.01
S	0.005
N	0.15
Al	0.05
Ti	0.01
Bor	0.006
Co	63.4

### 3.2.1.2 Powder composition and powder size distribution

In this study, the alloy powder used were supplied by Sandvick Technologies, German. The particle size was analysed using MALVERN particle size analyser by using laser scattering particle analyser (Malvern Mastersizer 2000) as shown in Figure 3.3 The morphology of the powders was observed using scanning electron microscope (SEM). Besides that, the powder composition was observed by energy dispersive x-ray (EDX) using SEM with EDX equipment.



Figure 3.3 Laser scattering particle analyzer

### 3.2.1.3 Characterisation of binder's component

In this work, the binder's component used consisted of 70 wt.% paraffin wax, 25 wt.% polypropylene, and 5 wt.% stearic acid. The binder's components itself function as

a temporarily conveyance for homogeneously packing the powder into desired shape. In this study, a 70 wt. % of PW was react as a filler, to fill the gaps among the powder particles besides reduce the viscosity of feedstock. While 25 wt. % of PP acts as a backboned polymer to keep the compact's shape after injection moulding and debinding and 5 wt. % of SA becomes a surfactant to strengthens the adhesion between binder and powder particles. A preliminary study of the binder characteristics was conducted before it proceeds with the MIM method. The melting temperature was determined from DSC analysis where from the analysis, the first peak on the graph will indicate the melting temperature while the second peak showed the decomposition temperature of the binders. The binder's components behaviour is summarised in Table 3.3.

Table 3.3 Characterisation of binders

<b>Binder</b>	<b>Chemical structure</b>	<b>Density (g/cm<sup>3</sup>)</b>	<b>Melting temperature (°C)</b>	<b>Decomposition temperature (°C)</b>
PW	C <sub>31</sub> H <sub>64</sub>	0.91	47-65	200-400
PP	(C <sub>3</sub> H <sub>6</sub> ) <sub>n</sub>	0.90	> 95	328-410
SA	C <sub>18</sub> H <sub>36</sub> O <sub>2</sub>	0.94	69.4	180-380

### 3.3 Characterisation of CoCr- based alloy powders and feedstock

#### 3.3.1 Thermal analysis of the feedstock

Thermal analysis is a method to determine the phase properties of a material using temperature changes method. Thermal analysis is very significant to understand the thermal behaviour of feedstock. The thermal information of the feedstock is necessary to be a guideline during injection, debinding and sintering process. In this project, two types of thermal test which are TGA and DSC analysis were conducted to give information regarding the thermal behaviour of the feedstock in a different aspect.

##### 3.3.1.1 Thermogravimetric analysis (TGA)

Mettler Toledo Thermogravimetric Analysis (TGA) as shown in Figure 3.4 is measuring equipment to define the physical and thermal properties of powders as a function of increasing temperature mainly to determine the degradation temperature of the binder's component. This technique aids to determine the percentage amount of binder being removed after it is heated to the maximum temperature of decomposition rate. The binder's components were evaluated in nitrogen gas with the flow rate of

20L/min. The binder's components were heated from room temperature until it reached the temperature of 600°C with the heating rate of 10°C/min.



Figure 3.4 Thermogravimetric Analysis (TGA) machine

### 3.3.1.2 Differential Scanning Electron analysis (DSC)

A Mettler Toledo differential scanning calorimetry (DSC) model 214 Polyma NETZSCH DSC21400A-01717-L as shown in Figure 3.5 was used to determine the melting point of the binders. The parameters used for DSC was the same with TGA analysis exclude for temperature in which the maximum temperature for the presented DSC machine is 500°C. Each of binder's component was placed into the aluminium crucible and sealed to avoid oxidation from happening. Then, the containing binders were closed tightly with the crucible cap using a particular press purposely made for the DSC test. This process is critical in this study where the suitable temperature for mixing, injection moulding, and solvent debinding can be determined from this analysis.

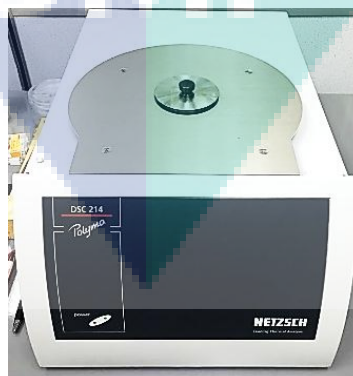


Figure 3.5 Differential Scanning Electron (DSC) machine

### 3.3.1.3 Determination of powder loading

To determine the optimum powder loading, five different powder loading has been recommended which are 64, 65, 66, 67 and 68 vol. % powder loading. All of these parameters were based on previous researchers that are using similar powder size (Manonukul et al., 2010; M. Omar et al., 2003). The formulation feedstock consists of five different powder loading were moulded to a disc shape compact as shown in Figure 3.6. Then, the compact was sintered at 1250, 1300 and 1350°C for one and three hours. The physical and mechanical properties and also the amount of porosity for the five different powder loading sintered compact were analysed under an optical microscope, and the percentage of porosity was measured by using Image J software.

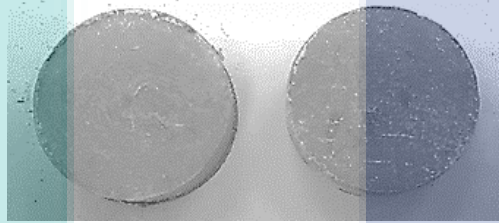


Figure 3.6 Disc shape compacts

## 3.4 The metal injection moulding process

Figure 3.7 below shows the overall process of MIM. In general, there are 4 main steps in this process. Firstly, the powder alloy is adequately mixed with the binder's component to form a homogeneous feedstock, where it called the mixing process. Then, the feedstock was pelletized, to form pellet form feedstock, hence it will easily transport into the injection moulding machine. Second is the injection moulding process, where the feedstock will be moulded into the desired shape which is dog-bone shaped compact or tensile shape where it is termed explicitly as green compact. Then, to remove the primary binder which is Paraffin wax and also stearic acid, the green compact will undergo solvent debinding process at specific required parameters. The compact form after debinding is term as brown compact. Final stages of MIM process, which is sintering will be held in an argon furnace together with the thermal debinding process in specific parameters to form sintered compact. In this study, all compacts were named specifically according to their stage conditions in the MIM process as referred to in Table 3.4.

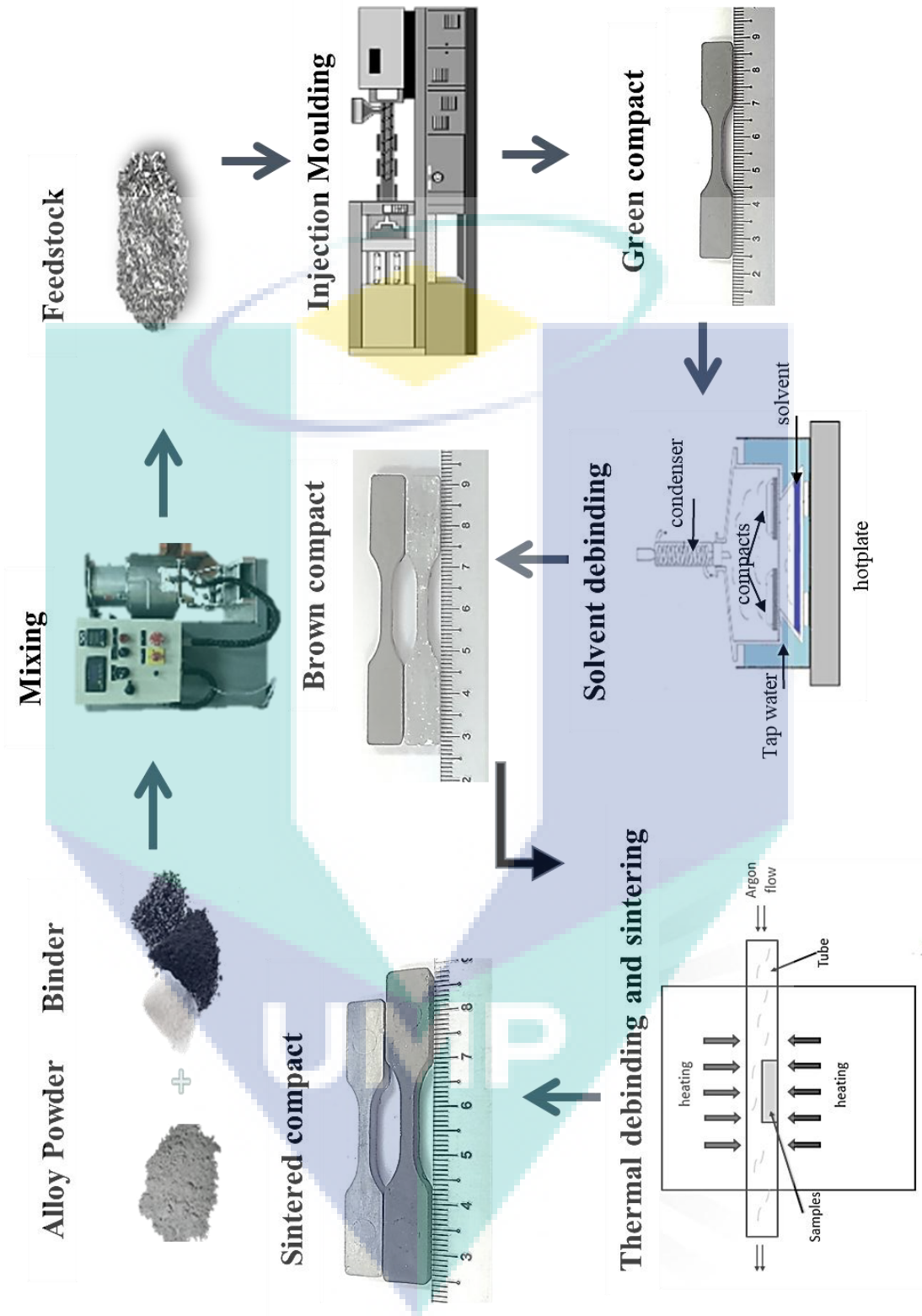


Figure 3.7 Overview of the metal injection moulding process

Table 3.4 Specific labelling for compact's condition for each stage of the MIM process

<b>MIM Stage</b>	<b>Classification of compact</b>
After Injection moulding	Green compact
After Solvent and thermal debinding	Brown compact
After Sintering	Sintered compact

### 3.4.1 Preparation of feedstock

The feedstock for moulding is prepared by mixing a proper ratio of powder and binders. A successful feedstock depends on several parameters. The powder-binder ratio influences the feedstock viscosity. The proper average ratio of the metal powder and binder is 60:40 (Randall M German et al., 1997) by volume, respectively. To prepare the feedstock, the metal powder was mixed with the binder to form a homogeneous paste. In this experiment, the ratio of the metal powder and binder used is 67:33 by volume. The final step in feedstock preparation is to make pellets that are easily transported to the moulding machine. Table 3.5 indicates the powder and binder ratio used in this research, while Table 3.6 shows the estimated weight and volume for the green compact before been moulded. The weight and volume for one green compact were obtained by the calculation of feedstock density based on formula  $\rho = m/V$ . Some of the mixing parameters that could affect the homogeneity of the feedstock are the type of the mixer and mixer blades, the mixing speed and the temperature, the mixing time and the sequence. The binder and powder characteristics will affect homogeneity [10]

Table 3.5 Powder and binder ratio by mass (%)

<b>Properties</b>	<b>The ratio by mass (%)</b>
CoCrMo alloy powder	100
Paraffin Wax	70
Polypropylene	25
Stearic Acid	5

Table 3.6 Estimated weight and volume for a tensile green compact in this study

<b>Injection moulding data for CoCrMo alloy</b>	
The weight of one tensile green compact (g)	10.73
The volume of one tensile green compact (cm <sup>3</sup> )	1.81



### 3.4.2 Mixing process

To create a formulation for binders and metal powder, the double planetary mixer was used to mix the binders and metal powder to produce the feedstock. The mixing process was done at a rotational speed of 70 rpm at 150°C for 90 minutes. Figure 3.8 shows the twin blade mixer machine used in this work.



Figure 3.8 Double Planetary mixer machine

### 3.4.3 Injection moulding

After the feedstock have already been prepared, they will be injected moulded into the desired shape by heating in the moulding machine and injected under pressure into the tool cavity. Standard of ASTM 638-type V for tensile shape was used in this research. The graphics drawing of the tensile shape compact is shown in Figure 3.9. The fabrication of 67 vol. % of a feedstock containing CoCrMo feedstock was carried out on NISSEI 20-tonne injection moulding machine, as shown in Figure 3.10. During this process, two variables which are pressures and temperatures are being optimised to gain the result of green components successfully. Thus, the moulding parameters play an important role in determining the quality of the products.

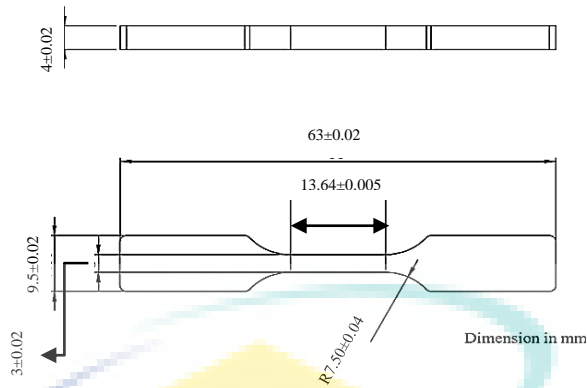


Figure 3.9 Tensile shape model according to ASTM 638-type V standard (unit in mm)



Figure 3.10 NISSEI 20-tonne injection moulding machine components

According to the above image, the injection moulding machine comprises the injection unit, clamp unit, and control unit. The injection and clamping unit are usually arranged in a horizontal position as shown in Figure 3.10. This is the convenient way to fabricate MIM products. The injection unit is mostly a heated barrel with a screw that transporting the molten feedstock to the injection nozzle. Control instruments for pressure and temperature serve to monitor the overall process, and a computer used to controls the operation handling of the machine. The technical parameters of MIM NISSEI NS20 are shown in Table 3.7. While Figure 3.11 below shows the tensile mould used in this current study.

Table 3.7 MIM Processing Parameters in this study

Parameters	Setting
Screw diameter (mm)	19
Injection pressure (MPa)	117 ( ± 200)
Injection speed (cm <sup>3</sup> /s)	25.5
Temperature (°C)	
Injection	150
Mould 1	40
Mould 2	40



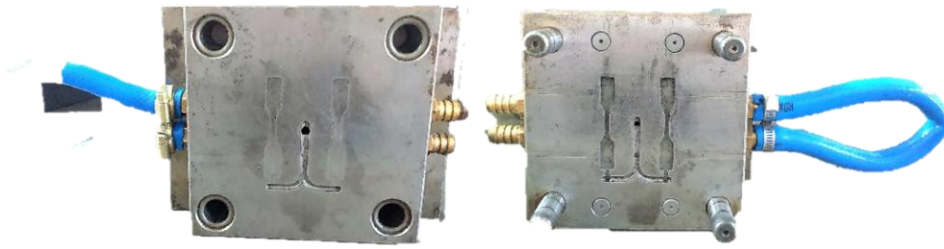


Figure 3.11 Mould used in the current study ( Tensile shape model according to ASTM 638 – type V standard)

#### 3.4.4 Debinding Process

Debinding is a critical problem in MIM because the time for binder removal depends on the section thickness. During this step, the binder is removed from the green compact. In this study, we applied a two-step debinding process. Start from the most popular alternative of debinding which is to immerse the green compact in a solvent and dissolves some binder leaving some polymer behind to hold the particles in place. This process is called solvent debinding. Then, the remaining binder will undergo the second step of the debinding process which is the thermal debinding, where the remaining binder from solvent debinding is slowly heated and decompose by from the green compact.

##### 3.4.4.1 Solvent Debinding Process

Before conducting thermal debinding, solvent debinding process or known as solvent extraction method takes over to remove the primary binder (Paraffin Wax). Before performing the solvent debinding, the green compacts were measured using vernier calliper and analytical balance Precisa Gravimetric to determine the dimensional analysis and weight change after completing the solvent process. Figure 3.12 shows schematic illustrations of solvent debinding process. Here, compacts have been placed in a condenser after been compacted. Then, the compacts were debound at 50, 60 until 70 °C temperatures. The debinding times were set from 60 to 240 minutes (4 hours). From Figure 3.13, the illustrations of the graph for solvent debinding process been utilised. About 40 ml n-heptane was used as a solvent in this debinding process by wicking technique using  $\text{Al}_2\text{O}_3$  (alumina) powders. This powder bed helps to avoid distortion, and it offers more uniform heating through this process (Randall M German et al., 1997). Then, as the brown compacts were obtained from this process, the amount of weight loss for each compact for each condition as stated will be measured. Before the weight of each compact was measured, the compacts were dried in a vacuum desiccator for half an hour.

From Equation 3.1 below,  $M_{pw}$  indicates the mass loss of paraffin wax where the mass of PW and SA were calculated based on the equation below:

$$M_{pw}(\%) = \frac{M_b - M_a}{M_b} \times 100 \quad 3.1$$

Where  $M_b$  is the mass before solvent debinding (green compact) and  $M_a$  is the mass after solvent debinding of the (brown compact).

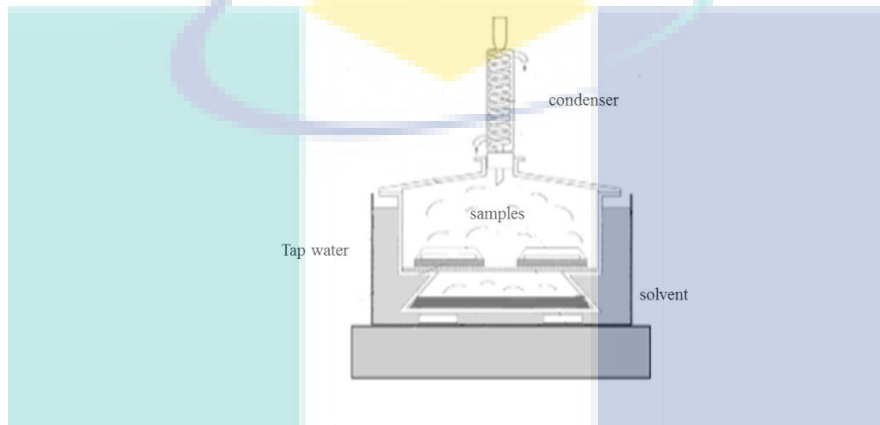


Figure 3.12 Schematic diagram for solvent debinding by wicking technique

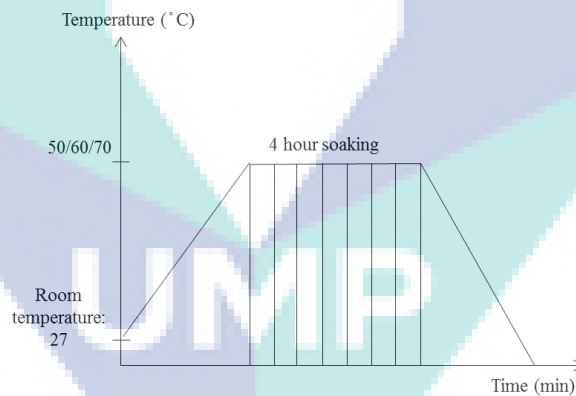


Figure 3.13 Graph illustrates Time vs Temperature plot of solvent debinding

### 3.5 Thermal debinding and sintering process

The thermal debinding process is an important technique to remove the secondary binder. In this study, secondary binder known as polypropylene (PP) was removed at 500° C for 1 hours soaking time to ensure that there is no remaining binder in the brown compacts. The compacts were heated in a tube furnace with high purity argon gas flow starting from room temperature 27 to 500°C with the heating rate of 5°C/min for 1 hour

soaking time. The flow rate of binders within the compacts to the surface is rapid at the beginning of this process and can be controlled by the binder's degradation rate. When the polymer degradation starts, the pores will open near the surface of the brown compact which aids the removal of burnout gasses of the binder. After debinding, the compacts continued to be sintered in a furnace.

Sintering is a continuous process from thermal debinding. The compacts have also been sintered under high purity argon gas in a tube furnace. There are six different conditions used; 1250, 1300, 1350°C for sintering time at 1 and 3 hours with the 10°C/min heating rate. These sintering temperatures were selected based on the composition of material which usually lies within 70-90% its melting temperature (Banerjee et al., 2012; M Rafi Raza et al., 2012). For the holding time during the sintering process, it also may be varied in a range between 90-180 min (Limberg et al., 2012). It is then followed by furnace-cooled at until reached the room temperature. Figure 3.14 shows the process steps for thermal debinding and sintering from brown compact and Figure 3.15 referring to the graph pattern for both processes. After the sintering process, all sintered compacts were named according to prototype labelling as referred to in Table 3.8 based on different sintering temperature and sintering time used.

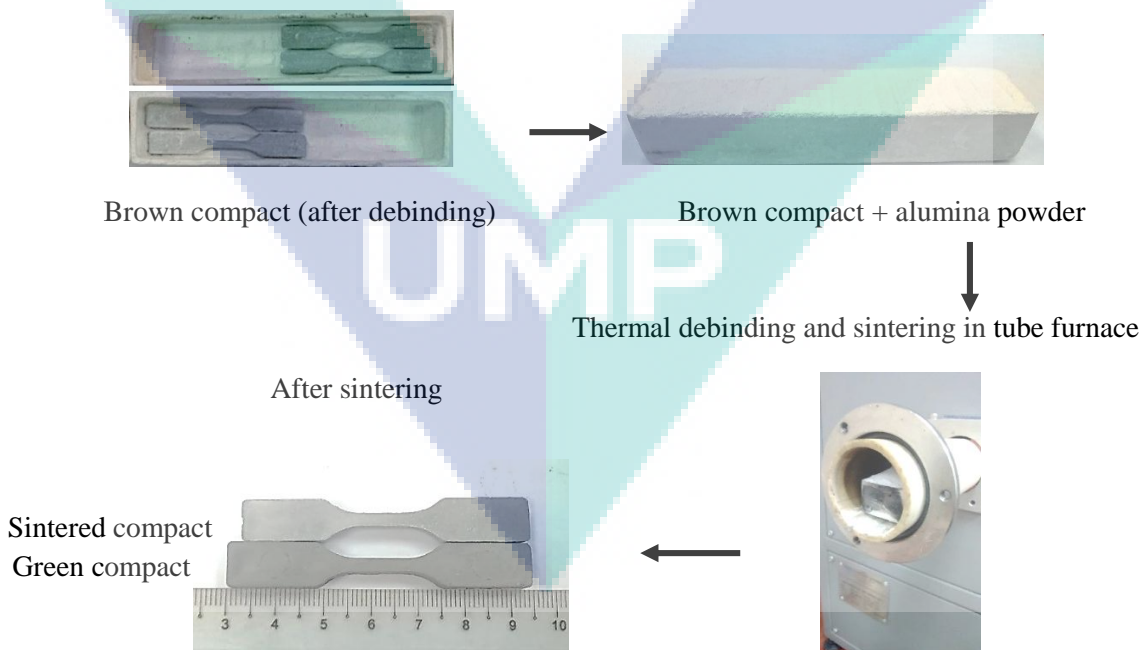


Figure 3.14 Steps for thermal debinding and sintering process

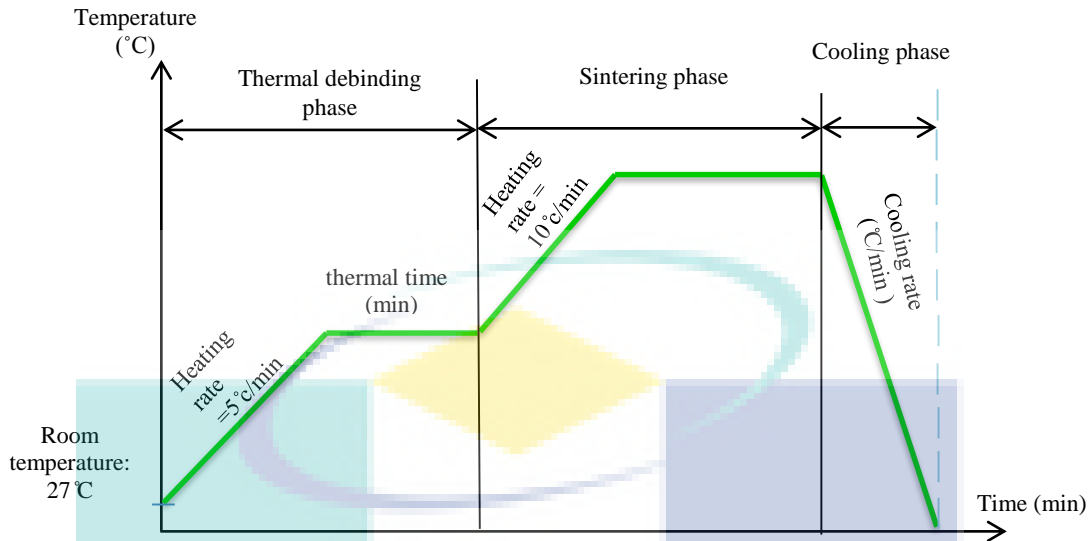


Figure 3.15 Graph pattern of thermal debinding and sintering process

Table 3.8 Prototype labelling for the sintered compact

Sintering conditions	Compact labelling
1250°C sintering temperature for 1 hour soaking time	1250°C-1h
1300°C sintering temperature for 1 hour soaking time	1300°C-1h
1350°C sintering temperature for 1 hour soaking time	1350°C-1h
1250°C sintering temperature for 3 hour soaking time	1250°C-3h
1300°C sintering temperature for 3 hour soaking time	1300°C-3h
1350°C sintering temperature for 3 hour soaking time	1350°C-3h

### 3.6 Characterisation of the compacts

#### 3.6.1 Physical testing

##### 3.6.1.1 Dimensional accuracy analysis

In dimensional accuracy analysis, the green compacts dimension ( $D_{Gc}$ ), after injection moulding process and the nominal mould dimension ( $D_{Nm}$ ) as stated in Figure 3.9, will be measured and compare. First of all, the compacts were measured using a vernier calliper to determine the dimensional changes regarding length, thickness and width of the compacts. The vernier calliper is being used as it is a precise instrument to measure internal and external distances of the compacts accurately. The formula to calculate the dimensional accuracy is shown below. While the dimension of the green compact was measured from its length ( $D_{Gc1}$ ), thickness ( $D_{Gc2}$ ), width ( $D_{Gc3}$ ) is shown in Figure 3.16.

The formula to calculate the percentage of dimensional accuracy, D (%) is shown in Equation 3.2 below:

$$D\% = \frac{|D_{Nm(1,2,3)} - D_{Gc(1,2,3)}|}{D_{Nm(1,2,3)}} \times 100 \quad 3.2$$

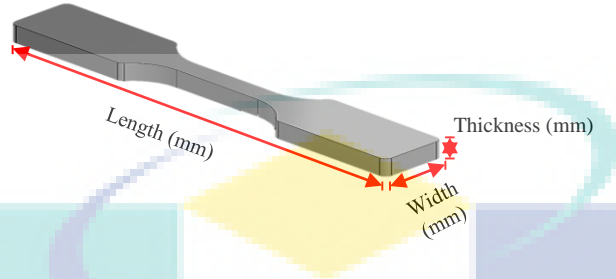


Figure 3.16 Schematic diagram of MIM CoCrMo tensile bar

### 3.6.1.2 Shrinkage measurement

Theoretically, after sintering process, there will be some physical modifications on the compacts, especially on the physical appearance as the compacts might shrink or expand due to diffusion and bonding occur between particles of metal powder. The weight changes between green compacts ( $W_{Gc}$ ) and sintered compacts ( $W_{Sc}$ ) will be measured by using analytical balance Precisa Gravimetric equipment and compared. In this research, the shrinkage result was obtained using at least three compacts of CoCrMo alloy for each sintering condition. Then, an average measurement of these compacts was obtained. The calculation of the percentage of shrinkage, S (%) is shown in the Equation 3.3.

The formula to calculate shrinkage:

$$\% \text{ shrinkage} = \frac{|W_{Gc} - W_{Sc}|}{W_{Gc}} \times 100 \quad 3.3$$

### 3.6.1.3 Relative density measurement

Density was measured by Archimedes' method, according to standard ASTM B 328-96. The sintered compact's weight was measured in air and by immersing in water. Archimedes principle had stated that the weight of the displaced fluid by the immersed object is directly proportional to the volume of the displaced fluid as shown in Equation 3.4. Method for measuring the compacts by this Archimedes technique is illustrated in

Figure 3.17. Measurements were carried out with a precision balance (Precisa Gravimetric) with a sensibility of 0.0001 g as shown in Figure 3.18.

$$\rho = \frac{W_{air}}{W_{water}} \times (\rho_o - d_{air}) + d_{water} \quad 3.4$$

$\rho$  = Relative density of compact (%)

$W_{in\ air}$  = Weight of compact in air

$W_{in\ water}$  = Weight of compact in water

$\rho_o$  = Density of CoCrMo alloy; 8.4 g/cm<sup>3</sup>

$d_{air}$  = Density of air ; 0.001g/cm<sup>3</sup>

$d_{water}$  = Density of water;(1.0017- 0.0002315)( Temperature of water)

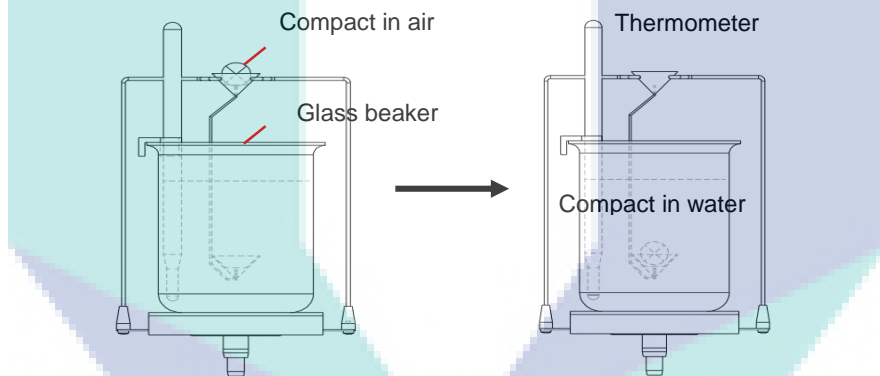


Figure 3.17 Method of measuring relative density

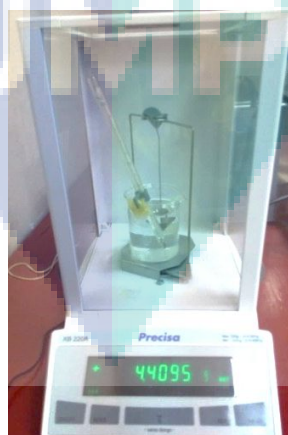


Figure 3.18 Precisa Gravimetric Equipment

### 3.6.2 Mechanical testing

#### 3.6.2.1 Tensile test

The tensile testing was conducted to estimate the strength of the sintered compact of CoCrMo alloy compact. The testing involves pulling the compact to failure in a period at a constant rate. The capability of the compact to resist breaking under tensile stress is one of the significant methods to measure the mechanical properties of the material used in structural applications. Meanwhile, Figure 3.19 shows an Instron tensile machine testing used in this study. The technical parameters of the tensile machine are shown in Table 3.4.

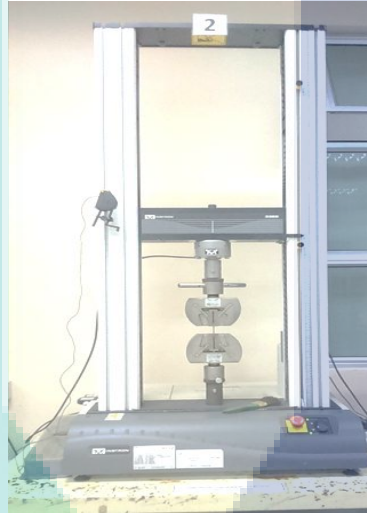


Figure 3.19 INSTRON Universal Testing Machine

Table 3.9 Setting parameters for Universal tensile testing machine

Parameters	Setting
Crosshead speed	1 mm/min
Temperature	25 °C
Humidity	55%
Standard	ASTM E8

#### 3.6.2.2 Hardness testing

The mounted compact was shown in Figure 3.20. Vickers hardness machine types MMT X7 was used in testing the hardness of mounted compact of the CoCr-based alloy as shown in Figure 3.21. An optical measurement system founded the Vickers technique. It was used to measure the hardness of materials were testing its capability to resists plastic deformation by penetration. This technique practices the principle of penetration by indenting the specimen with the diamond indenter. The diamond typically was in the



form of pyramids shape with the square base and having an angle of 136 degrees between opposite faces. The specimen subjected to load 1000 gf. The time taken for each indentation was 15 seconds.



Figure 3.20 Mounted compact



Figure 3.21 Vickers Hardness Machine MATSUZAWA Type MMT X7

### 3.6.3 Microstructural analysis of compacts

#### 3.6.3.1 Microstructure analysis by an optical microscope (OM) and selective electron microscope (SEM)

Sintered compact was examined by optical microscope brand OLYMPUS model BXF60F – 3, to capture the image at different magnifications while SEM function is to determine the compact's surface topography, fracture surface after tensile test and the composition. Besides that, SEM is also capable of observing the formation of an elemental component such as carbide formation that occurred after the sintering process using EDX analysis. The necessary steps such as mounting, grinding, polishing, and etching were done to obtain the desired results.

### 3.6.3.2 Porosity and grain size analysis of compacts by Image-J software

Amount of porosity of sintered compacts was determined by using Image-J analysis. The analysis was done by measuring few cross-sectional areas on the surface of compacts using the software. Then, the number of pores were measured based on the percentage of the area obtained. The data was tabulated employing three different compacts measured. The same theories method was applied for measuring the grain size by using Image-J software analysis which is by calculating the percentage area on the surface of three different compacts. Figure 3.22 shows the steps to measure the amount of porosity by ImageJ software analysis:

1. First, the file being analysed was opened. Zoom in on the scale bar, and the image was calibrated. Straight line was drawn on the scale bar and the angle was checked to make sure it was absolutely zero.
2. Under Analysis, set scale was opened, and here the known length were set based on scale and units were set for microns.
3. Next, the image were set under Image for Type to 32-bit gray scale.
4. Then, Threshold under Image was selected. The thresholding was adjusted to avoid measuring the scale bar.
5. Under Analyse, set measurement was opened, then Area and Area Fraction were selected to measure the percentage of area.
6. Under analyse particle, the size limits were set at 2-infinity and cumulative was set for 0.50-1.00.
7. The outlines of particles with white and black background examined were shown. Here, the difference between micrograph before measurements were compared to shows the differences.
8. Lastly, the summary results of the particles were obtained and analysed. For further analysis, this step were repeated by using three different image with same area to measure the means of particle size distribution for each sintering conditions. The steps were repeated from the beginning.

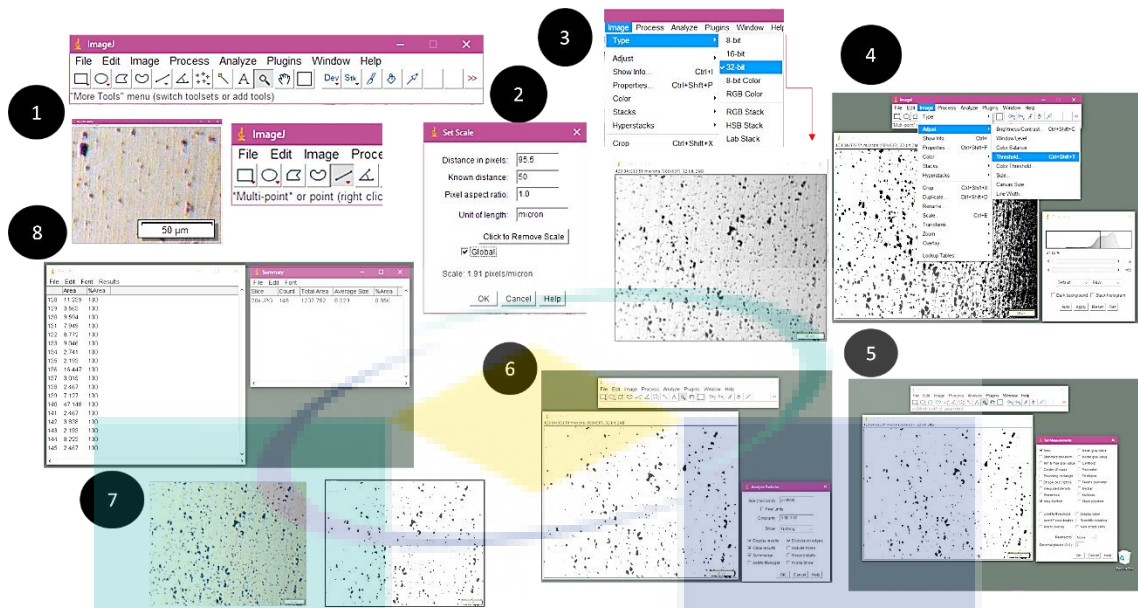


Figure 3.22 Steps to measure amount of porosity by Image J Software analysis

### 3.6.3.3 Hot mounting

Mounting has required the process to offer a right method to hold the compacts, as, after sectioning, the compacts will become smaller and thinner, making it difficult to hold for the next process which is grinding and polishing. Mounting is divided into two types which are hot and cold mounting. In this study, hot mounting was used as hot mounting usually quicker and more economical. While cold mounting is used for specimens that may be damaged by heat or pressure. Hot mounting compacts were as shown in Figure 3.23.



Figure 3.23 Hot mounting of CoCrMo alloy sintered compact

### 3.6.3.4 Grinding and polishing

After mounting, the grinding process was completed. In this phase, the compacts were grounded using rough and fine grinding. The objective of rough grinding is to eliminate flaws on the surface of compacts while fine grinding was used to make the

compacts shining and smooth. Dissimilar grits of abrasive papers were used for this process which is 180, 240, 400, 600 and 1200. Throughout grinding, water is used as a lubricant to avoid deep scratch besides keeping the quality of the compact 'surface. The surface of the compacts was manually ground.

After the grinding process has been done, the process was continued to the polishing process. This process determines to get the mirror surface of the ground compacts surface. To preserve the quality of the compact surface, both of these processes were carried out at the same time for both compacts. For the polishing process, several steps that are compulsory to be followed to get the mirror surface. The solution used for polishing cloths were 3 micron Diamond Compound microid extender, Siamat Non-crystalline (Colloidal Silica) and distilled water. The rotation speed of 230 rev/min was used for this process. The grinding and polishing machine was shown in Figure 3.24. All solution were shown in Figure 3.25. After the polishing process, the compacts were cleaned using distilled water to prevent contamination.



Figure 3.24 Metkon grinding and polishing machine



Figure 3.25 Polishing solutions after the grinding process

### 3.6.3.5 Etching process

Etching is the process of using chemical, mostly a combination of acid and distilled water to reveal the grain and grain boundaries of the compacts. In this study, three types of acid were used which are Acetic Acid ( $\text{CH}_3\text{COOH}$ ), Nitric Acid ( $\text{HNO}_3$ )

and Hydrochloric Acid (HCl) and distilled water. Figure 3.26 shows the etching solution for CoCrMo alloy. Firstly, the etchant solution must be well prepared with correct measurement for each chemical as shown in Table 3.10 below. While Figure 3.27 shows the yellowish etchant solution that is ready to be used for this process. After the solution is ready, by using a dropper, drop the etchant solution on the surface of the compact. Then, left it for 30 until 40 seconds. Lastly, dried the compact's surface by using a dryer before the compacts were observed using an optical microscope to analyse the porosity and grain boundaries of the compacts.

Table 3.10 Chemical used for the etching process

Chemicals	Soaking time	Atmosphere
Distilled water Acetic Acid Nitric Acid Hydrochloric Acid	30 – 40 seconds	Room temperature

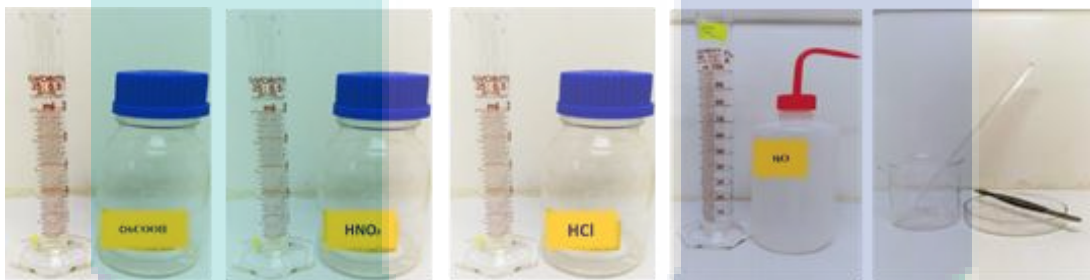


Figure 3.26 Solutions and tools used for etching



Figure 3.27 Yellowish white solution ready to use for etching

### 3.6.4 Corrosion behaviour study

For the corrosion behaviour study, electrochemical tests were performed in a standard three-electrode glass cell using a potentiostat Intelligence Control Bank WPG100e with an interface for computer controlled data acquisition. The tensile shaped compacts were ground with grade 2000 emery paper, and copper wire was fixed at the back side for electrical contact. The compact was isolated by an acrylic painting; back

side and lateral sides as shown in Figure 3.28. The front side, exposed to the electrolyte, had an area of  $0.51 \text{ cm}^2$ . Potentiodynamic tests were performed in the Ringer solution comprised of (8.6 g/L NaCl, 0.48 g/L  $\text{CaCl}_2$ , 200ml  $\text{H}_2\text{O}$ , 0.3 g/L KCl). The solution was kept at  $37^\circ\text{C}$  by a thermostat with 7.2-7.3 pH value. Voltage scans were started at a potential of  $-100 \text{ mV}$  vs standard hydrogen electrode (NHE). The scan direction was inverted when the anodic current density surpassed  $10 \text{ mA/cm}^2$ . The scan rate was  $0.4 \text{ mV/s}$ . The setup diagram for the process is shown in Figure 3.29. The counter electrode was made of platinum wire. Standard three electrodes cells were used as a working cell, with a Pt net as a counter electrode, a saturated calomel electrode (SCE) as a reference electrode and CoCrMo alloy compact as the working electrode.



Figure 3.28 Painted sintered compact by acrylic painting

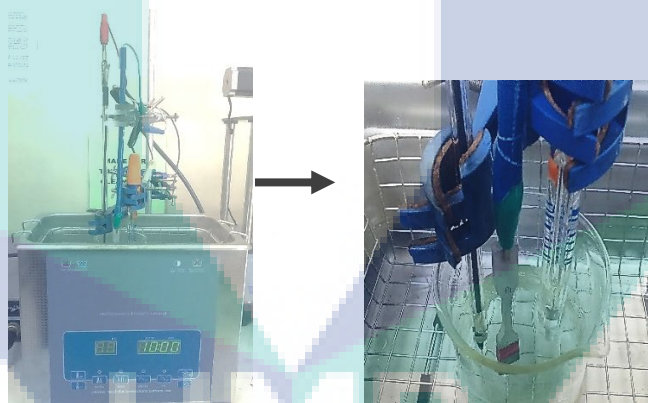


Figure 3.29 Set up a diagram for electrochemical testing

### 3.1 Summary

The methodology for this work was briefly explained in this chapter. The sequence of the methodology followed the research flowchart. All the material and facilities involved in this research were presented in pictures, and the procedure to use the facilities were explained detailed.



## CHAPTER 4

### RESULTS AND DISCUSSION

#### 4.1 Introduction

This chapter describes the results related to the CoCrMo alloy compacts. The results are presented in graphs, figures and tables to clarify the findings. The discussion is based on the previous research which is related to the fabrication of CoCrMo alloy compacts starting from powder until the final sintered compacts analysis. This chapter is divided into six main sub-chapters which are results and discussions on the characterisation of materials used, solvent debinding, physical properties, mechanical properties, microstructural analysis and corrosion behaviour. Each sub-chapter is explained in details about what are the outcomes of this study.

#### 4.2 Characterisation of metal powder

##### 4.2.1 Particle size distribution of CoCr-based alloy powder

Figure 4.1 shows a particle size distribution curve of the metal powder. Three distribution of particle size which is  $D_{10}$ ,  $D_{50}$  and  $D_{90}$  are shown in Table 4.1. This analysis was obtained by Particle size distribution analysis test. Another measurement of the particle size study is the distribution slope parameter,  $S_w$ . The  $S_w$  value of the metal powder has been calculated by using the following formula from Equation 4.1:

$$S_w = \frac{2.56}{\log\left(\frac{D_{90}}{D_{10}}\right)} \quad 4.1$$



From Table 4.1, the  $S_w$  value for the consumed powder was documented at 3.3. It can be determined that the powder illustrate a broad particle size distribution and it is suitable to be mould. The distribution slope  $S_w$  and mean particle size,  $D_{50}$  shows necessary measures of a powder. The parameter  $S_w$  which is identical to a standard deviation or coefficient of variation is the slope of the log-normal cumulative distribution. Narrow particle size distributions are agreed to the huge value of  $S_w$ , and wide distributions resemble small values of  $S_w$ . The most suitable and easiest powders to mould present  $S_w$  values of around 2 where the powder were broad distributions, while if the  $S_w$  values were between 4 to 5, the powder is more difficult to be mould (Sotomayor et al., 2010a).

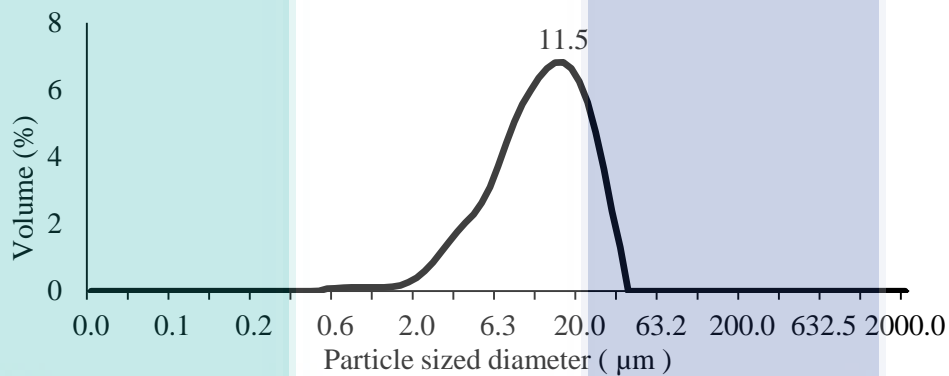


Figure 4.1 Particle Size Distribution Curve

Table 4.1 Characteristics of metal powder

Powder	Size distribution	$D_{50}$ ( $\mu\text{m}$ )	$D_{90}$	$D_{10}$	$S_w$
CoCrMo	22	11.5	23.7	4.1	3.3

#### 4.2.2 Selection of optimum powder loading

Figure 4.2 shows the optical micrograph for a sintered compact from five difference powder loading which is 64, 65, 66, 67 and 68 % volume powder loading. It can be understood that 67 vol. % powder loading indicates the lowest percentage amount of porosity compared to 64, 65, 66 and 68 vol. %. As shown in Figure 4.3 only 0.08 % porosity were recorded on 67 vol.% sintered compact where 16.3, 3.64, 0.83 and 0.51 % were recorded on 64, 65, 66 and 68 vol.% sintered compact. A higher percentage of porosity on 64 vol. % sintered compact perhaps caused by a high amount of binder's excess. The compact that has low powder loading will experience difficulty in densification due to a higher percentage of pores among the metal particle need to be

filled by a metal atom during the sintering process. Furthermore, a low amount of binders also can form a high percentage of porosity on the surface of the sintered compact. When the binder concentration is low, a critical composition is faced beyond which the viscosity is very high, and voids form in the mixture. Though, a higher amount of powder might lead to the inadequate amount of binder's component which makes it difficult to inhibit voids. Moreover, it also leads to challenge and difficulty in moulding and causes a higher amount of porosity after the sintering process (Randall M German, 1990). From this work, 67 vol. % PL obtained the lowest percent of porosity, and it can consider as appropriate powder loading for this feedstock. The low percentage of porosity at 67% vol. % powder loading will enhance densification and also its properties. The selection of this powder loading is also supported with study conducted by (Wahi et al., 2016), in this study, the feedstock for moulding is prepared by mixing a suitable ratio of powder and binder which is 67%. It is found that the mixture is homogeneous, free of agglomeration and contains no porosity. The powder were added in stages and the homogeneity of the mixture was found experimentally better.

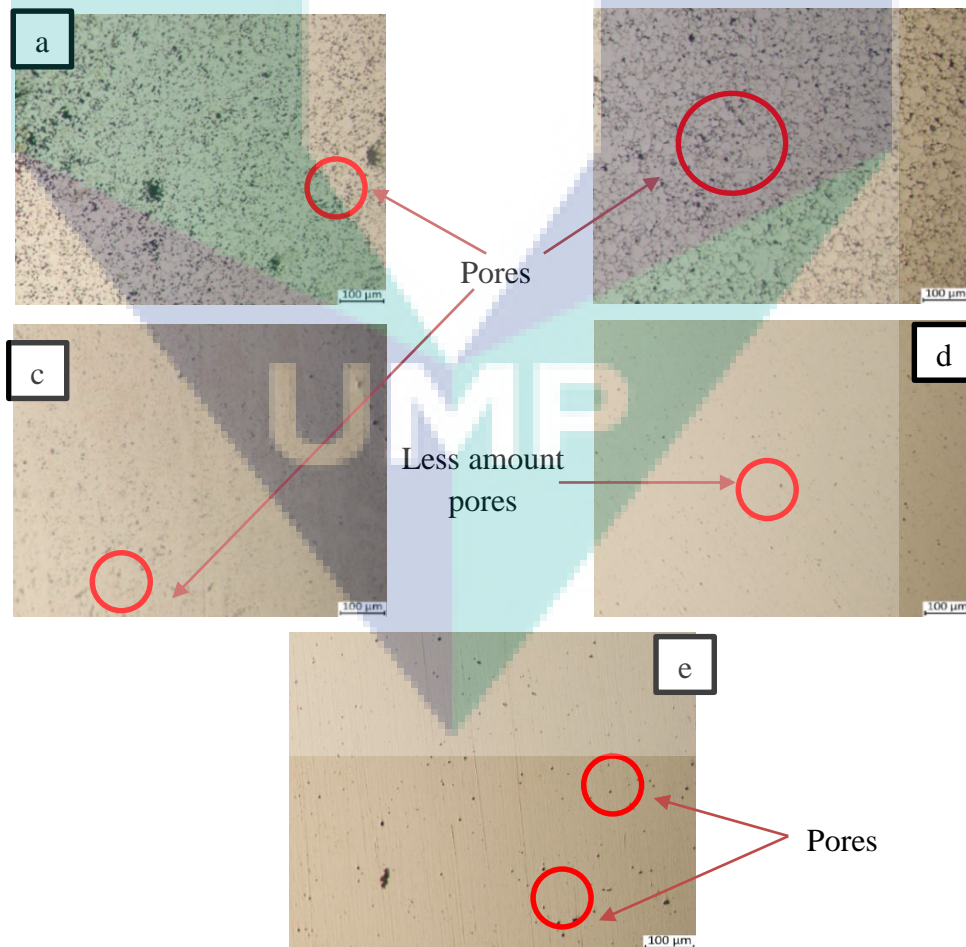


Figure 4.2 Optical micrograph of sintered compact ; a) 64 vol.% PL b) 65 vol.% PL c) 66 vol.% PL d) 67 vol.% PL e) 68 vol.% PL

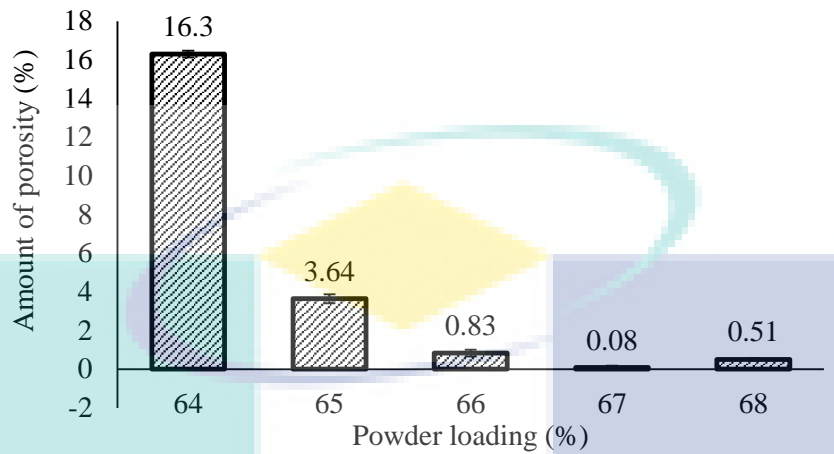


Figure 4.3 Percentage of porosity for five different powder loading

### 4.3 Feedstock characterisation

Means of thermal characterised the feedstock and flowed analysis to get certain insights on the thermal event and fluidity of the feedstock prepared as discussed on the following sub-topic. Furthermore, the injection moulding and solvent debinding temperatures were also expected by thermal properties of feedstock as it suggests an excellent guide for a future experiment in this research.

#### 4.3.1 DSC measurement of binder's component and feedstock

The objective of this process is to determine the binder's melting point and to measure the maximum temperature to obliterate all the binder's component. Figure 4.4 (a) and 4.4 (b) show the DSC analysis of binders and feedstock. From Figure 4.4 (a), it can be observed that temperature at 57.5 – 167.5°C is the uttermost feedstock's melting temperatures. As shown in the figure, the first peak of the curve shows the melting point of paraffin wax and stearic acid. While, for polypropylene, the highest peak, which is the second peak specified the melting of polypropylene. From Hwang et al. (Hwang et al., 1997) it was stated that, when the melting point of the maximum melting binder component is surpassed, the binder becomes more flowable.

Whereas, from Figure 4.4(b), the peak on the graph indicates the melting temperature of the feedstock at 420.5°C. At this temperature, the feedstock will wholly

decompose. All binder's components were apparently burned off entirely at the temperature of 500°C for the thermal debinding process. From M.H.I. Ibrahim, it stated that from analysis from TGA measurement propose that, the decomposition of feedstock will not occur during the mixing process (M. H. I. Ibrahim et al., 2016).

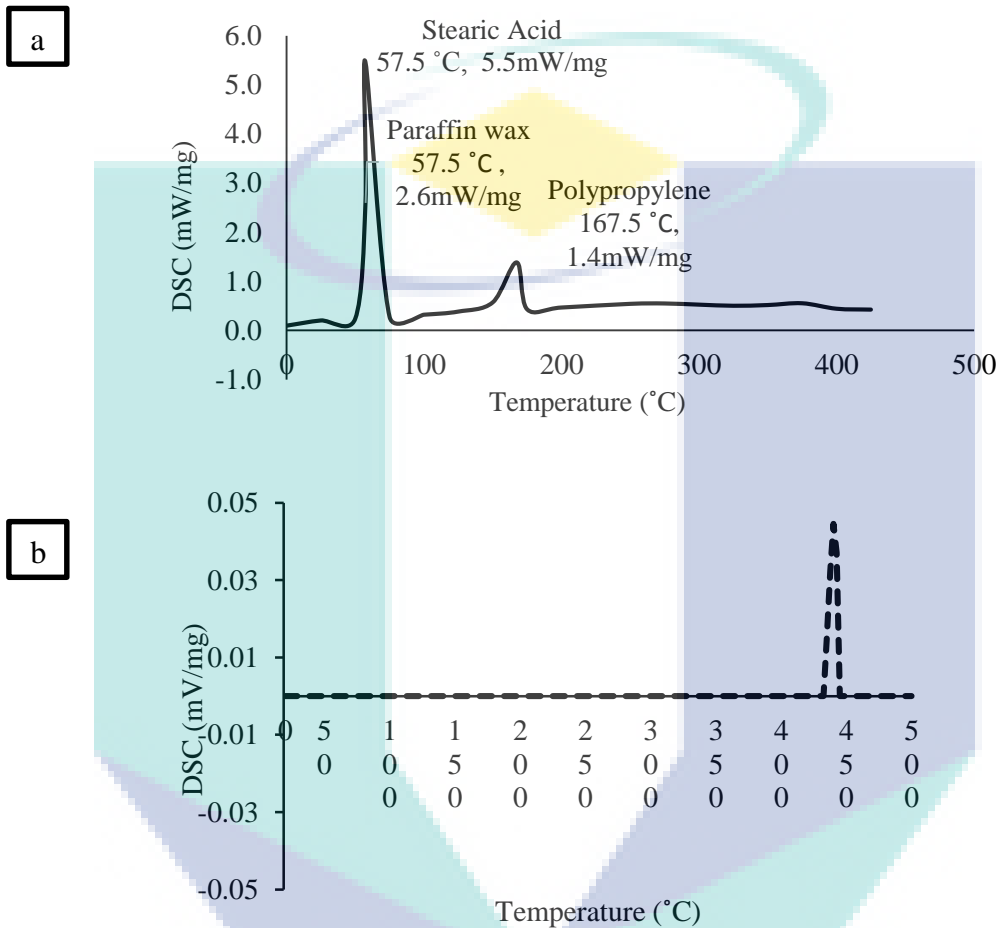


Figure 4.4 DSC of binder's component (a) and DSC measurements of feedstocks (b)

### 4.3.2 TGA analysis of binder's component and feedstock

Thermal properties of the binders and feedstock from TGA analysis are shown in Figure 4.5(a) and 4.5(b). Throughout the mixing and injection process, the temperature used should be lower than be the decomposition temperature of the binder components to prevent the binder loss. As seen in Figure 4.5(a), the decomposition temperature for the binder was started at 180°C which indicates the degradation temperature for stearic acid and paraffin wax. It can be concluded that the decomposition of binders has not occurred in the mixing and injection process as the temperature was set at 150°C for both processes. For polypropylene, the degradation occurred at 325°C and is entirely decomposed at the

temperature of 475°C. Polypropylene has usually been removed from the compacts in a thermal debinding process. Thus the thermal debinding temperature was set at 500°C to ensure all the binders were removed.

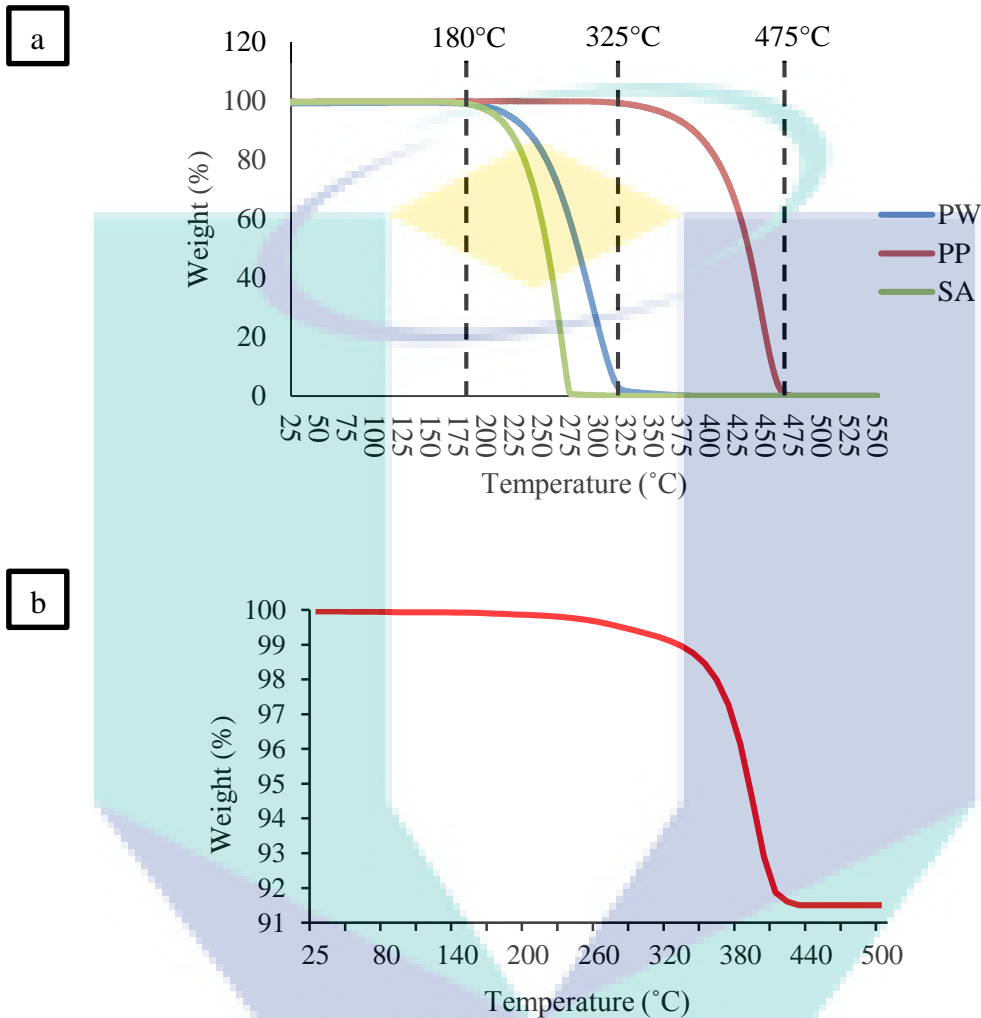


Figure 4.5 TGA of binder's component (a) and TGA measurements of feedstocks (b)

#### 4.4 Injection moulding

After the injection moulding process, the compacts formed were named as green compacts as shown in Figure 4.6 below. In this research, a tensile shape mould was used referring to ASTM 638-V standard. The dimension of the compact was previously detailed in chapter three at Figure 3.9. The injection moulding process was completed using NISSEI NS-20A injection moulding machine. The injection temperature was chosen higher than the melting temperature of the primary binders, PW (58°C) initial degradation temperature of PW which is 180°C and lower than its degradation

temperature which is 180°C. Previously, the moulding temperature was set at 140 °C. The cavity was not fully occupied by the feedstock. This circumstance can be called as short shot (occurs when the flow of molten material doesn't completely fill the cavities in a mould) and presented in Figure 4.7(a). For the next trial, the moulding temperature was increased to 160°C. Unfortunately, a defect had also appeared on the green compact. This time, the green compact shows a sink mark and fracture defects as shown in Figure 4.7 (b) sink mark and fracture Figure 4.7 (c). These defects might be due to the higher moulding temperature used. Thus, the temperature was set between 160 and 140°C which was 150 °C and a desirable final moulded compact without any defects was physically observed, besides the compact also has a suitable weight when compared with the estimation weight of one green compact as shown in Figure 4.6 previously.

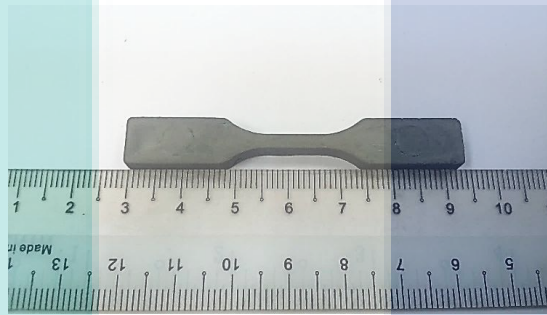


Figure 4.6 Green compact of CoCr-based alloy

During the injection moulding process, a few compacts had been rejected. It was determined when the compact's weights are measure below than the theoretical weight of the compact. This inadequacy was assumed to occur, due to the formation of pores within the compacts. The mass of green compact will then be compared with the mean weight for one tensile compact from a particular calculation which is 10.72 g. The green compact that has about the same or higher mass achieved than theoretical weight can be considered as good moulded compact. Normally, the higher mass were achieved due to an excess material had occupied the entire mould and suitable parameters for injection machine was selected. Hence, higher weight of one compact will be obtained compared to estimation weight of the compact. While green compacts will be rejected when their weights are below than theoretical weight which means the presence of pores occurs. The weight of the compact was weighed, to maintain a good conditions of the compact before the stage of debinding and sintering. At this phase, a compact still in medium fragile, density was not been measure yet, do to unsuitable condition of compact to be measure



by Archimedes' principle, or in other words, it may disturb the strength and compact might cracks during the testing. Therefore, by measuring the weight of each compacts and compare with the estimation weight is a suitable way to get a good green compact for the next phases in MIM

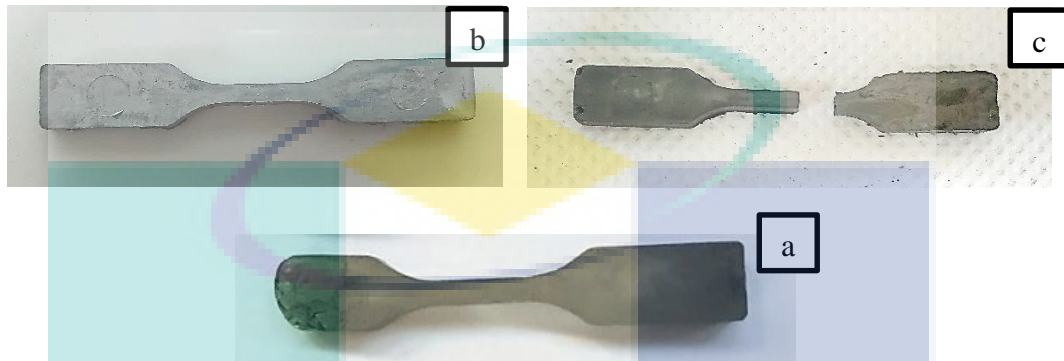


Figure 4.7 Defect (a) Short shot (b) Sink mark (c) Fracture

#### 4.5 Solvent debinding

The extraction of the binder from the green compacts begins with the solvent debinding process. The parameters for this process were enhanced using results from DSC and TGA test. The function of the solvent solution used, which is n-heptane was to remove paraffin wax and stearic acid. Then, a porous brown compact was formed once they had been removed. The existence of pores in the compacts enables backbone binder which is polypropylene (PP) to diffuse out during the thermal debinding process.

Figure 4.8 shows the mass loss of paraffin wax at various temperatures. In the first hour of the process, it can be presumed that as the debinding temperature increase, the loss of the binder also increases. Hence, when temperatures increase, it boosts binder diffusivity and solubility. Besides, more binder loss with the extended of debinding time. Correspondingly, it can be illustrated in Figure 4.9 that 4 phases occur throughout solvent debinding. Based on Md Ani et al. work (Md Ani et al., 2014), the phases of the process are discussed.

Phase I [0-60 minutes]: During this phase, loss of binder's component was quite fast as they are directly contacted with the solvent on the surface.

Phase II [60-120 minutes]: The rate of debinding decelerates. It is due to the solvent that enters intensely into the compact and the binder was extracted and liquefy into the surface.



Capillary forces helped the dissolved binder to diffuse to the exterior surface of the compact by liquid extraction (BECKER, 2006; Chikwanda et al., 2014).

Phase III [120-180 minutes]: The debinding rates start to rise due to adequate channels formed in the compact that permits the dispersion of the binder dissolved rapidly to the exterior surface of the compact. From the graph, the incline is the highest at 70°C which can be proved that the debinding rate achieves it peaks at this phase. At 50°C and 60°C temperatures, debinding rates on graph seem to be going at the similar leap. While, on curve 70°C, the debinding rate is reasonably high.

Phase IV [180-240 minutes]: From the graph, the mass loss of binder remains constant when the temperature increase and cause the debinding rate reduces. From this phase, the saturation point of the solvent and the binder had been achieved. However, it should be alert that the stability point among the latter is reliant on the solvent-binder component volume ratios.

The comparison of binder diffusivity and solubility to changes in temperature can be seen from the graph of the debinding rate at 50 and 60°C. For phases II-IV which is at 50°C, the debinding rate seems to be consistently reduced, where inclines are nearly constant. In contrast, at 60°C, phases II-IV, the debinding rate seems to increase to 180 minutes. Previously, from chapter two, in Figure 2.4, the overview of solvent debinding mechanism was illustrated, besides the conditions of the binder and diffusion of solvent during debinding. Debinding rates throughout the debinding process are reliant on the movement of molecules from dissolved binder, where they commonly move more rapidly with increasing of temperatures and smaller solvent molecules as reported by German and Bose (Randall M German et al., 1997).

Researchers had stated that, when the temperature of solvent debinding exceeds the highest melting point of the soluble binder components, MIM compacts will start to collapse (Md Ani et al., 2014). Figure 4.10 shows compacts are collapse and cracks after solvent debinding. High solvent temperatures, longer debinding times, and thickness variation of the component are the reasons behind all those conditions from the Figure 4.10. The compact will crack due to insoluble binder component due to longer soaking time. Besides, higher temperature makes binder soften which effects green compact to crack (M Rafi Raza et al., 2012). Therefore, it is why cracking demonstrates on the surface

of the compact as shown in Figure 4.10. These external defects were detected from the compact debound at 70 °C for 240 minutes debinding time. While compact debound at 60 °C temperature shows the efficient amount of paraffin wax mass loss after 240 minutes which is 76.9 % PW loss with no defects on the surface existing on the compact.

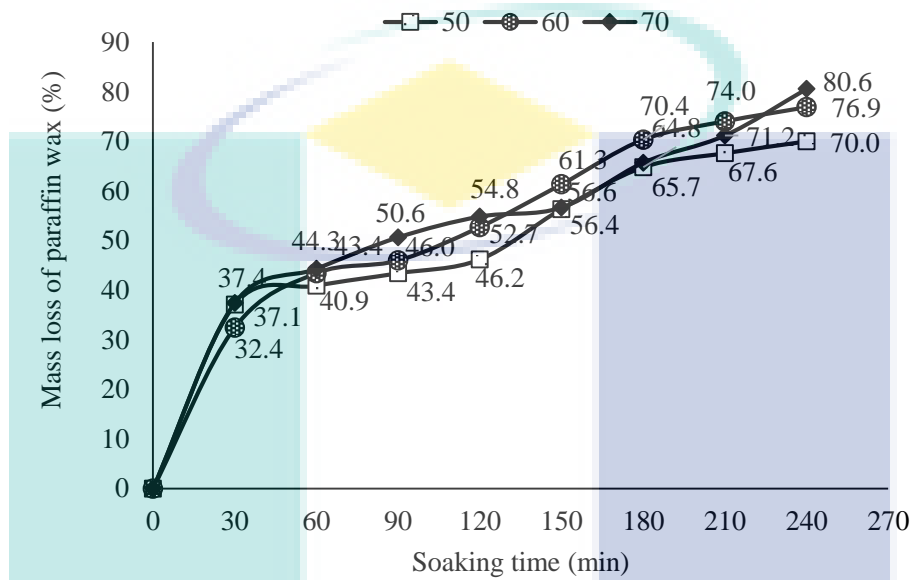


Figure 4.8 Time vs Temperature plot for paraffin wax’s mass loss during solvent debinding

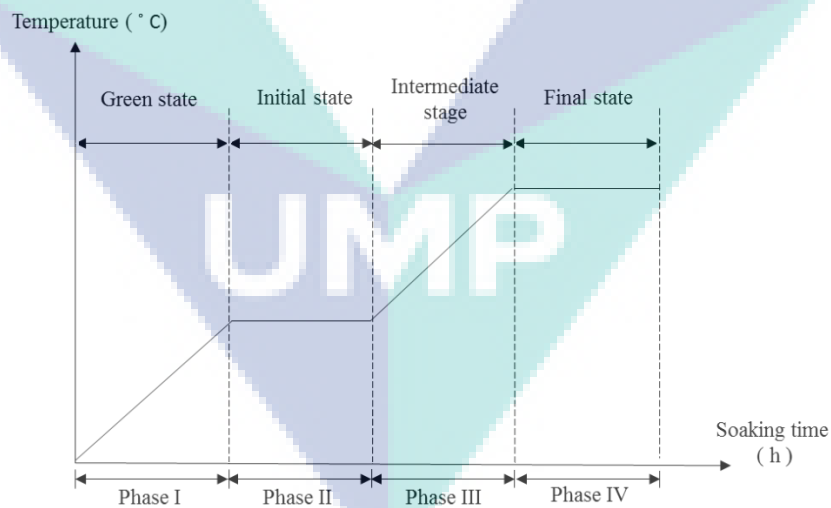


Figure 4.9 A schematic graph of paraffin wax loss for each phase

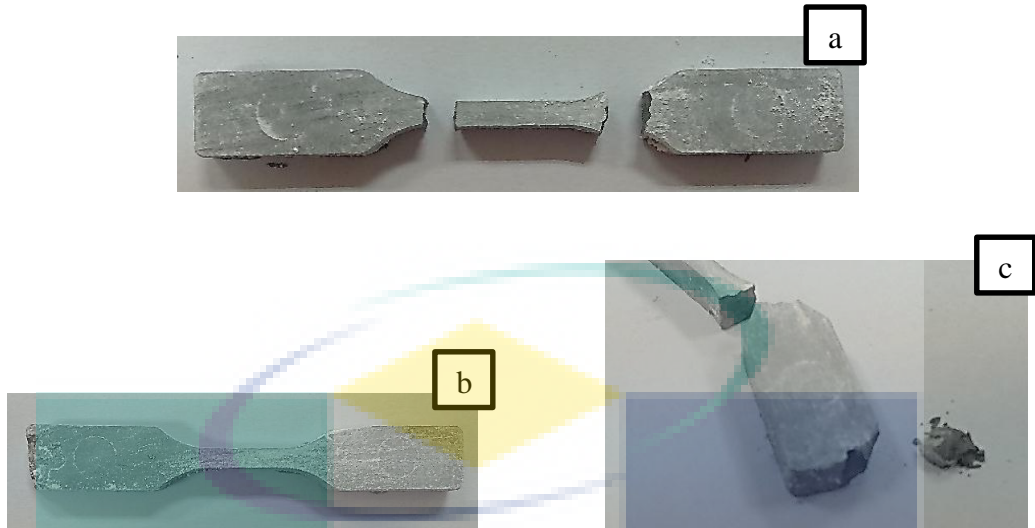


Figure 4.10 Defects observed on brown compact a) Fractures b) collapse c) cracks at conditions 70°C and 4 hour

From Figure 4.11, SEM micrographs had demonstrated the microstructure image of compacts before and after solvent debinding respectively. The brown compact after solvent debinding was obtained from the green compact debound at 60 °C for 240 minutes. From Figure 4.11 a), it can be realised that the metal particles was squarely scattered in the binder matrix. Then, uniform binders distribution can also be detected in the compact. While from Figure 4.11 b), after solvent debinding, it is clear that open pore channels had formed beside PW, and SA binders had been removed. The result has proven that n-heptane solvent manages and success in extracting the PW from the green compacts. There is also remaining binder in the compact which helps to retain the shape of the compact before thermal debinding process which is polypropylene.

An observation by SEM analysis confirmed that the open pore channels generated throughout the compact matrix. The open pore channels lead the residual binder especially polypropylene to be removed without altering the physical structure of the compacts during the thermal debinding stage. Without effective open pore channels, the remaining binder will force powder particle of the compact outward leading to uneven external surface and internal crack to the compacts (Chikwanda et al., 2014). Hence, the adequate solvent debinding process is needed in ensuring the success of the subsequent process which is the thermal debinding process and maintain the integrity of the compact (Zaky, 2004).

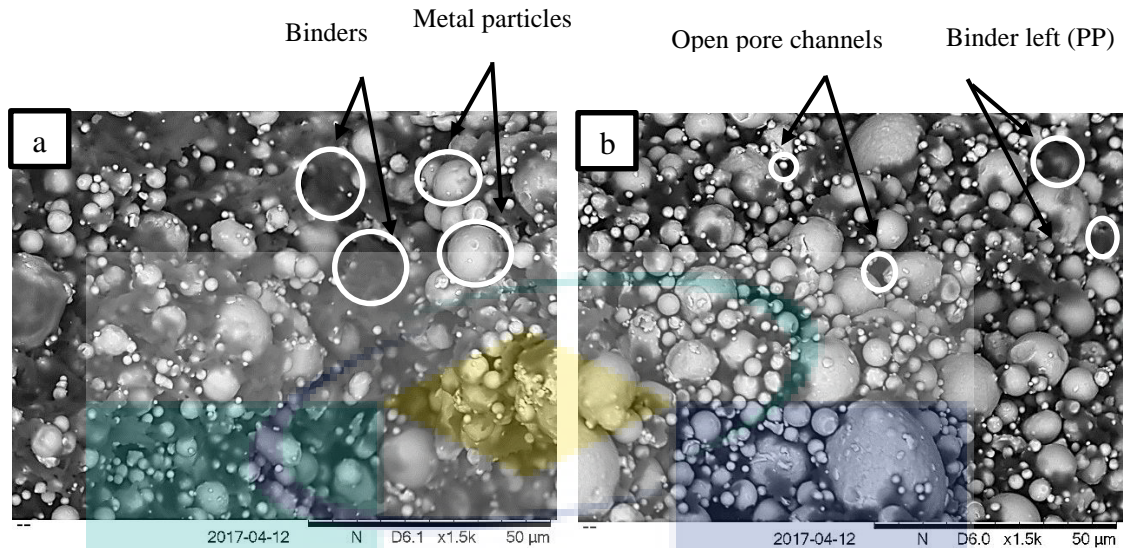


Figure 4.11 SEM micrographs of green compact before solvent debinding (a) and brown compact after solvent debinding (b)

#### 4.6 Thermal debinding and sintering process

Sintering is the last stage in the MIM process, and it was one of the most critical processes compared to others as it ensures the conditions the final compacts. Sintering parameter includes sintering temperature and sintering time was manipulated in this study. There is six sintering condition were analysed using three different range of temperatures which are 1250, 1300 and 1350°C with two different sintering time which are 1 and 3 hours. These parameters were based on the previous study related to MIM process of CoCrMo alloy (Henriques et al., 2015; Mohd Afian et al., 2014; Wahi et al., 2016). In this research, for thermal debinding, the compacts were heated at a temperature of 500°C for the thermal debinding process to eliminate all the binders' component from the compacts. Then, the brown compact will undergo a sintering process which is a continuous process from thermal debinding in an argon atmosphere furnace based on suggested parameters. While, Figure 2.5 shows the diffusion mechanism of particles during this process where at the last stage, the neck growth occur which enhances the bonding between particles. The sintering temperature was set at lower than the melting temperature of CoCrMo alloy to prevent overdue shrinkage and allow sufficient grain growth. After all the compacts undergo sintering process at various parameters, the sintered compact shows the promising result as shown in Figure 4.12. This shows that the sintering parameters such as sintering temperature, sintering time, heating rate and sintering atmosphere used in this work were appropriated.

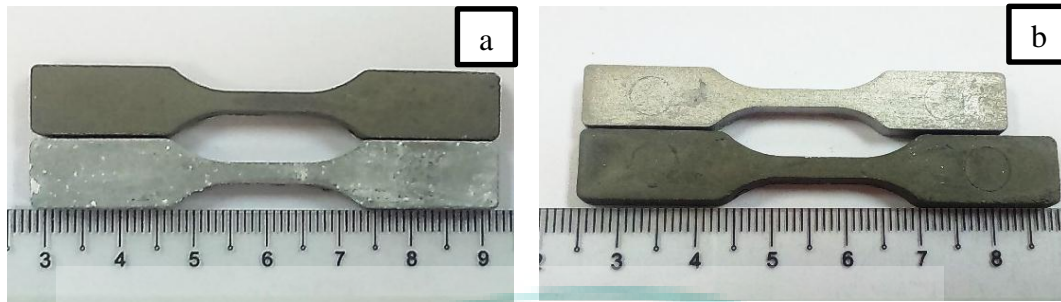


Figure 4.12 CoCrMo compacts (a) Green vs brown compact (after debinding) (b) green vs sintered compact (after sintering)

## 4.7 Characterisation of sintered compact

### 4.7.1 Microstructure study

#### 4.7.1.1 Porosity analysis

Figure 4.13 shows the microstructure of the various CoCrMo alloy sintered compacts observed under optical microscope. The compact sintered at 1250°C-1h and 1250°C-3h showed the sharp-edged/ irregular shape of pores and large pores on the surface of compacts. The phenomenon was due to the insufficient sintering process at low sintering temperature and short holding time resulted in diminishing the mechanical properties. The sintered compact from 1300°C-1h and 1300°C-3h demonstrated that the sharp edged-pores (happens due to higher surface area expose to air at the surface of compact) are also detected in grain boundaries but at 1300°C-3h shows a lesser amount of pores as compared to compare sintered at 1250°C-1h, 1250°C-3h, and 1300°C-1h.

Subsequently, the compacts sintered at 1350°C-1h showed the pore shapes evolved from irregular to spherical shape, and smaller than compact sintered at 1300°C-1h and 3h. The lowest amount of pores observed on the sintered compact under the sintering condition of 1350°C-3h, and most of the pores were in small spherical shape. The results indicated that the suitable sintering process occurred at higher temperature and longer holding time and this sintering parameters undoubtedly affected the mechanical properties of the compacts.



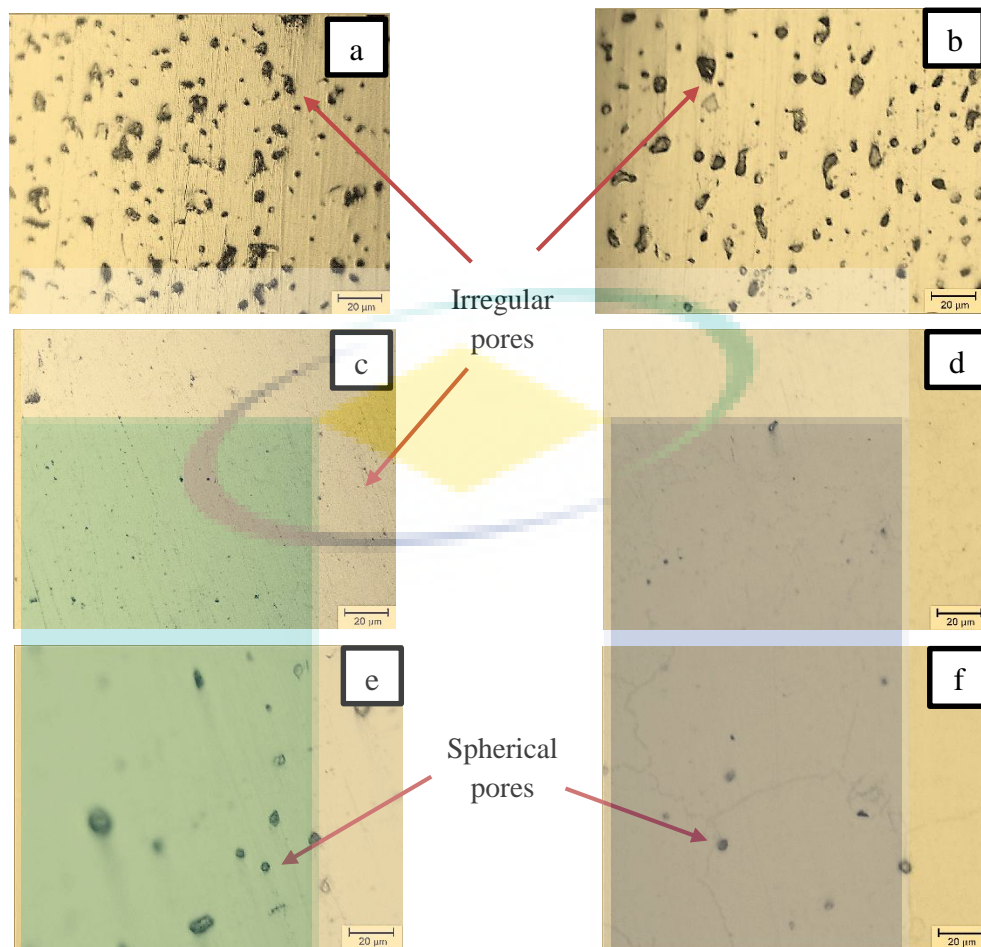


Figure 4.13 Optical micrograph of sintered compact; (a) 1250°C-1h; (b) 1250°C-3h; (c) 1300°C-1h; (d) 1300°C-3h; (e) 1350°C-1h; (f) 1350°C-3h.

From Figure 4.14, the average amount of porosity which are 16.8, 9.8, 5.2, 1.6, 1.2 and 0.2 % was observed for compact sintered at 1250°C-1h, 1250°C-3h, 1300°C-1h, 1300°C-3h, 1350°C-1h and 1350°C-3h respectively. The amount of porosity in the sintered compact decreased with increasing of sintering temperature and time. The increasing of sintering condition; temperature and time result in the removal of small pores. Previous work by (Kurgan, 2014) had found that the average porosity observed for the compacts sintered at 1200, 1250 and 1300 °C for 30 min were 20.12, 17.11 and 12.29 %. The study observed that the sintered compact with a lower amount of porosity showed better mechanical properties. While, from the results obtained by this study, it shows that when the sintering temperature was increased and holding time was prolonged, the amount of porosity appeared was much lower. Another work by Gupta (Gupta, 2005) the low sintering temperature applied yielded to poor density and tensile strength values in the powder compaction process of CoCrMo. From the evaluation of porosity volume, they discovered that, when the sintering temperature was increased to 1300 °C and above, the

number of pores decreases and the small size of pore detected compared to the sintering condition. During heating, diffusion mechanisms become active at high temperature and time result in a reduction of porosity. Therefore, enough energy supplied to the powder particles help the powder to bond massively (Fayyaz et al., 2018; Johari et al., 2016).

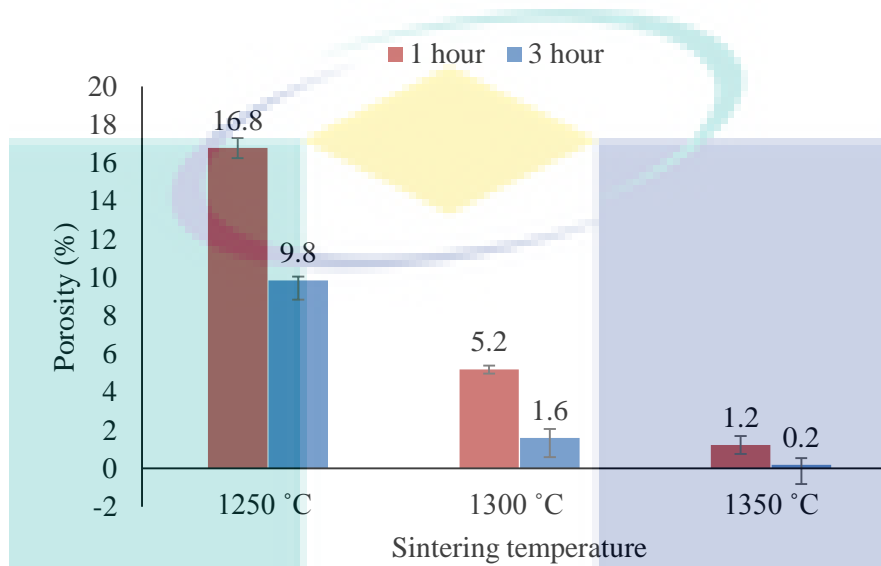


Figure 4.14 Amount of porosity of CoCr-based alloy sintered compact by Image J Analyser Software

#### 4.7.1.2 Grain size analysis

Table 4.2 demonstrates the distribution of grain size of sintered compacts obtained by ImageJ analyser software. The average results obtained were 12.6, 8.9, 11.2, 36.8 and 42.1  $\mu\text{m}$  from the grain size measurement of the sintered compact with a sintering condition 1250°C-3h, 1300°C-1h, 1300°C-3h, 1350°C-1h and 1350°C-3h respectively. However, at 1250°C-1h, lowest sintering temperatures and time, the size of the grain size was invisible. From the table, formation of the grain size of the sintered compact increased with the increasing of sintering temperature and time. This phenomenon also has been agreed by other researchers (Kurgan, 2014; Sotomayor et al., 2010b). During sintering, the interaction between pores and grain boundaries can have three forms: the pores can retard grain growth, the moving grain boundaries can drag the pores during grain growth or the grain boundaries can break away from the pores, leaving them isolated in the grain interior. As the temperature increases, the rate of grain boundary motion increases too. A breakaway of the boundaries from the pores occurs because the pores are moving slower than the grain boundaries (Ji et al., 2001).



Figure 4.15 shows the optical micrograph of sintered compact at 1250°C-1h; 1250°C-3h; 1300°C-1h; 1300°C-3h; 1350°C-1h; 1350°C-3h. From the figure, no formation of grain size was detected on the surface of the compact at 1250°C-1h sintering condition. It also can be observed, at shortest sintering time and lower sintering temperature, the particles of the compact were not completely diffuse. Nevertheless, when the sintering time was prolonged, the grain size starts to appear and could be seen at sintering condition of 1250°C-3h, 1300°C-1h and 1300°C-3h. When it reach sintering conditions of 1350°C-1h, the grain size was undoubtedly become bigger. Examination of the distribution of the grain size shows that in the CoCrMo at 1350°C-3h compacts, biggest grains size are overrepresented, apparently as the result of the isolated growth of a part of the grains at higher temperature and longer sintering time. Besides, From Figure 4.15, in this condition, it indicates that the size of the grain boundary is moderately broad and bright compared with other conditions. Johari et al. stated that (Johari et al., 2016) coarsening of microstructure and increase of grain size would deteriorate the mechanical properties. In this research, From the microstructural characteristics of the CoCrMo of 1350°C-3h compacts, although bigger matrix grains, coarser grain boundary was formed, the lowest percentage of porosities had led to increase in density, hardness and strength.

Table 4.2 Grain size analysis sintered compacts for each sintering condition

Sintering conditions	1250°C-1h	1300°C-1h	1350°C-1h	1250°C-3h	1300°C-3h	1350°C-3h
Grain size (µm)	-	8.9	36.8	12.6	11.2	42.1

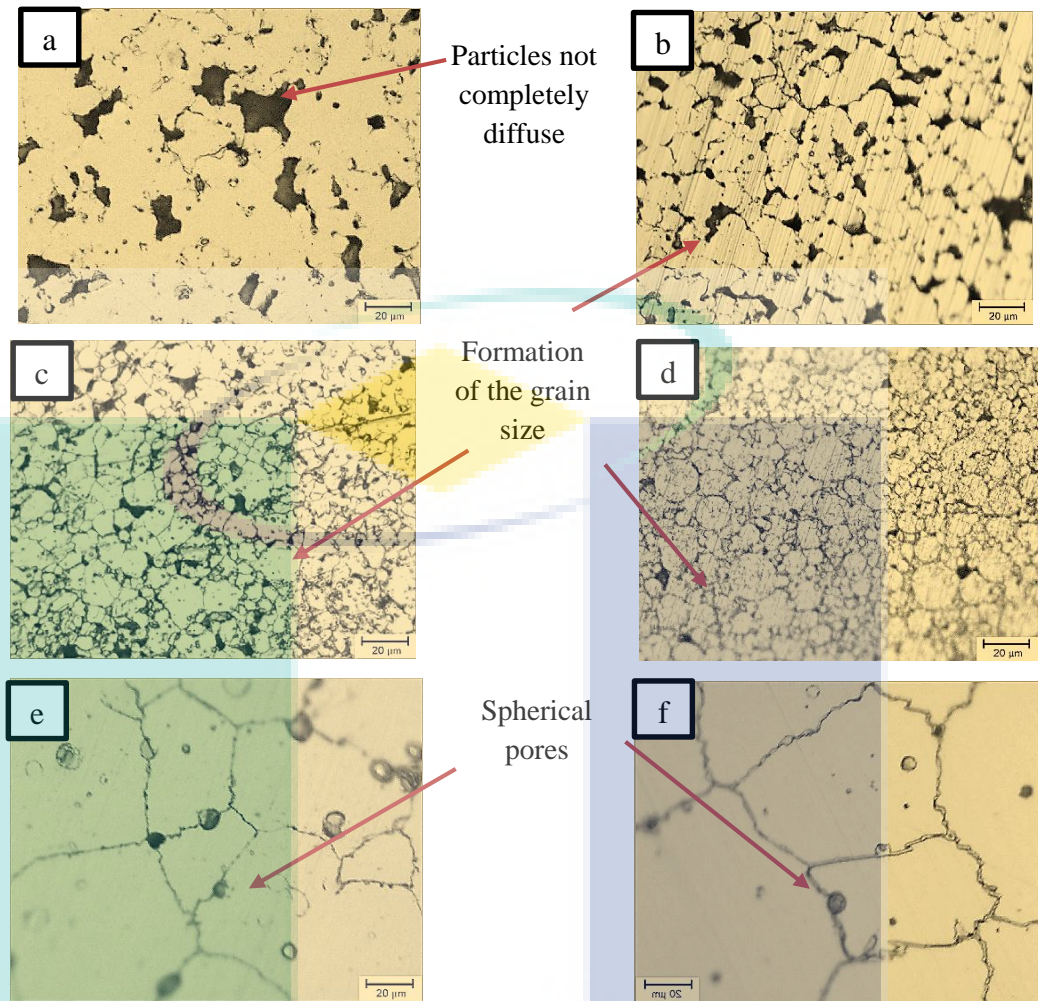


Figure 4.15 Optical micrograph of sintered compact; (a) 1250°C-1h; (b) 1250°C-3h; (c) 1300°C-1h; (d) 1300°C-3h; (e) 1350°C-1h; (f) 1350°C-3h

## 4.7.2 Physical properties

### 4.7.2.1 Dimensional accuracy between green compact and nominal mould

Figure 4.16 presents the dimensional accuracy of the nominal mould dimension and green compact. The dimensional accuracy was determined by comparing with nominal mould dimension from the schematic dimension of the tensile shape. It was differ based on length, thickness, and width. From the graph, the percentage of dimensional accuracy based on the length measurement of the green compact is near 100 % which is about 98.8 %. While, for the width, the results also show that green compact performs almost accurate measurement which is 99.68 %. Concerning thickness, the dimensional stability of green compacts is accurately same with nominal mould dimension. From the result obtained, the dimensional accuracy of the green compact based on its length, width

and thickness are consistent and better with the higher similarity of dimensional accuracy with the dimension of the nominal mould. Therefore, the green compacts obtained from this work is suitable for further processing in MIM.

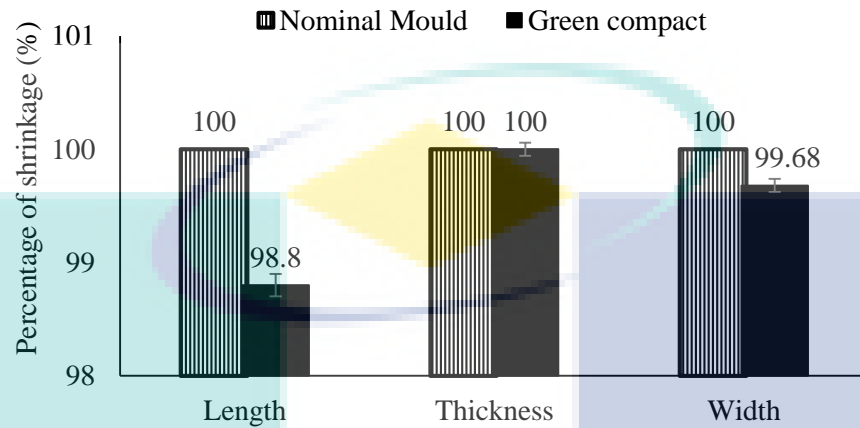


Figure 4.16 Dimensional change of sintered compact

#### 4.7.2.2 Shrinkage analysis

Throughout the MIM process, compacts had undergone binder removal through solvent and thermal debinding process and end with the sintering process. During sintering, the void spaces between the powder particles were disconnected, causing densification and shrinkage of the sintered compact. Thus, throughout those processes, the dimensional modification in the compacts was affected. The changes in dimension of a compact are known by the linear shrinkage ( $\Delta L/L_0$ ), where  $\Delta L$  is the dimensional change between the green compact and the sintered compact, and  $L_0$  is the dimension of the green compact. The dimensional shrinkage of the green and sintered compacts was measured by the changes of its dimensions as shown in Figure 4.17.

Sintering is the critical process that dominates the phase in dimensional variation, in which shrinkage might range from 14 to 24 % (Randall M German, 1996). However, the calculated percentage of shrinkage in this study is a bit lower which is ranged from 4.9 to 5.9 %. Azizah et al. (Wahi et al., 2016) had stated that the limit range of powder loading used is between 64 to 69 %. Hence, the small changes of shrinkage value in this study possibly due to the high powder loading used which is 67 vol. %. The highest shrinkage resulted from sintered compact with a sintering condition of 1350°C-3h. While the sintering condition at 1250°C-1h shows the lowest percentage of shrinkage. From

Figure 4.17 the amount of shrinkage increased with the increases of sintering temperature and time. Previous work by (M. A. Omar et al., 2012) found that the shrinkage of the sintered compact will rapidly increase from 12-15% when the sintering temperature increased from 1300-1360°C. As seen in Figure 4.18, the shrinkage result raised with the increase of sintering temperature and time. During the sintering process, the particles start to diffuse and formed neck growth. As the sintering temperature increase, it develops the contact length among the particles through grain boundary diffusion, volume diffusion and plastic diffusion which also increase the linear shrinkage of the sintered compacts (Aslam et al., 2016).

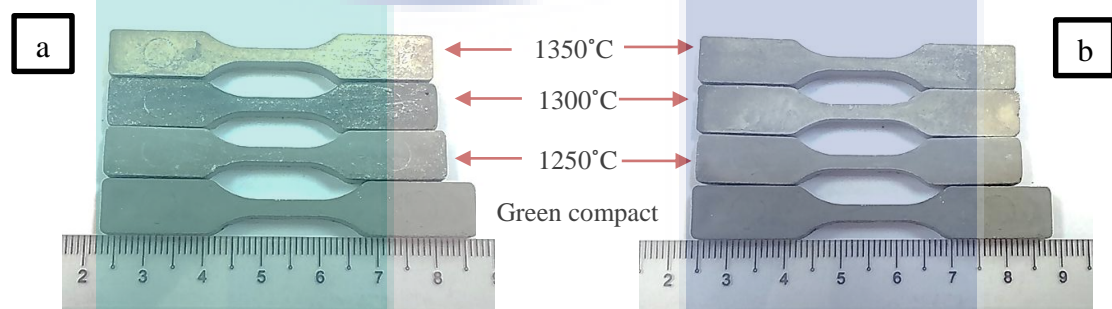


Figure 4.17 Dimensional change of sintered compact at 1h sintering condition (a) and 3h (b)

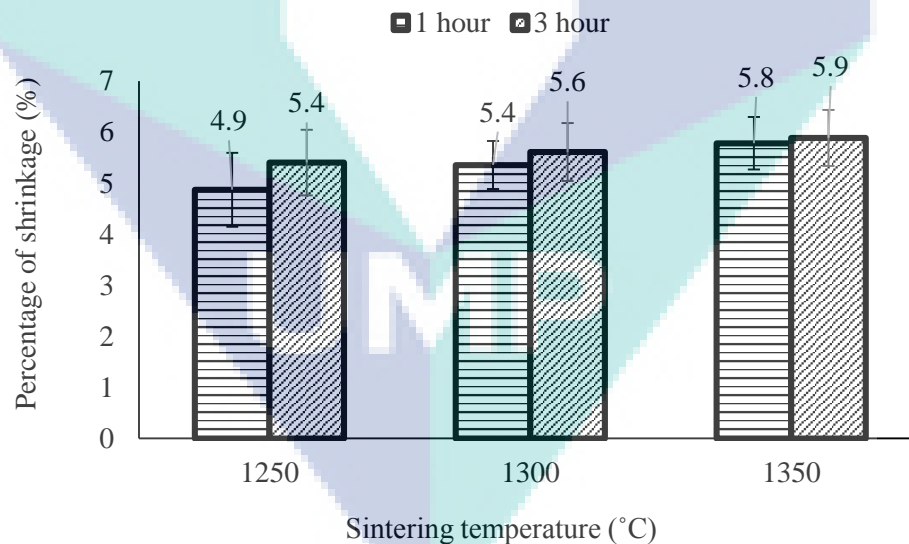


Figure 4.18 Percentage of shrinkage for CoCrMo alloy sintered compacts.

#### 4.7.2.3 Density analysis

For the compacts characterisation, Archimedes' principle was applied to measure the densities of sintered compact. The relative density obtained was based on the theoretical density of CoCr-based alloy which 8.4g/cm<sup>3</sup>. The relative density of each

compact condition is shown in Table 4.3. The table demonstrated the relative density of 1250°C-1h, 1300°C-1h, 1350°C-1h, 1250°C-3h, 1300°C-3h and 1350°C-3h which were 7.19 g/cm<sup>3</sup> (85.6 % theoretical density), 7.40 g/cm<sup>3</sup> (88.1 % theoretical density), 7.35 g/cm<sup>3</sup> (87.5 % theoretical density), 7.43 g/cm<sup>3</sup> (88.4 % theoretical density), 7.70 g/cm<sup>3</sup> (91.7 % theoretical density) and 7.77 g/cm<sup>3</sup> (92.5% theoretical density) respectively. The highest relative density was recorded on 1350°C-3h sintered compact condition which is 92.5 %. Meanwhile, the lowest relative density was obtained from the 1250°C-1h sintered compact condition. As shown in Table 4.3, the density of the compact improved with the increasing sintering temperature and prolonged sintering time.

Previous work from Azizah et al., (Wahi et al., 2016) they found that at 1250, 1300 and 1350 °C sintering temperature the relative density achieved was 76, 87 and 93 % for 2 hours holding time under vacuum atmosphere with 2 °C/min heating rate. The study observed that, with increasing of sintering temperature, good mechanical properties of compacts could be achieved. By comparing the results obtained by this study, in 1250, 1300°C-1h and 1250, 1300°C-3h sintering condition, the low increment of density result is obtained which is about 1.4 %. While, when the sintering temperature was increased to 1350 °C, the higher increment of density can be obtained. However, applying a prolonged sintering time increased the densification process result in an increase of density value. This has a good agreement from the study by Obasi et al., (Obasi et al., 2010) where they observed sintering for only 1 instead of two hours reduced the density and strength of compacts significantly.

Table 4.3 Density of CoCrMo alloy sintered compact.

Sintering conditions	Sintered density (g/cm <sup>3</sup> )	Relative density (%)
1250°C-1h	7.19	85.6
1300°C-1h	7.35	87.5
1350°C-1h	7.70	91.2
1250°C-3h	7.40	88.1
1300°C-3h	7.45	88.4
1350°C-3h	7.77	92.5

The optical microstructure images in Figure 4 confirmed the result of the relative density in this study through the amount of porosity demonstrated in the previous section. Figure 4.19 summarises the relationship between density, the amount of porosity and percentage of shrinkage from six conditions of sintered compacts. From Figure 4.19, it is apparent that the amount of porosity for the sintered compacts is inversely proportional



to the relative density i.e the increase of relative density results in the lower porosity amount whereas, higher relative density leads to the higher amount of shrinkage in the sintered compacts. This demonstrates that the void spaces among the powder particles were detached thru sintering, causing shrinkage and densification of the compacts. From the figure below, it validates that the highest density value at 1350°C-3hs obtained is achievable due to the fewer amount of porosity exist which was 0.2 %. Hence, it can be stated that the increase in sintering temperature and time will lead to the low amount of pores formed, and tally with this research works obtained, where it proves, the amount of porosity is relatively related with the density value. From Johnson et .al, (Johnson et al., 2005) it reveals that pore-free condition compact was likely obtained in higher sintering temperature cases, while with impurities in the compact will resulting in lower theoretical densities.

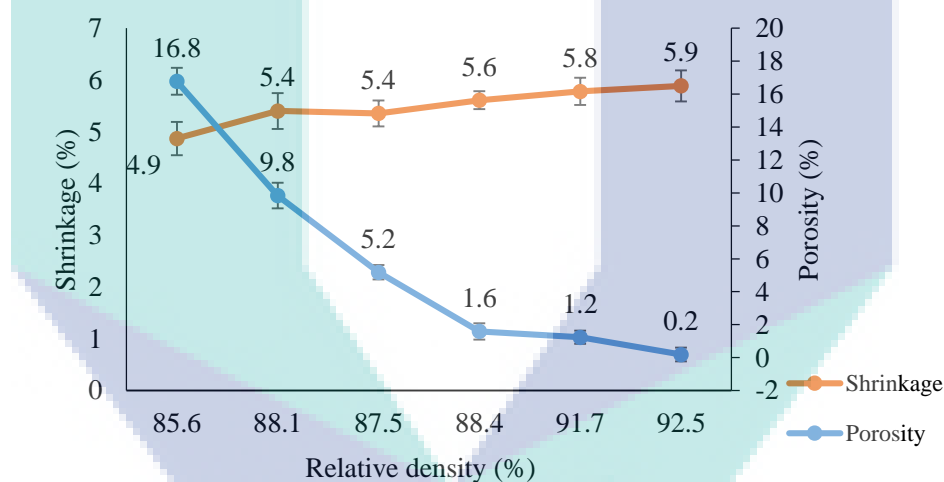


Figure 4.19 Relation between density, amount of porosity and percentage of shrinkage for CoCrMo alloy sintered compacts

### 4.7.3 Mechanical properties

#### 4.7.3.1 Hardness measurement

Figure 4.20 shows the hardness results of the sintered compact obtained in this study. The result of hardness is 173.07, 201.9, 187.2, 213.73, 230.66 and 308.07 HV for 1250°C-1h, 1250°C-3h, 1300°C-1h, 1300°C-3h, 1350°C-1h and 1350°C-3h sequentially. The increase of sintering temperature and time affects the hardness of sintered compacts. Moreover, the increase in the hardness result also correlates with the decrease of porosity

and increase of the density of sintered compact. Figure 4.21 shows the relation between hardness and amount of porosity for each sintering condition. The highest hardness value was obtained by the compact 1350°C-3h which was 308.1 HV.

The hardness result is comparable with the CoCrMo alloy of Cast ASTM F75 study by George et al. (Bellefontaine, 2010) in which the highest hardness achieved was 310 HV. While in this study, the sintering temperature of 1250°C-1h produces the lowest hardness of 173.1 HV. Similar to the result indicated by density value, which is related to the amount of porosity. It can be stated that the lowest hardness value caused by the void and spaces occur in the compact due to low sintering temperature and time. Where the surface area between the particles become more significant due to the highest form of a pore in the compacts. From Figure 4.21, it can be summarised that, when the percentage of porosity increase, it leads to a lower hardness value. The high rate of densification during sintering resulted in higher hardness, and density due to less porosity remain in the sintered body (J. He et al., 2018; C. Wang et al., 2012).

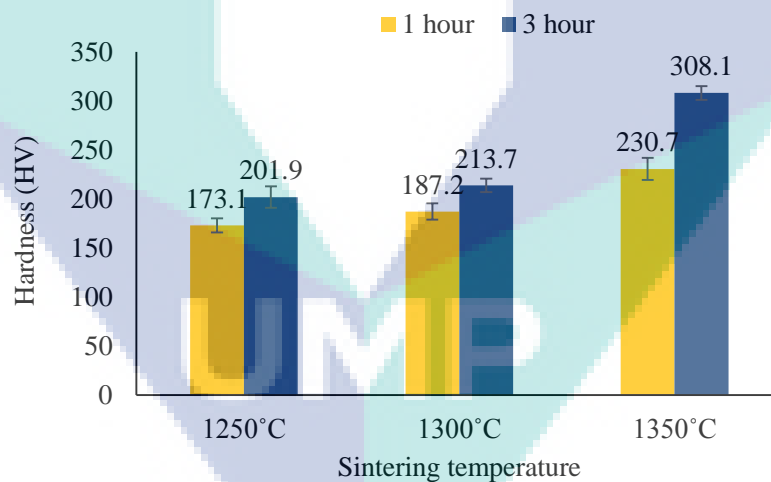


Figure 4.20 Micro-hardness of CoCrMo alloy sintered compacts



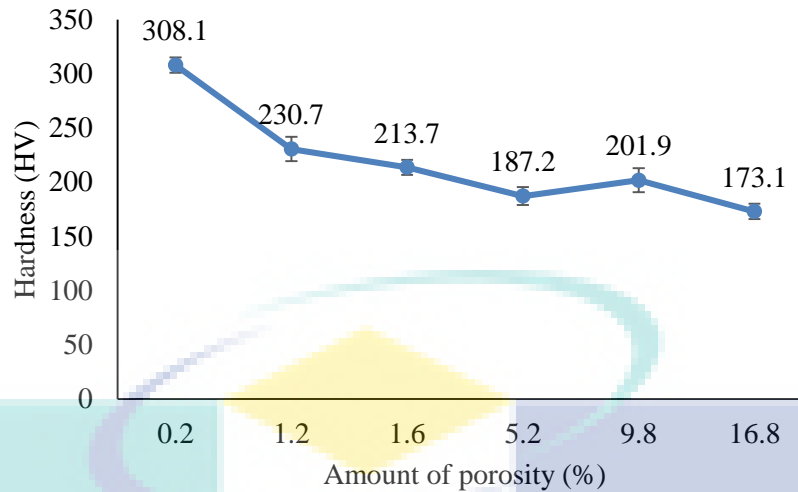


Figure 4.21 Relation between hardness and amount of porosity for CoCrMo alloy sintered compacts

#### 4.7.3.2 Stress-strain curve and microstructure analysis

Figure 4.22 shows the stress-strain curves for different sintering conditions of CoCrMo alloy in this study. The properties of sintered CoCrMo compact from the stress-strain curve graph are compiled in Table 4.4. From Table 4.4, the highest ultimate tensile strength achieved at the sintering temperature of 1350°C-3h soaking time which meets the ISO standard 5832-4. As predictable, the differences in microstructural topographies could be as evidence to correlate with the compacts that perceived higher strength when sintered at a higher temperature. The phase of densification or identified as the number of pores appear to be the utmost significant factor that affected the tensile strength of the compacts. Despite that, the increase in density value also affected the tensile strength of the sintered compact. Where, at the higher result of density, it provides a stronger interparticle bonding, which hinders crack propagation and leads to higher tensile strength (M. A. Omar et al., 2012). From the mechanical properties of the sintered compact in Table 3.4, it can be concluded that, at 1350°C-3h, when the strength is increased, the elongation tends to be a bit lower. These results are in a good agreement with the results reported by Azizah et al. (Wahi et al., 2016) where, at a higher strength, the elongation tends to become lower. While, at the lowest temperature, which is for condition 1250°C-1h and 3h, the compacts were experienced to have lower strength and ductility. This is due to the higher amount of porosity presents in the compacts compared to other condition.

Referring to Levine’s work (Levine, 1987), a required condition for ductility in F75 (alloys commonly used commercial or proprietary names to describe CoCrMo alloys that are used in surgical implants) is the discontinuous carbide formation along the grain boundaries, whereas massive, continuous carbides form at grain boundary, along with entirely clean grain boundaries without carbides, lead to a low of ductility correspondingly. Therefore, a bit lower elongation result may take place at sintering condition at 1350°C-3h was due to the formation of carbide at the grain boundary.

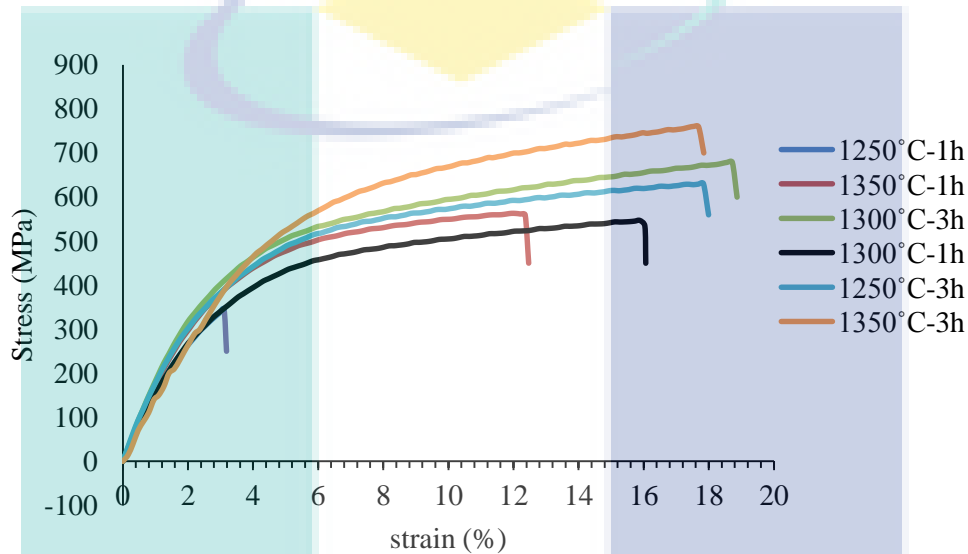


Figure 4.22 Stress-strain curves at different sintering condition for CoCrMo alloy sintered compacts

Table 4.4 Yield stress, Ultimate tensile strength, and elongation of the compact at different sintering condition

Sintering condition	Yield stress, $\sigma$ (Mpa)	Ultimate tensile strength (Mpa)	Elongation, $\epsilon$ (%)
1250 °C-1h	200	318.9	1.0
1300 °C-1h	340	442.3	10.0
1350 °C-1h	380	567.7	12.0
1250 °C-3h	450	613.9	12.5
1300 °C-3h	490	658.9	14.1
1350 °C-3h	550	728.4	12.0

#### 4.7.3.3 SEM/EDS characterisation

In general, the CoCrMo alloy microstructure presents a carbide phase with different composition depending on the alloying elements. Fig 4.23 gives an example of SEM image of the carbide presents in the CoCrMo alloy in this study. The concentration of the main alloying elements in large carbides was analysed with EDS, and the results are shown in Figure 4.24. It has also been observed that, in some cases, different carbides

coexist in large carbide clusters, especially when their size exceeds 20 microns as evidenced by the bright areas within the dark ones in the SEM image and the EDS analysis.

From the analysis, greyish type precipitation identified as carbide formation exist along the grain boundary which was the same as reported by Giacchi et al. (Giacchi et al., 2011). While, from EDS analysis, as shown in Figure 4.24, at 1350°C-3h, Cr rich carbides exist at the grain boundary of the compact. From previous research work by Johnson, it is reported that carbides at the grain boundaries produced by carbon in Co-28Cr-6Mo can diminish ductility which is unfavourable to mechanical properties of the alloy (Johnson et al., 2005; Narushima et al., 2013). Hence, it can be expected that the primary cause for the increase in micro-hardness and strength is the fewer amount porosity, while the lower elongation was due to the formation of excessive carbide precipitation in the compact at 1350°C-3h sintering conditions. For detailed characterisation of the carbide clusters and phase identification, XRD analyses were performed. The results are discussed in the following section.

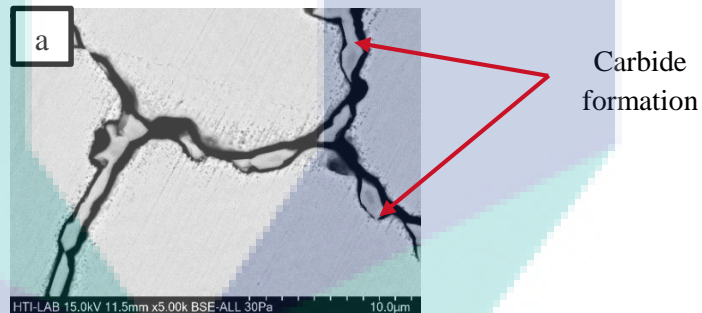


Figure 4.23 SEM image of sintered CoCrMo at 1350°C-3h.

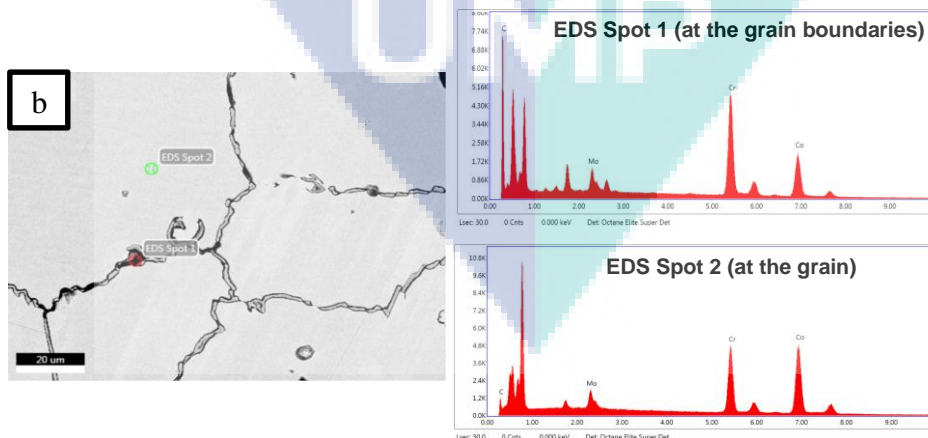


Figure 4.24 SEM image of sintered CoCrMo at 1350°C-3h (a) SEM image and EDS analysis of sintered CoCrMo at 1350°C-3h (b)

#### 4.7.3.4 XRD phase identification

Figure 4.25 shows the XRD pattern of compact sintered at 1350°C-3h sintering condition. It is possible to identify the carbides peaks in the pattern. However, carbides are not adequately detected on the highest peak by XRD because their mean peaks are in the same position as others phases stated on the pattern. Therefore, the main difference of lower elongation in this study is due to the presence of carbides and significantly larger grain size at higher sintering temperature and longer sintering time. The previous researcher reported that the different grain size and the residual grain boundary carbides are responsible for this difference which causes lower sintering temperature has good ductility than those sintered at higher one despite lower density (Vieira Muterlle, 2010).

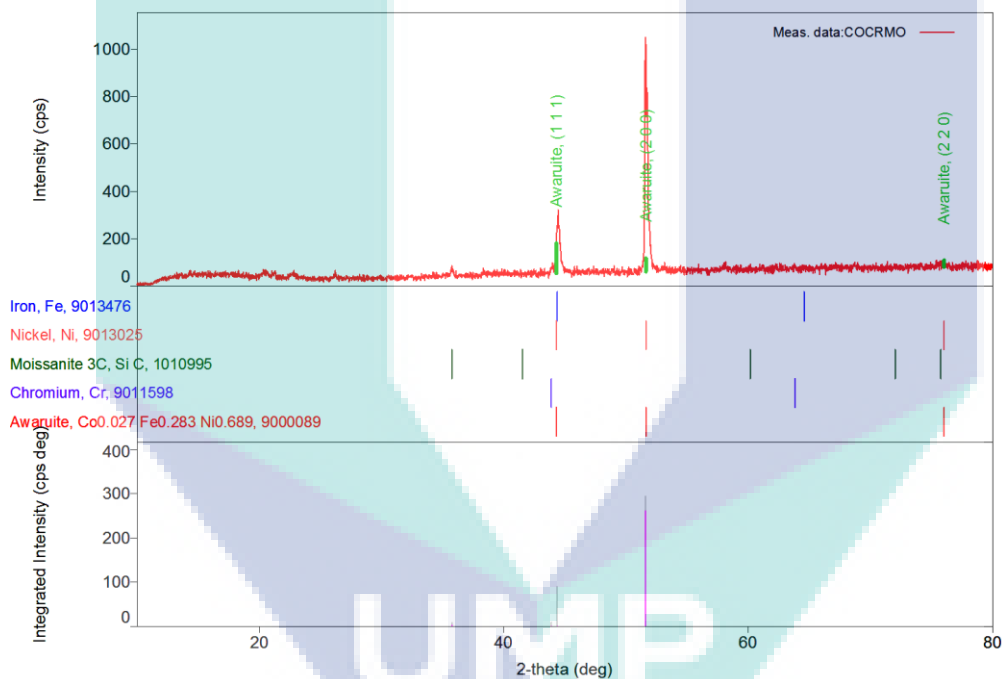


Figure 4.25 XRD analysis of sintered CoCrMo at 1350°C-3h

#### 4.7.3.5 Fracture surface analysis

The SEM analysis was used to observe the fractured surface and the porous structure of the sintered compact as shown in Figure 4.26. A clear transformation in fracture surface behaviour between the different sintering conditions is analysed. The strength of CoCrMo alloy compacts was shown to decrease with increasing of the size and amount of pores in the compact. Mainly, from the fractured surface analysis of the 1250°C-1h sintered compact, the larger pore size and lower amount of sinter neck

formation were observed. Also, an irregular pore formation with the largest size occurred at 1250 °C-1h sintered compact condition. While the most ductile structure attribute was found in the 1300 °C-3h sintered compact in Figure 4.26(d).

The increase in ductility for the sintered compact at 1300°C-3h, 1350°C-1h and 1350°C-3h were due to the smaller pore size, regular spherical pore and low amount of porosity formed at higher sintering temperature and an increase of sintering time. Regular pore formation with a small size can achieve a minimum amount of porosity and an increase in density. At 1250°C-3h, and 1300°C-1h, the irregular pores were also observed on the sintered compact. The irregular pore structure will affect the mechanical properties by diminishing the strength and hardness which causing the sinter neck to fracture immediately due to the stress-localised phenomenon and the sharp edge of the pores.

In Figure 4.26 (d) the fracture surface of 1300°C-3h, are shown. The failure mode is clarified as an intergranular with dimples, which accounts for the highest ductility achieved compared to others sintering condition. Only in the compact sintered at a higher temperature which is 1350°C, a brittle morphology is visible. Figure 4.27 shows the fracture surface of compact at 1350°C-3h sintering conditions. From the figure, the tensile test shows brittle fracture conditions of the compact was observed. In addition, for compact sintered at 1350°C-3h, fracture mode is fully intergranular and associated with the presence of carbides. With the increase of carbon content on the compact, strength increases, whilst ductility decreases because of the existence of carbide and fracture (P. Vieira Muterlle et al., 2009; Vieira Muterlle, 2010) behaviour which promote an intergranular fracture (P. Vieira Muterlle et al., 2009). Besides porosity, both carbides precipitation and mode of failure are responsible for this difference on the compacts for each sintering conditions.

In this study, the CoCrMo alloy compact at 1350°C-3h (7.77g/cm<sup>3</sup>) had shown excellent mechanical properties. The others sintering condition, especially at 1350°C-1h and 1300°C-3h, show excellent mechanical properties too, but due to its high porosity, they cannot be considered for the specific applications.



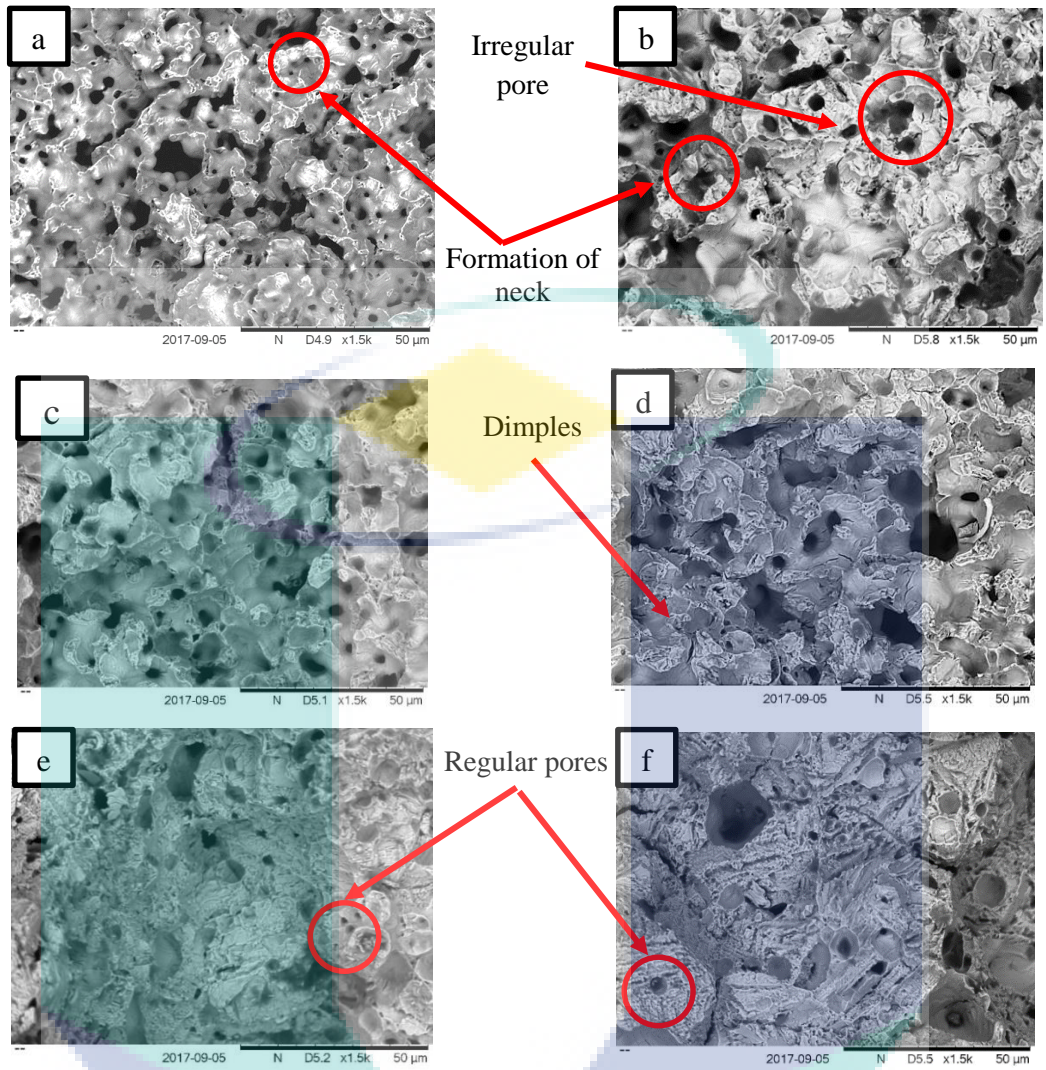


Figure 4.26 Fracture surface of sintered CoCrMo at (a) 1250°C-1h (b) 1250°C-3h (c) 1300°C-1h (d) 1300°C-3h (e) 1350°C-1h and (f) 1350°C-3h

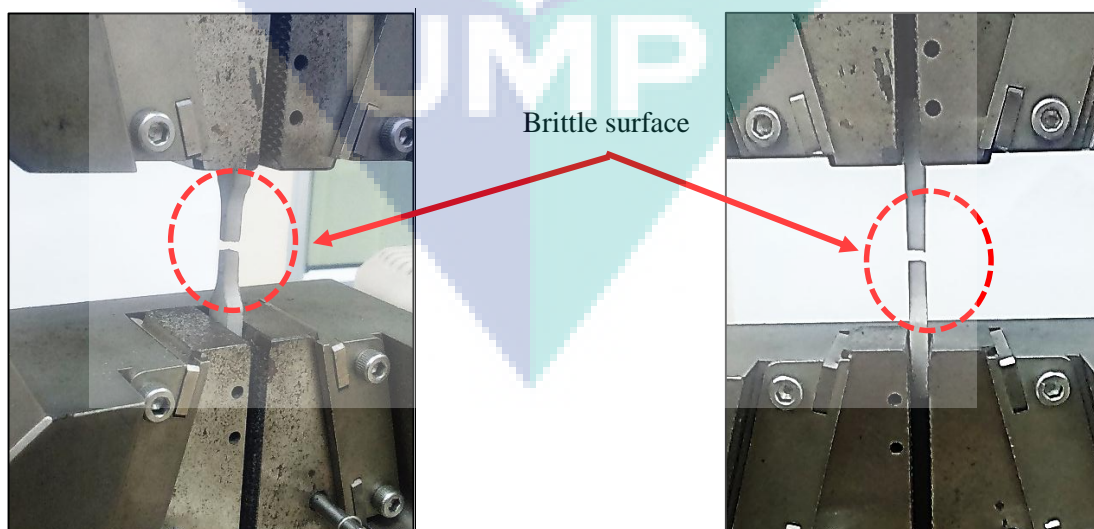


Figure 4.27 Brittle fracture surface of sintered CoCrMo at 1350°C-3h after tensile test



#### 4.8 Electrochemical properties of sintered compact

In order to better evaluate the stability of the passivity and the electrochemical behaviour of the sintered compacts at different sintering conditions, potentiodynamic curves were analysed. Figure 4.28 shows the potentiodynamic polarisation curves of each sintered compact at different sintering temperature and time in the Ringer's solution at 37°C. While the corresponding kinematics parameters extracted from corrosion potential ( $E_{corr}$ ) and corrosion current density ( $i_{corr}$ ) are summarised in Table 4.5.

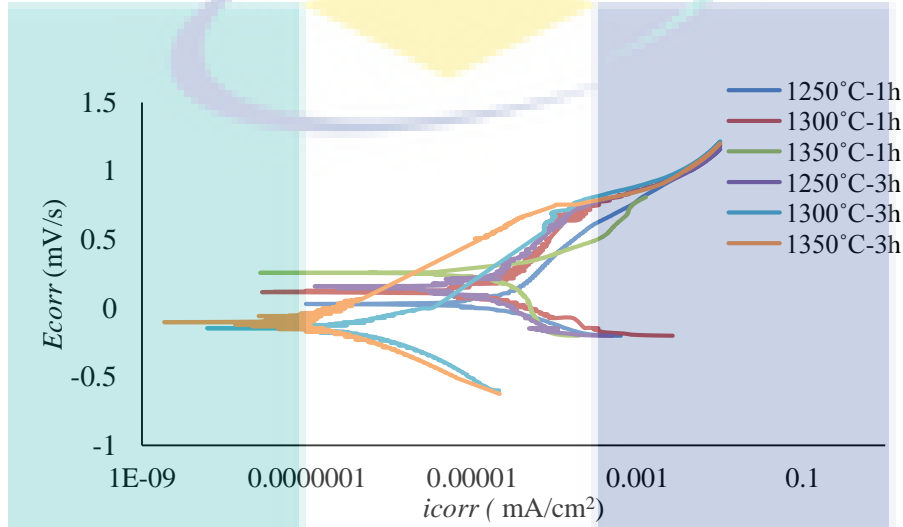


Figure 4.28 Potentiodynamic of CoCrMo compacts, sintered at 1250, 1300 and 1350°C for 1 and 3 h; Ringer solution, 37°C

Based on the result in Figure 4.26 the curve for sintering condition of 1350°C-1h shifted to a nobler potential but higher current density compared to 1350°C-3h sintering condition.  $E_{corr}$  and  $i_{corr}$  represent chemical stability and corrosion rate of metallic material respectively. The corrosion rate for all compact at different sintering condition was measured using (Asri et al., 2017) equation 4.2 and listed in Table 4.5. From the table, the value of the  $E_{corr}$  for 1250°C-1h was 1.17E-01mV, 1300°C-1h was 1.56E-01mV, 1350°C-1h was 2.58E-01mV, 1250°C-3h was 3.01E-02 mV 1300°C-3h was -1.47E-01mV and 1350°C-3h was -0.1018mV. The values of  $E_{corr}$  indicate the increase in corrosion resistance after the increasing of sintering temperature and time. This was also confirmed by the decrease of the  $i_{corr}$  values where  $i_{corr}$  for 1350°C-3h was the lowest which is 2.13E-07 mA/cm<sup>2</sup> upon higher sintering time which is 3 hour.

$$CR = K \frac{i_{corr}}{\rho} xEW \quad 4.2$$

Table 4.5 Corrosion behaviour analysis of sintered compacts, respectively

Sintering conditions	Corrosion potential, $E_{corr}$ [mV/s]	Corrosion current, $i_{corr}$ [mA/cm <sup>2</sup> ]	Corrosion rate [mm/year]
1250°C-1h	1.17E-01	1.90E-05	1.93E-04
1300°C-1h	1.56E-01	1.07E-05	1.09E-04
1350°C-1h	2.58E-01	1.25E-05	1.27E-04
1250°C-3h	3.01E-02	2.13E-05	2.16E-04
1300°C-3h	-1.47E-01	3.63E-07	3.68E-06
1350°C-3h	-0.1018	2.13E-07	2.16E-06

The precarious shortcomings of the MIM process are the risk to reduce the presence of pores on the sintered compact. The existence of pores enhances corrosion attack especially when the compacts were exposed to corrosive environment. The microstructure of the compact reveals the influences of the corrosion rate on the compact at different sintering temperature and time. Two causes affect the corrosion properties of compacts; first is the non-existence of passivation within the pore; second is the more significant surface area of the porous sintered compact (higher than the surface area of the external geometric surface area). Both causes are thought to be the reason that the compact becomes more defenceless to the corrosion attack (Vidal et al., 2009). Therefore, to report the problem, three parameters are used to enhance the corrosion resistance of the compact which includes sintered compact density, sintering atmosphere, and sintering temperature. The increase in density will reduce the number of pores which results in the decreased surface area for the corrosion to attack. Also, to gain high densification, sintering atmosphere and sintering temperature play essential roles where the rapid cooling from the sintering process will preserve the homogeneous distribution of the particle in alloy compact hence it will improve the corrosion resistance.

Figure 4.29 shows the corrosion rate of the sintered CoCrMo alloy compact decreased with the increase of sintering temperature and time. While from Figure 4.30, sintering conditions for 1350°C-3h show the lowest corrosion rate compared to other sintering condition due to the lower amount of porosity which leads to the smaller surface area exposed to the corrosion attack. Besides, Rodriguez et al. (Montero- Ocampo et al., 1995) conveyed that minor carbon content in the CoCrMo alloys might contribute to higher chemical and microstructural homogeneity and thus a better corrosion resistance. It has also been well accepted that the tolerable corrosion rate for metallic implant systems should be about 2.5E-04 mm/year (Asri et al., 2017). All the corrosion rate values from these six conditions have acceptable corrosion rate and fulfil the requirement of for

metallic implant. It is also proved that even though the MIM fabrication is one of the powder metallurgy methods to fabricate metal, it is highly recommended to be applied to fabricate metallic implant in future since the corrosion behaviour of the metal is acceptable. Besides, another powder metallurgy studied by Wilson (Rodrigues et al., 2011a) stated that for the invention of a CoCrMo alloy for dental implants were determined. With the claim of these factors, an alloy with appropriate green density, low porosity after sintering, considerable hardness and spontaneously passive behaviour in the Ringer solution had been achieved.

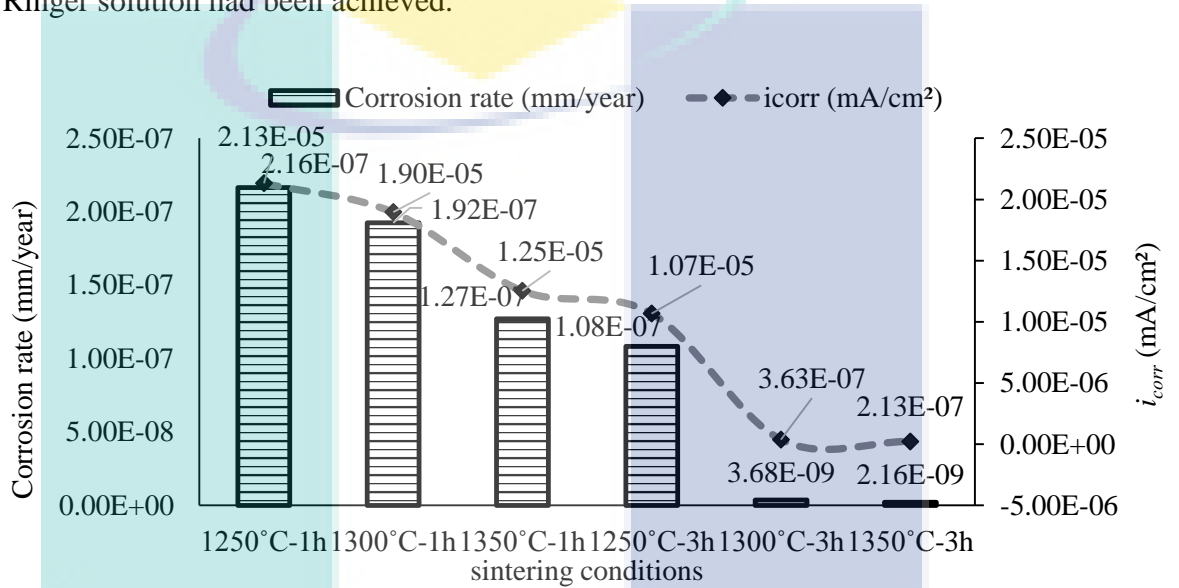


Figure 4.29 Corrosion rate vs corrosion current density ( $i_{corr}$ ) analysis of sintered compacts, respectively

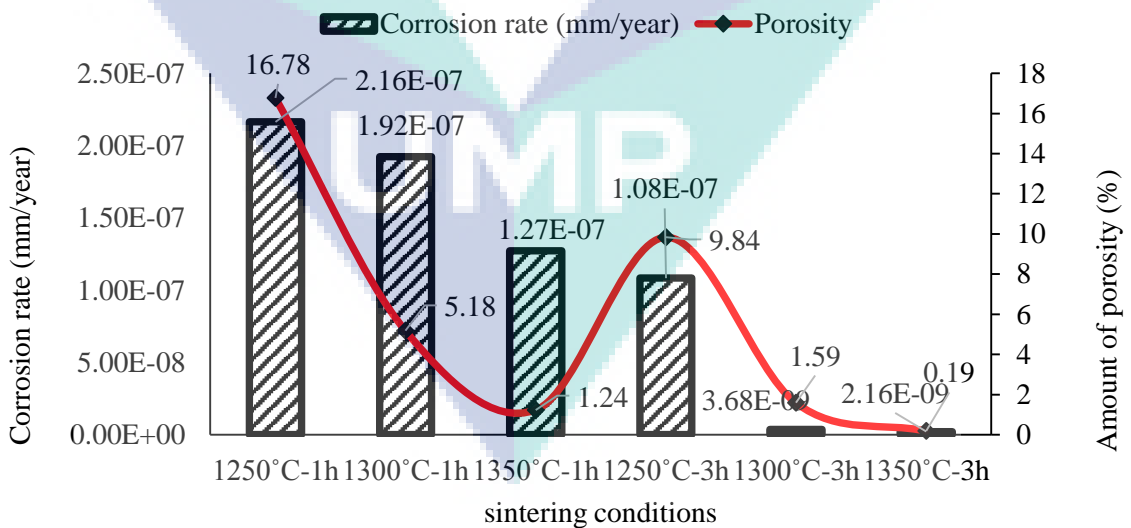


Figure 4.30 Corrosion rate vs amount of porosity analysis of sintered compacts, respectively

## CHAPTER 5

### CONCLUSIONS AND RECOMMENDATIONS

#### 5.1 Introduction

In this research, CoCrMo alloy sintered compact with six different sintering conditions was successfully fabricated by Metal Injection Moulding process. Based on the results obtained and its analysis, the following conclusions can be made.

#### 5.2 Conclusions

- i. Paraffin wax was extracted out from the green compact through solvent debinding process. The optimum solvent debinding parameters have been established at 60°C for 240 minutes as a result of the adequate volume of PW loss. The total percentage of optimum PW recorded was 76.9 %.
- ii. The less amount of porosity and defects free on the sintered CoCrMo alloy compact were achieved with higher sintering temperature and time. At 1250°C-1h sintering condition, the grain size could not be revealed due to the insufficient sintering temperature and time used, which cause weak particles bonding between powder particles. While, at higher sintering temperature and time, 1350°C-3h, the grain size becomes larger at 42.1  $\mu\text{m}$  and the existence of porosity is the lowest which is 0.2% compared to other sintering conditions.
- iii. The dimensional shrinkage increased with the increase of sintering temperature and time due to higher densification of the sintered compact. Highest shrinkage of 5.9% was recorded on a sintered compact with a sintering condition 1350°C-3h, while the lowest at 1250°C-1h which was 4.9%.

- iv. The relative density of the compact increases depending on sintering time and temperature. The highest relative density value which is 92.5 % has been achieved by a sintering condition at 1350°C-3h. Meanwhile, 1250°C-1h exhibited the lowest relative density of 85.6 %.
- v. The increase in ultimate tensile strength is associated with the increase in the sintered compact density. A smaller pore size and lower amount of pore clustering are the reason for the improvement of the tensile strength. Larger pore with irregular shape can cause premature failure for the sintered compacts as it plays a role as a stress concentration for tensile crack initiation. Compare to other compacts, CoCrMo alloy sintered compact at 1350°C-3h exhibited excellent mechanical properties with acceptable hardness and achievable tensile strength.
- vi. However, the elongation values of CoCrMo alloy compact in 1350°C-3h sintered condition have reduced to 12 %. The microstructures from SEM and EDS analysis, have shown that there are carbide precipitates in these compact during this condition which containing materials tend to be brittle. So that, it is reflected that the variance in the strength values of compacts related to the formation of carbide in the microstructure.
- vii. The amount of porosity affected the corrosion behaviour of the sintered compact. The sintered compacts of CoCrMo alloy at 1350°C-3h sintering conditions exhibited better corrosion resistance than others sintering conditions due to a low amount and small size of pores on the sintered compact. But, those sintering conditions are all acceptable for corrosion rate in implant material.

### **5.3 Recommendation**

- i. Thermal debinding and sintering are the most crucial step in the MIM process. Proper compact handling should be made to avoid the compact from damaged. The cleanliness of the tube furnace also should be managed well as it can produce a defect and impurities on the sintered compact

- ii. The optimisation must be made in each MIM process such as injection moulding, solvent debinding, thermal debinding and sintering to identify the optimum parameters for those process. Through optimisation technique such as Response Surface Methodology or Taguchi method, an excellent final compact can be achieved in term of physical, mechanical and chemical properties.
- iii. The promising results in eliminating any grain boundary carbides, CoCrMo alloy compact can be obtained by generally heating the compacts by using nitrogen gas instead of argon gas which can increase the strength of the compacts while maintaining the ductility.
- iv. To achieve higher mechanical properties, the vacuum atmosphere can be utilised as it can reduce the impurities after sintering. Smaller particle size also can be used as finer powder particle can improve the mechanical properties of the sintered compacts.



UMP



## REFERENCES

- Aboulkhair, N. T., Maskery, I., Tuck, C., Ashcroft, I., & Everitt, N. M. (2016). Improving the fatigue behaviour of a selectively laser melted aluminium alloy: Influence of heat treatment and surface quality. *Materials & Design*, *104*, 174-182.
- Ahn, S., Park, S. J., Lee, S., Atre, S. V., & German, R. M. (2009). Effect of powders and binders on material properties and molding parameters in iron and stainless steel powder injection molding process. *Powder Technology*, *193*(2), 162-169.
- Al-Rashidy, Z. M., Farag, M. M., Ghany, N. A. A., Ibrahim, A. M., & Abdel-Fattah, W. I. (2017). Aqueous electrophoretic deposition and corrosion protection of borate glass coatings on 316 L stainless steel for hard tissue fixation. *Surfaces and Interfaces*, *7*, 125-133.
- Aslam, M., Ahmad, F., Yusoff, P. S. M. B. M., Altaf, K., Omar, M. A., & M. German, R. (2016). Powder injection molding of biocompatible stainless steel biodevices. *Powder Technology*, *295*, 84-95.
- Asri, R., Harun, W., Samykano, M., Lah, N., Ghani, S., Tarlochan, F., & Raza, M. (2017). Corrosion and surface modification on biocompatible metals: A review. *Materials Science and Engineering: C*.
- Banerjee, S., & Joens, C. (2012). Debinding and sintering of metal injection molding (MIM) components *Handbook of metal injection molding* (pp. 133-180): Elsevier.
- Baojun, Z., Xuanhui, Q., & Ying, T. (2002). Powder injection molding of WC-8%Co tungsten cemented carbide. *International Journal of Refractory Metals and Hard Materials*, *20*(5-6), 389-394.
- Bartolomeu, F., Sampaio, M., Carvalho, O., Pinto, E., Alves, N., Gomes, J., . . . Miranda, G. (2017). Tribological behavior of Ti6Al4V cellular structures produced by Selective Laser Melting. *Journal of the Mechanical Behavior of Biomedical Materials*.
- BECKER, F. H. (2006). *Debinding processes: Physical and chemical conclusions and their practical realisations*. Paper presented at the CFI. Ceramic forum international.
- Bedolla-Gil, Y., Juarez-Hernandez, A., Perez-Unzueta, A., Garcia-Sanchez, E., Mercado-Solis, R., & Hernandez-Rodriguez, M. (2009). Influence of heat treatments on mechanical properties of a biocompatibility alloy ASTM F75. *Rev. Mex. Fis. S*, *55*(1), 1-5.
- Bellefontaine, G. (2010). *The corrosion of CoCrMo alloys for biomedical applications*. University of Birmingham.

- Bolzoni, L., Herraiz, E., Ruiz-Navas, E. M., & Gordo, E. (2014). Study of the properties of low-cost powder metallurgy titanium alloys by 430 stainless steel addition. *Materials & Design*, *60*, 628-636.
- Bolzoni, L., Ruiz-Navas, E. M., & Gordo, E. (2013). Influence of sintering parameters on the properties of powder metallurgy Ti-3Al-2.5V alloy. *Materials Characterization*, *84*, 48-57.
- Bolzoni, L., Ruiz-Navas, E. M., & Gordo, E. (2015). Feasibility study of the production of biomedical Ti-6Al-4V alloy by powder metallurgy. *Materials Science and Engineering: C*, *49*, 400-407.
- Bolzoni, L., Ruiz-Navas, E. M., & Gordo, E. (2016). Understanding the properties of low-cost iron-containing powder metallurgy titanium alloys. *Materials & Design*, *110*, 317-323.
- Bolzoni, L., Ruiz-Navas, E. M., & Gordo, E. (2017). Quantifying the properties of low-cost powder metallurgy titanium alloys. *Materials Science and Engineering: A*, *687*, 47-53.
- Bullard, M. K., Williams, T., Swift, M., Harken, A. H., & Bir, N. D. (2008). QS227. Pre-Existing Cardiac Dysfunction Limits Recovery of Cardiac Performance After Sepsis. *Journal of Surgical Research*, *144*(2), 357-358.
- Čapek, J., & Vojtěch, D. (2014). Effect of sintering conditions on the microstructural and mechanical characteristics of porous magnesium materials prepared by powder metallurgy. *Materials Science and Engineering: C*, *35*, 21-28.
- Chen, G., Cao, P., Wen, G., & Edmonds, N. (2013). Debinding behaviour of a water soluble PEG/PMMA binder for Ti metal injection moulding. *Materials Chemistry and Physics*, *139*(2-3), 557-565.
- Chen, L.-j., Li, T., Li, Y.-m., He, H., & Hu, Y.-h. (2009). Porous titanium implants fabricated by metal injection molding. *Transactions of Nonferrous Metals Society of China*, *19*(5), 1174-1179.
- Chen, Y., Zhang, J., Dai, N., Qin, P., Attar, H., & Zhang, L.-C. (2017). Corrosion Behaviour of Selective Laser Melted Ti-TiB Biocomposite in Simulated Body Fluid. *Electrochimica Acta*, *232*, 89-97.
- Chikwanda, H., & Machaka, R. (2014). A study of solvent debinding variables on Ti6Al4V green bodies.
- Choi, J.-P., Lee, G.-Y., Song, J.-I., Lee, W.-S., & Lee, J.-S. (2015). Sintering behavior of 316L stainless steel micro-nanopowder compact fabricated by powder injection molding. *Powder Technology*, *279*, 196-202.
- Choi, J.-P., Lyu, H.-G., Lee, W.-S., & Lee, J.-S. (2014a). Densification and microstructural development during sintering of powder injection molded Fe micro-nanopowder. *Powder Technology*, *253*, 596-601.

- Choi, J.-P., Lyu, H.-G., Lee, W.-S., & Lee, J.-S. (2014b). Investigation of the rheological behavior of 316L stainless steel micro-nano powder feedstock for micro powder injection molding. *Powder Technology*, 261, 201-209.
- Cramer, S. D., & Covino, B. S. (2006). *Corrosion: Environments and industries* (Vol. 13): ASM International.
- Darvish, K., Chen, Z. W., & Pasang, T. (2016). Reducing lack of fusion during selective laser melting of CoCrMo alloy: Effect of laser power on geometrical features of tracks. *Materials & Design*, 112, 357-366.
- Dewidar, M. (2012). Influence of processing parameters and sintering atmosphere on the mechanical properties and microstructure of porous 316L stainless steel for possible hard-tissue applications. *Int. J. Mech. Mech. Eng*, 12, 10-24.
- Dewidar, M. M., Yoon, H.-C., & Lim, J. K. (2006). Mechanical properties of metals for biomedical applications using powder metallurgy process: A review. *Metals and Materials International*, 12(3), 193.
- Dobrzański, L. A., Dobrzańska-Danikiewicz, A. D., Ahtelik-Franczak, A., Dobrzański, L. B., Hajduczek, E., & Matula, G. (2017). Fabrication technologies of the sintered materials including materials for medical and dental application *Powder Metallurgy-Fundamentals and Case Studies: InTech*.
- Dourandish, M., Godlinski, D., Simchi, A., & Firouzdor, V. (2008). Sintering of biocompatible P/M Co–Cr–Mo alloy (F-75) for fabrication of porosity-graded composite structures. *Materials Science and Engineering: A*, 472(1–2), 338-346.
- Dufaud, O., Bideau, D., Le Guyadec, F., Corriou, J.-P., Perrin, L., & Caleyron, A. (2014). Self ignition of layers of metal powder mixtures. *Powder Technology*, 254, 160-169.
- Dutta, B., & Froes, F. S. (2017). The additive manufacturing (AM) of titanium alloys. *Metal Powder Report*.
- Ebel, T., Beißig, T., Ebner, S., Luo, X., Nagaram, A. B., & Zhao, D. (2017). Reduction of the embrittlement effect of binder contamination in MIM processing of Ti alloys. *Powder Metallurgy*, 1-10.
- Effects of silver on the microstructure of sintered nickel-copper-zinc ferrites. (1993). *Metal Powder Report*, 48(4), 50.
- Ertugrul, O., Park, H. S., Onel, K., & Willert-Porada, M. (2014). Effect of particle size and heating rate in microwave sintering of 316L stainless steel. *Powder Technology*, 253, 703-709.
- Fayyaz, A., Muhamad, N., & Sulong, A. B. (2018). Microstructure and physical and mechanical properties of micro cemented carbide injection moulded components. *Powder Technology*, 326, 151-158.

- Fox, P., Pogson, S., Sutcliffe, C. J., & Jones, E. (2008). Interface interactions between porous titanium/tantalum coatings, produced by Selective Laser Melting (SLM), on a cobalt–chromium alloy. *Surface and Coatings Technology*, 202(20), 5001-5007.
- Garcia-Cabezon, C., Blanco, Y., Rodriguez-Mendez, M., & Martin-Pedrosa, F. (2017). Characterization of porous nickel-free austenitic stainless steel prepared by mechanical alloying. *Journal of Alloys and Compounds*, 716, 46-55.
- German, R. M. (1990). *Powder injection molding*: Metal Powder Industries Federation Princeton, NJ.
- German, R. M. (1996). Sintering theory and practice. *Solar-Terrestrial Physics (Solnechno-zemnaya fizika)*, 568.
- German, R. M., & Bose, A. (1997). *Injection molding of metals and ceramics*: Metal Powder Industries Federation.
- German, R. M., Bose, A., & Mani, S. S. (1992). Sintering time and atmosphere influences on the microstructure and mechanical properties of tungsten heavy alloys. *Metallurgical Transactions A*, 23(1), 211-219.
- Giacchi, J., Morando, C., Fornaro, O., & Palacio, H. (2011). Microstructural characterization of as-cast biocompatible Co–Cr–Mo alloys. *Materials Characterization*, 62(1), 53-61.
- Girardin, E., Barucca, G., Mengucci, P., Fiori, F., Bassoli, E., Gatto, A., . . . Rutkowski, B. (2016). Biomedical Co-Cr-Mo Components Produced by Direct Metal Laser Sintering1. *Materials Today: Proceedings*, 3(3), 889-897.
- Gorjan, L., Kosmač, T., & Dakskobler, A. (2014). Single-step wick-debinding and sintering for powder injection molding. *Ceramics International*, 40(1), 887-891.
- Grądzka-Dahlke, M., Dąbrowski, J. R., & Dąbrowski, B. (2008). Modification of mechanical properties of sintered implant materials on the base of Co–Cr–Mo alloy. *Journal of Materials Processing Technology*, 204(1–3), 199-205.
- Gulsoy, H. O., Pazarlioglu, S., Gulsoy, N., Gundede, B., & Mutlu, O. (2015). Effect of Zr, Nb and Ti addition on injection molded 316L stainless steel for bio-applications: Mechanical, electrochemical and biocompatibility properties. *Journal of the Mechanical Behavior of Biomedical Materials*, 51, 215-224.
- Guoxin, H., Lixiang, Z., Yunliang, F., & Yanhong, L. (2008). Fabrication of high porous NiTi shape memory alloy by metal injection molding. *Journal of Materials Processing Technology*, 206(1–3), 395-399.
- Gupta, K. (2005). The Co-Cr-Mo (cobalt-chromium-molybdenum) system. *Journal of Phase Equilibria and Diffusion*, 26(1), 87-92.
- Han, C., Li, Y., Wu, X., Ren, S., San, X., & Zhu, X. (2013). Ti/SiO<sub>2</sub> composite fabricated by powder metallurgy for orthopedic implant. *Materials & Design*, 49, 76-80.

- Hayat, M. D., Wen, G., Li, T., & Cao, P. (2015). Compatibility improvement of Ti-MIM feedstock using liquid surfactant. *Journal of Materials Processing Technology*, 224, 33-39.
- Hayat, M. D., Wen, G., Zulkifli, M. F., & Cao, P. (2015). Effect of PEG molecular weight on rheological properties of Ti-MIM feedstocks and water debinding behaviour. *Powder Technology*, 270, Part A, 296-301.
- He, C., Bin, S., Wu, P., Gao, C., Feng, P., Yang, Y., . . . Yang, S. (2017). Microstructure Evolution and Biodegradation Behavior of Laser Rapid Solidified Mg–Al–Zn Alloy. *Metals*, 7(3), 105.
- He, G., Liu, F., Huang, L., Huang, Z., & Jiang, L. (2016). Microstructure evolutions and nucleation mechanisms of dynamic recrystallization of a powder metallurgy Ni-based superalloy during hot compression. *Materials Science and Engineering: A*, 677, 496-504.
- He, J., Shao, Z., Khan, D. F., Yin, H., Elder, S., Zheng, Q., & Qu, X. (2018). Investigation of inhomogeneity in powder injection molding of nano zirconia. *Powder Technology*, 328, 207-214.
- Heaney, D. (2012). Designing for metal injection molding (MIM) *Handbook of metal injection molding* (pp. 29-49): Elsevier.
- Hedberg, Y. S., Qian, B., Shen, Z., Virtanen, S., & Odnevall Wallinder, I. (2014). In vitro biocompatibility of CoCrMo dental alloys fabricated by selective laser melting. *Dental Materials*, 30(5), 525-534.
- Henriques, B., Bagheri, A., Gasik, M., Souza, J. C. M., Carvalho, O., Silva, F. S., & Nascimento, R. M. (2015). Mechanical properties of hot pressed CoCrMo alloy compacts for biomedical applications. *Materials & Design*, 83, 829-834.
- Hoeges, S., Zwiren, A., & Schade, C. (2017). Additive manufacturing using water atomized steel powders. *Metal Powder Report*.
- Hsu, R. W.-W., Yang, C.-C., Huang, C.-A., & Chen, Y.-S. (2005). Electrochemical corrosion studies on Co–Cr–Mo implant alloy in biological solutions. *Materials Chemistry and Physics*, 93(2), 531-538.
- Hwang, K., Lin, H., & Lee, S. (1997). Thermal, solvent, and vacuum debinding mechanisms of PIM compacts. *Material and Manufacturing Process*, 12(4), 593-608.
- Ibrahim, M. H. I., Mohd Amin, A., Asmawi, R., & Mustafa, N. (2016). Influences of Restaurant Waste Fats and Oils (RWFO) from Grease Trap as Binder on Rheological and Solvent Extraction Behavior in SS316L Metal Injection Molding. *Metals*, 6(2), 19.



- Ibrahim, M. Z., Sarhan, A. A. D., Yusuf, F., & Hamdi, M. (2017). Biomedical materials and techniques to improve the tribological, mechanical and biomedical properties of orthopedic implants – A review article. *Journal of Alloys and Compounds*, 714, 636-667.
- Imai, H., Tanaka, Y., Nomura, N., Doi, H., Tsutsumi, Y., Ono, T., & Hanawa, T. (2017). Magnetic susceptibility, artifact volume in MRI, and tensile properties of swaged Zr–Ag composites for biomedical applications. *Journal of the Mechanical Behavior of Biomedical Materials*, 66, 152-158.
- Imgrund, P., Hein, S., Reindl, A., Grunwald, I., & Goncalves, P. Biocompatibility, mechanical properties and degradation of Fe based alloys and composites processed by Powder Injection Molding.
- Imran, M., Raza, M., Khan, M. S., & Hayat, Y. (2017). EFFECT OF COBALT-CHROMIUM ALLOY RE-USE IN DENISTRY ON ITS CASTABILITY VALUE. *Journal of Ayub Medical College Abbottabad*, 29(2), 270-274.
- Ismail, M. H., Goodall, R., Davies, H. A., & Todd, I. (2012). Porous NiTi alloy by metal injection moulding/sintering of elemental powders: Effect of sintering temperature. *Materials Letters*, 70, 142-145.
- Ji, C. H., Loh, N. H., Khor, K. A., & Tor, S. B. (2001). Sintering study of 316L stainless steel metal injection molding parts using Taguchi method: final density. *Materials Science and Engineering: A*, 311(1–2), 74-82.
- Jinlong, L., Meng, Y., Miura, H., & Tongxiang, L. (2017). The effect of surface enriched chromium and grain refinement by ball milling on corrosion resistance of 316L stainless steel. *Materials Research Bulletin*, 91, 91-97.
- Johari, N., Sauti, R., Abdullah, N., Mohd Zainon, N., Meh, B., Abd Jalil, M. N., . . . Omar, M. A. (2016). *Physical and mechanical properties of injection molded Co-Cr-Mo alloy powder for orthopedic applications*. Paper presented at the Advanced Materials Research.
- Johnson, J. L., & Heaney, D. F. (2005). Metal injection molding of Co-28Cr-6Mo.
- Kan, Y., Zhang, S.-h., Zhang, L.-w., Cheng, M., Song, H.-w., & Lu, H.-w. (2014). Healing Behavior of Micropores in Powder Metallurgy 316L Stainless Steel during Hot Forging and Heat Treatment. *Journal of Iron and Steel Research, International*, 21(9), 862-868.
- Kayhan, S. M., Tahmasebifar, A., Koç, M., Usta, Y., Tezcaner, A., & Evis, Z. (2016). Experimental and numerical investigations for mechanical and microstructural characterization of micro-manufactured AZ91D magnesium alloy disks for biomedical applications. *Materials & Design*, 93, 397-408.
- Kaysser, W. A., & Weise, W. (1993). Powder metallurgy and sintered materials. *Ullmann's Encyclopedia of Industrial Chemistry*.



- Khanlari, K., Ramezani, M., Hayat, M., Piaras, K., Cao, P., & Neitzert, T. (2017). *Microstructural and Mechanical Properties of Porous 60NiTi Prepared by Conventional Press-and-sinter Method*. Paper presented at the MATEC Web of Conferences.
- Kikuchi, S., Hayami, Y., Ishiguri, T., Guennec, B., Ueno, A., Ota, M., & Ameyama, K. (2017). Effect of bimodal grain size distribution on fatigue properties of Ti-6Al-4V alloy with harmonic structure under four-point bending. *Materials Science and Engineering: A*, 687, 269-275.
- Klarstrom, D., & Wu, J. (2004). *Metallography and microstructures of cobalt and cobalt alloys*. *Materials Park, OH: ASM International, 2004.*, 762-774.
- Koike, M., Martinez, K., Guo, L., Chahine, G., Kovacevic, R., & Okabe, T. (2011). Evaluation of titanium alloy fabricated using electron beam melting system for dental applications. *Journal of Materials Processing Technology*, 211(8), 1400-1408.
- Koseski, R. P., Suri, P., Earhardt, N. B., German, R. M., & Kwon, Y.-S. (2005). Microstructural evolution of injection molded gas- and water-atomized 316L stainless steel powder during sintering. *Materials Science and Engineering: A*, 390(1-2), 171-177.
- Kurgan, N. (2014). Effect of porosity and density on the mechanical and microstructural properties of sintered 316L stainless steel implant materials. *Materials & Design*, 55(Supplement C), 235-241.
- Lang, D., Pöhl, C., Holec, D., Schatte, J., Povoden-Karadeniz, E., Knabl, W., . . . Primig, S. (2016). On the chemistry of the carbides in a molybdenum base Mo-Hf-C alloy produced by powder metallurgy. *Journal of Alloys and Compounds*, 654, 445-454.
- Lee, S.-H., Takahashi, E., Nomura, N., & Chiba, A. (2005). Effect of heat treatment on microstructure and mechanical properties of Ni-and C-free Co-Cr-Mo alloys for medical applications. *Materials transactions*, 46(8), 1790-1793.
- Lee, S. H., Messing, G. L., & Awano, M. (2008). Sintering Arches for Cosintering Camber-Free SOFC Multilayers. *Journal of the American Ceramic Society*, 91(2), 421-427.
- Levine, D. J. (1987). Metallurgical relationships of porous-coated ASTM F75 alloys *Quantitative Characterization and Performance of Porous Implants for Hard Tissue Applications*: ASTM International.
- Li, B. Q., Wang, C. Y., & Lu, X. (2013). Effect of pore structure on the compressive property of porous Ti produced by powder metallurgy technique. *Materials & Design*, 50, 613-619.
- Li, D., Hou, H., Tan, Z., & Lee, K. (2009). Metal injection molding of pure molybdenum. *Advanced Powder Technology*, 20(5), 480-487.

- Li, J., Chen, C., Liao, J., Liu, L., Ye, X., Lin, S., & Ye, J. Bond strengths of porcelain to cobalt-chromium alloys made by casting, milling, and selective laser melting. *The Journal of Prosthetic Dentistry*.
- Li, W., Li, S., Liu, J., Zhang, A., Zhou, Y., Wei, Q., . . . Shi, Y. (2016). Effect of heat treatment on AlSi10Mg alloy fabricated by selective laser melting: Microstructure evolution, mechanical properties and fracture mechanism. *Materials Science and Engineering: A*, 663, 116-125.
- Limberg, W., Ebel, T., Pyczak, F., Oehring, M., & Schimansky, F. P. (2012). Influence of the sintering atmosphere on the tensile properties of MIM-processed Ti 45Al 5Nb 0.2B 0.2C. *Materials Science and Engineering: A*, 552, 323-329.
- Limmahakhun, S., Oloyede, A., Sitthiseripratip, K., Xiao, Y., & Yan, C. (2017). Stiffness and strength tailoring of cobalt chromium graded cellular structures for stress-shielding reduction. *Materials & Design*, 114, 633-641.
- Lin, D., Sanetnik, D., Cho, H., Chung, S. T., Kwon, Y. S., Kate, K. H., . . . Park, S. J. (2017). Rheological and thermal debinding properties of blended elemental Ti-6Al-4V powder injection molding feedstock. *Powder Technology*, 311, 357-363.
- Liu, J., Chang, L., Liu, H., Li, Y., Yang, H., & Ruan, J. Microstructure, mechanical behavior and biocompatibility of powder metallurgy Nb-Ti-Ta alloys as biomedical material. *Materials Science and Engineering: C*.
- Liverani, E., Fortunato, A., Leardini, A., Belvedere, C., Siegler, S., Ceschini, L., & Ascari, A. (2016). Fabrication of Co-Cr-Mo endoprosthetic ankle devices by means of Selective Laser Melting (SLM). *Materials & Design*, 106, 60-68.
- Liverani, E., Toschi, S., Ceschini, L., & Fortunato, A. (2017). Effect of Selective Laser Melting (SLM) process parameters on microstructure and mechanical properties of 316L austenitic stainless steel. *Journal of Materials Processing Technology*.
- Loh, L.-E., Chua, C.-K., Yeong, W.-Y., Song, J., Mapar, M., Sing, S.-L., . . . Zhang, D.-Q. (2015). Numerical investigation and an effective modelling on the Selective Laser Melting (SLM) process with aluminium alloy 6061. *International Journal of Heat and Mass Transfer*, 80, 288-300.
- Lu, L., Sevonkaev, I., Kumar, A., & Goia, D. V. (2014). Strategies for tailoring the properties of chemically precipitated metal powders. *Powder Technology*, 261, 87-97.
- Lu, Y., Gan, Y., Lin, J., Guo, S., Wu, S., & Lin, J. (2017). Effect of laser speeds on the mechanical property and corrosion resistance of CoCrW alloy fabricated by SLM. *Rapid Prototyping Journal*, 23(1).
- Lu, Y., Wu, S., Gan, Y., Huang, T., Yang, C., Junjie, L., & Lin, J. (2015). Study on the microstructure, mechanical property and residual stress of SLM Inconel-718 alloy

manufactured by differing island scanning strategy. *Optics & Laser Technology*, 75, 197-206.

- Madeira, S., Pinto, A., Rodrigues, L., Carvalho, O., Miranda, G., Reis, R., . . . Silva, F. (2017). Effect of sintering pressure on microstructure and mechanical properties of hot-pressed Ti6Al4V-ZrO<sub>2</sub> materials. *Materials & Design*, 120, 394-403.
- Madhukar, S., Sai, P. V., Kumar, S., & Prakash, D. J. (2017). Experimental Investigation on Effect of Heat Treatment on Mechanical Properties of Titanium Alloy (Ti-6Al-4V). *International Journal of Current Engineering and Technology*, 7(1).
- Málek, J., Hnilica, F., Veselý, J., & Smola, B. (2013). Heat treatment and mechanical properties of powder metallurgy processed Ti-35.5Nb-5.7Ta beta-titanium alloy. *Materials Characterization*, 84, 225-231.
- Manonukul, A., Muenya, N., Léaux, F., & Amaranan, S. (2010). Effects of replacing metal powder with powder space holder on metal foam produced by metal injection moulding. *Journal of Materials Processing Technology*, 210(3), 529-535.
- Marek, I., Novák, P., MLYNÁR, A., VOJTĚCHA, D., Kubatík, T., & Málek, J. (2015). Powder Metallurgy Preparation of Co-Based Alloys for Biomedical Applications. *Acta Physica Polonica, A*, 128(4).
- Mariot, P., Leeflang, M. A., Schaeffer, L., & Zhou, J. (2016). An investigation on the properties of injection-molded pure iron potentially for biodegradable stent application. *Powder Technology*, 294, 226-235.
- Md Ani, S., Muchtar, A., Muhamad, N., & Ghani, J. A. (2014). Binder removal via a two-stage debinding process for ceramic injection molding parts. *Ceramics International*, 40(2), 2819-2824.
- Mengucci, P., Gatto, A., Bassoli, E., Denti, L., Fiori, F., Girardin, E., . . . Barucca, G. (2017). Effects of build orientation and element partitioning on microstructure and mechanical properties of biomedical Ti-6Al-4V alloy produced by laser sintering. *Journal of the Mechanical Behavior of Biomedical Materials*, 71, 1-9.
- Mirzaei, M., & Paydar, M. H. (2017). A novel process for manufacturing porous 316 L stainless steel with uniform pore distribution. *Materials & Design*, 121, 442-449.
- Mohd Afian, O., Baharin, S., Nurazilah, M. Z., Norazlan, R., Mohd Nizam, A. J., Mohd Bakri, M. H., . . . Noorsyakirah, A. (2014). Innovative Metal injection molding (MIM) method for producing CoCrMo alloy metallic prosthesis for orthopedic applications.
- Montani, M., Demir, A. G., Mostaed, E., Vedani, M., & Previtali, B. (2017). Processability of pure Zn and pure Fe by SLM for biodegradable metallic implant manufacturing. *Rapid Prototyping Journal*, 23(3).

- Montero-Ocampo, C., & Salinas Rodriguez, A. (1995). Effect of carbon content on the resistance to localized corrosion of as-cast cobalt-based alloys in an aqueous chloride solution. *Journal of Biomedical Materials Research Part A*, 29(4), 441-453.
- Murakami, M., Nomura, N., Doi, H., Tsutsumi, Y., Nakamura, H., Chiba, A., & Hanawa, T. (2010). Microstructures of Zr-Added Co-Cr-Mo Alloy Compacts Fabricated with a Metal Injection Molding Process and Their Metal Release in 1 mass% Lactic Acid. *Materials transactions*, 51(7), 1281-1287.
- Muterlle, P. V., Perina, M., Mantovani, M., & Molinari, A. (2009). Dissolution the 'the key' to make carbide more friendly. *Metal Powder Report*, 64(2), 30-33.
- Muterlle, P. V., Zendron, M., Perina, M., Bardini, R., & Molinari, A. (2009). Microstructure and tensile properties of metal injection molding Co-29Cr-6Mo-0.23C alloy. *Journal of Materials Science*, 45(4), 1091-1099.
- Mutlu, I. (2016). Synthesis and characterization of Ti-Co alloy foam for biomedical applications. *Transactions of Nonferrous Metals Society of China*, 26(1), 126-137.
- Narushima, T., Mineta, S., Kurihara, Y., & Ueda, K. (2013). Precipitates in biomedical Co-Cr alloys. *Jom*, 65(4), 489-504.
- Ng, C. C., Savalani, M. M., Lau, M. L., & Man, H. C. (2011). Microstructure and mechanical properties of selective laser melted magnesium. *Applied Surface Science*, 257(17), 7447-7454.
- Nouri, A., Hodgson, P. D., & Wen, C. E. (2010). Effect of process control agent on the porous structure and mechanical properties of a biomedical Ti-Sn-Nb alloy produced by powder metallurgy. *Acta Biomaterialia*, 6(4), 1630-1639.
- Nyberg, E., Miller, M., Simmons, K., & Weil, K. S. (2005). Microstructure and mechanical properties of titanium components fabricated by a new powder injection molding technique. *Materials Science and Engineering: C*, 25(3), 336-342.
- Obadele, B. A., Ige, O. O., & Olubambi, P. A. (2017). Fabrication and characterization of titanium-nickel-zirconia matrix composites prepared by spark plasma sintering. *Journal of Alloys and Compounds*, 710, 825-830.
- Obasi, G. C., Ferri, O. M., Ebel, T., & Bormann, R. (2010). Influence of processing parameters on mechanical properties of Ti-6Al-4V alloy fabricated by MIM. *Materials Science and Engineering: A*, 527(16-17), 3929-3935.
- Okulov, I., Volegov, A., Attar, H., Bönisch, M., Ehtemam-Haghighi, S., Calin, M., & Eckert, J. (2017). Composition optimization of low modulus and high-strength TiNb-based alloys for biomedical applications. *Journal of the Mechanical Behavior of Biomedical Materials*, 65, 866-871.

- Omar, M., Ibrahim, R., Sidik, M., Mustapha, M., & Mohamad, M. (2003). Rapid debinding of 316L stainless steel injection moulded component. *Journal of Materials Processing Technology*, 140(1), 397-400.
- OMAR, M., SAUTI, R., & ABDULLAH, N. DEBINDING AND SINTERING CHARACTERISTIC OF INJECTION MOULDING CoCrMo ALLOY POWDER FOR BIOMEDICAL APPLICATIONS.
- Omar, M. A., & Subuki, I. (2012). *Sintering Characteristics of Injection Moulded 316L Component Using Palm-Based Biopolymer Binder*: INTECH Open Access Publisher.
- Onbattuvelli, V. P., Chinn, R., Enneti, R. K., Park, S.-J., & Atre, S. V. (2014). The effects of nanoparticle addition on binder removal from injection molded silicon carbide. *Ceramics International*, 40(9, Part A), 13861-13868.
- Özbilen, S., Liebert, D., Beck, T., & Bram, M. (2016). Fatigue behavior of highly porous titanium produced by powder metallurgy with temporary space holders. *Materials Science and Engineering: C*, 60, 446-457.
- Páez-Pavón, A., Jiménez-Morales, A., Santos, T. G., Quintino, L., & Torralba, J. M. (2016). Influence of thermal debinding on the final properties of Fe–Si soft magnetic alloys for metal injection molding (MIM). *Journal of Magnetism and Magnetic Materials*, 416, 342-347.
- Palermo, T. (2014). Carbon potential control in MIM sintering furnace atmospheres. *Metal Powder Report*, 69(3), 16-21.
- Quinard, C., Song, J., Barriere, T., & Gelin, J. C. (2011). Elaboration of PIM feedstocks with 316L fine stainless steel powders for the processing of micro-components. *Powder Technology*, 208(2), 383-389.
- Raghavendra, G. M., Varaprasad, K., & Jayaramudu, T. (2015). Chapter 2 - Biomaterials: Design, Development and Biomedical Applications A2 - Thomas, Sabu. In Y. Grohens & N. Ninan (Eds.), *Nanotechnology Applications for Tissue Engineering* (pp. 21-44). Oxford: William Andrew Publishing.
- Ratner, B. D., Hoffman, A. S., Schoen, F. J., & Lemons, J. E. (2004). *Biomaterials science: an introduction to materials in medicine*: Academic press.
- Raza, M. R., Ahmad, F., Muhamad, N., Sulong, A. B., Omar, M. A., Akhtar, M. N., & Aslam, M. (2016). Effects of solid loading and cooling rate on the mechanical properties and corrosion behavior of powder injection molded 316 L stainless steel. *Powder Technology*, 289, 135-142.
- Raza, M. R., Ahmad, F., Omar, M., German, R., & Muhsan, A. S. (2012). *Defect analysis of 316LSS during the powder injection moulding process*. Paper presented at the Defect and Diffusion Forum.
- Raza, M. R., Ahmad, F., Omar, M. A., & German, R. M. (2012). Effects of cooling rate on mechanical properties and corrosion resistance of vacuum sintered powder



- injection molded 316L stainless steel. *Journal of Materials Processing Technology*, 212(1), 164-170.
- Raza, M. R., Sulong, A. B., Muhamad, N., Akhtar, M. N., & Rajabi, J. (2015). Effects of binder system and processing parameters on formability of porous Ti/HA composite through powder injection molding. *Materials & Design*, 87, 386-392.
- Robison, N. E., Tantbirojn, D., Versluis, A., & Cagna, D. R. (2016). Failure strengths of denture teeth fabricated on injection molded or compression molded denture base resins. *The Journal of Prosthetic Dentistry*, 116(2), 292-299.
- Rodrigues, W. C., Broilo, L. R., Schaeffer, L., Knörnschild, G., & Espinoza, F. R. M. (2011a). Powder metallurgical processing of Co-28% Cr-6% Mo for dental implants: Physical, mechanical and electrochemical properties. *Powder Technology*, 206(3), 233-238.
- Rodrigues, W. C., Broilo, L. R., Schaeffer, L., Knörnschild, G., & Espinoza, F. R. M. (2011b). Powder metallurgical processing of Co-28%Cr-6%Mo for dental implants: Physical, mechanical and electrochemical properties. *Powder Technology*, 206(3), 233-238.
- Ryan, G., Pandit, A., & Apatsidis, D. P. (2006). Fabrication methods of porous metals for use in orthopaedic applications. *Biomaterials*, 27(13), 2651-2670.
- Saedi, S. (2017). Shape Memory Behavior of Dense and Porous NiTi Alloys Fabricated by Selective Laser Melting.
- Saedi, S., Turabi, A. S., Andani, M. T., Moghaddam, N. S., Elahinia, M., & Karaca, H. (2017). Texture, aging, and superelasticity of selective laser melting fabricated Ni-rich NiTi alloys. *Materials Science and Engineering: A*.
- Salahinejad, E., Amini, R., & Hadianfard, M. (2010). Contribution of nitrogen concentration to compressive elastic modulus of 18Cr-12Mn-xN austenitic stainless steels developed by powder metallurgy. *Materials & Design*, 31(4), 2241-2244.
- Salleh, F. M., Sulong, A. B., Muhamad, N., Mohamed, I. F., Mas'ood, N. N., & Ukwueze, B. E. (2017). Co-Powder Injection Moulding (Co-PIM) Processing of Titanium Alloy (Ti-6Al-4V) and Hydroxyapatite (HA). *Procedia Engineering*, 184, 334-343.
- Scott Weil, K., Nyberg, E., & Simmons, K. (2006). A new binder for powder injection molding titanium and other reactive metals. *Journal of Materials Processing Technology*, 176(1-3), 205-209.
- Seyed Farid Seyed, S., Samira, G., Mehdi, M., Hooman, Y., Hendrik Simon Cornelis, M., Nahrizul Adib, K., & Noor Azuan Abu, O. (2015). A review on powder-based additive manufacturing for tissue engineering: selective laser sintering and inkjet 3D printing. *Science and Technology of Advanced Materials*, 16(3), 033502.



- Shang, Y., Yuan, Y., Li, D., Li, Y., & Chen, J. (2017). Effects of scanning speed on in vitro biocompatibility of 316L stainless steel parts elaborated by selective laser melting. *The International Journal of Advanced Manufacturing Technology*, 1-7.
- Shu, G. J., Hwang, K. S., & Pan, Y. T. (2006). Improvements in sintered density and dimensional stability of powder injection-molded 316L compacts by adjusting the alloying compositions. *Acta Materialia*, 54(5), 1335-1342.
- Sidambe, A. T., Figueroa, I. A., Hamilton, H. G. C., & Todd, I. (2012). Metal injection moulding of CP-Ti components for biomedical applications. *Journal of Materials Processing Technology*, 212(7), 1591-1597.
- Simoneau, C., Terriault, P., Jetté, B., Dumas, M., & Brailovski, V. (2017). Development of a porous metallic femoral stem: Design, manufacturing, simulation and mechanical testing. *Materials & Design*, 114, 546-556.
- Song, B., Dong, S., Zhang, B., Liao, H., & Coddet, C. (2012). Effects of processing parameters on microstructure and mechanical property of selective laser melted Ti6Al4V. *Materials & Design*, 35, 120-125.
- Sotomayor, M. E., Várez, A., & Levenfeld, B. (2010a). Influence of powder particle size distribution on rheological properties of 316 L powder injection moulding feedstocks. *Powder Technology*, 200(1-2), 30-36.
- Sotomayor, M. E., Várez, A., & Levenfeld, B. (2010b). Influence of powder particle size distribution on rheological properties of 316L powder injection moulding feedstocks. *Powder Technology*, 200(1), 30-36.
- Srivastava, Y., & Srivastava, S. (2017). Preparation and properties of Cobalt-based soft magnetic material prepared by novel powder metallurgy. *Journal of Magnetism and Magnetic Materials*, 423, 267-274.
- Sun, H., Li, X., Zhang, P., & Fang, W. (2014). The microstructure and tensile properties of the Ti<sub>2</sub>AlC reinforced TiAl composites fabricated by powder metallurgy. *Materials Science and Engineering: A*, 611, 257-262.
- Sun, Z., Tan, X., Tor, S. B., & Yeong, W. Y. (2016). Selective laser melting of stainless steel 316L with low porosity and high build rates. *Materials & Design*, 104, 197-204.
- Tahmasebifar, A., Kayhan, S. M., Evis, Z., Tezcaner, A., Çinici, H., & Koç, M. (2016). Mechanical, electrochemical and biocompatibility evaluation of AZ91D magnesium alloy as a biomaterial. *Journal of Alloys and Compounds*, 687, 906-919.
- Takaichi, A., Suyalatu, Nakamoto, T., Joko, N., Nomura, N., Tsutsumi, Y., . . . Hanawa, T. (2013). Microstructures and mechanical properties of Co-29Cr-6Mo alloy fabricated by selective laser melting process for dental applications. *Journal of the Mechanical Behavior of Biomedical Materials*, 21, 67-76.

- Tandon, R., Disegi, J., Kennedy, R., & Pilliar, R. (1999). *Cobalt Base Alloys for Biomedical Applications ASTM STP 1365*.
- Thavanayagam, G., Pickering, K. L., Swan, J. E., & Cao, P. (2015). Analysis of rheological behaviour of titanium feedstocks formulated with a water-soluble binder system for powder injection moulding. *Powder Technology*, 269, 227-232.
- Thomas-Vielma, P., Cervera, A., Levenfeld, B., & Várez, A. (2008). Production of alumina parts by powder injection molding with a binder system based on high density polyethylene. *Journal of the European Ceramic Society*, 28(4), 763-771.
- Torres, Y., Lascano, S., Bris, J., Pavón, J., & Rodríguez, J. A. (2014). Development of porous titanium for biomedical applications: A comparison between loose sintering and space-holder techniques. *Materials Science and Engineering: C*, 37, 148-155.
- Trimble, D., Shipley, H., Lea, L., Jardine, A., & O'Donnell, G. (2017). Constitutive analysis of biomedical grade Co-27Cr-5Mo alloy at high strain rates. *Materials Science and Engineering: A*, 682, 466-474.
- Vervoort, P., Vetter, R., & Duszczuk, J. (1996). Overview of powder injection molding. *Advanced Performance Materials*, 3(2), 121-151.
- Vidal, C. V., & Muñoz, A. I. (2009). Effect of thermal treatment and applied potential on the electrochemical behaviour of CoCrMo biomedical alloy. *Electrochimica Acta*, 54(6), 1798-1809.
- Vieira Muterlle, P. (2010). *Microstructural and mechanical properties of Co and Ti alloys for biomedical applications produced by metal injection molding (MIM)*. University of Trento.
- Wahi, A., Muhamad, N., Sulong, A. B., & Ahmad, R. N. (2016). Effect of Sintering Temperature on Density, Hardness and Strength of MIM Co<sub>30</sub>Cr<sub>6</sub>Mo Biomedical Alloy. *Journal of the Japan Society of Powder and Powder Metallurgy*, 63(7), 434-437.
- Wang, C., Lu, Z., & Zhang, K. (2012). Microstructure, mechanical properties and sintering model of B<sub>4</sub>C nozzle with micro holes by powder injection molding. *Powder Technology*, 228, 334-338.
- Wang, D., Yang, Y., Liu, R., Xiao, D., & Sun, J. (2013). Study on the designing rules and processability of porous structure based on selective laser melting (SLM). *Journal of Materials Processing Technology*, 213(10), 1734-1742.
- Wang, H.-S., Chen, H.-G., Gu, J.-W., Hsu, C.-E., & Wu, C.-Y. (2014). Effects of heat treatment processes on the microstructures and properties of powder metallurgy produced Cu–Ni–Si–Cr alloy. *Materials Science and Engineering: A*, 619, 221-227.
- Wang, J.-L., Liu, R., Majumdar, T., Mantri, S., Ravi, V., Banerjee, R., & Birbilis, N. (2017). A closer look at the in vitro electrochemical characterisation of titanium

- alloys for biomedical applications using in-situ methods. *Acta Biomaterialia*, *54*, 469-478.
- Wang, M., Chen, B., Huang, S., Wang, X., Liu, B., Ge, Q., & Xie, S. (2017). A novel technology for vanadium and chromium recovery from V-Cr-bearing reducing slag. *Hydrometallurgy*, *171*, 116-122.
- Wang, X., Chen, Y., Xu, L., Liu, Z., & Woo, K.-D. (2013). Effects of Sn content on the microstructure, mechanical properties and biocompatibility of Ti-Nb-Sn/hydroxyapatite biocomposites synthesized by powder metallurgy. *Materials & Design*, *49*, 511-519.
- Wen, M., Wen, C., Hodgson, P., & Li, Y. (2014). Fabrication of Ti-Nb-Ag alloy via powder metallurgy for biomedical applications. *Materials & Design*, *56*, 629-634.
- West, E. G. (1982). *Copper and its Alloys*: Ellis Horwood.
- Williams, D. F., Cahn, R. W., & Bever, M. B. (1990). *Concise encyclopedia of medical & dental materials*: Pergamon Press. Distributed in North and South America by MIT Press.
- Xiao, M., Chen, Y., Biao, M., Zhang, X., & Yang, B. (2017). Bio-functionalization of biomedical metals. *Materials Science and Engineering: C*, *70*, 1057-1070.
- Xin, X. Z., Chen, J., Xiang, N., Gong, Y., & Wei, B. (2014). Surface characteristics and corrosion properties of selective laser melted Co-Cr dental alloy after porcelain firing. *Dental Materials*, *30*(3), 263-270.
- Xu, D., & Xu, Y. (2017). A versatile approach to vacuum injection casting for materials research and development. *Review of Scientific Instruments*, *88*(3), 033902.
- Yablokova, G., Speirs, M., Van Humbeeck, J., Kruth, J. P., Schrooten, J., Cloots, R., . . . Luyten, J. (2015). Rheological behavior of  $\beta$ -Ti and NiTi powders produced by atomization for SLM production of open porous orthopedic implants. *Powder Technology*, *283*, 199-209.
- Yadroitsev, I., Krakhmalev, P., & Yadroitsava, I. (2014). Selective laser melting of Ti6Al4V alloy for biomedical applications: Temperature monitoring and microstructural evolution. *Journal of Alloys and Compounds*, *583*, 404-409.
- Yadroitsev, I., & Smurov, I. (2011). Surface Morphology in Selective Laser Melting of Metal Powders. *Physics Procedia*, *12*, 264-270.
- Yan, C., Hao, L., Hussein, A., & Young, P. (2015). Ti-6Al-4V triply periodic minimal surface structures for bone implants fabricated via selective laser melting. *Journal of the Mechanical Behavior of Biomedical Materials*, *51*, 61-73.
- Yazdimamaghani, M., Razavi, M., Vashae, D., Moharamzadeh, K., Boccaccini, A. R., & Tayebi, L. (2017). Porous magnesium-based scaffolds for tissue engineering. *Materials Science and Engineering: C*, *71*, 1253-1266.

- Yoon, S., Kang, S., Choi, Y., Choi, H., & Lee, S.-J. (2016). Effect of relative density on microstructure and mechanical properties of Fe-12Mn-0.2C alloy fabricated by powder metallurgy. *Powder Technology*, 298, 106-111.
- Youhua, H., Yimin, L., Hao, H., Jia, L., & Xiao, T. (2010). Preparation and Mechanical Properties of Inconel718 Alloy by Metal Injection Molding. *Rare Metal Materials and Engineering*, 39(5), 775-780.
- Zaky, M. (2004). Effect of solvent debinding variables on the shape maintenance of green molded bodies. *Journal of Materials Science*, 39(10), 3397-3402.
- Zhang, L. C., Klemm, D., Eckert, J., Hao, Y. L., & Sercombe, T. B. (2011). Manufacture by selective laser melting and mechanical behavior of a biomedical Ti-24Nb-4Zr-8Sn alloy. *Scripta Materialia*, 65(1), 21-24.
- Zhang, Y., Liu, F., Chen, J., & Yuan, Y. (2017). Effects of surface quality on corrosion resistance of 316L stainless steel parts manufactured via SLM. *Journal of Laser Applications*, 29(2), 022306.
- Zhao, D., Chang, K., Ebel, T., Nie, H., Willumeit, R., & Pyczak, F. (2015). Sintering behavior and mechanical properties of a metal injection molded Ti-Nb binary alloy as biomaterial. *Journal of Alloys and Compounds*, 640, 393-400.
- Zhou, J., Zhu, D., Tang, L., Jiang, X., Chen, S., Peng, X., & Hu, C. (2016). Microstructure and properties of powder metallurgy Cu-1%Cr-0.65%Zr alloy prepared by hot pressing. *Vacuum*, 131, 156-163.

The logo for UMP (Universitas Muhammadiyah Purwokerto) is a large, stylized shield shape. It is divided into four quadrants by a white cross. The top-left quadrant is light blue, the top-right is light green, the bottom-left is light purple, and the bottom-right is light teal. The letters 'UMMP' are written in a bold, white, sans-serif font across the center of the shield.

UMMP

**APPENDIX A**

**PUBLICATIONS**

<b>No.</b>	<b>Paper title</b>	<b>Journal</b>	<b>Type</b>	<b>Impact factor</b>	<b>Status</b>	<b>Citation</b>
1	<b>Paraffin wax removal from metal injection moulded CoCrMo Alloy Compact by Solvent Debinding Process</b>	ICMER : Material Science and Engineering	Scopus index	-	Published	N.A.N. Dandang., et al., Paraffin Wax Removal from Metal injection Moulded CoCrMo Alloy Compact by Solvent Debinding Process . Journal of Materials and Science Engineering, 2017(257)
2	<b>Physical properties and microstructure study of 316L SS fabricated by metal injection moulding process</b>	AMC: Journal of Physics	Scopus index	-	Published	N.A.N. Dandang, et al., Physical Properties and Microstructure Study of 316L SS Fabricated by Metal Injection Moulding Process. Journals Of Physics 2017(1901)
3	<b>Effect of sintering temperature on physical properties &amp; hardness of CoCrMo alloys fabricated by metal injection moulding process</b>	ICMER : Material Science and Engineering	Scopus index	-	Published	N.A.N. Dandang., et al., Effect of sintering temperature on physical properties & hardness of CoCrMo alloys fabricated by metal injection moulding process. Journal of Materials and Science Engineering, 2017(257):